

MIRT

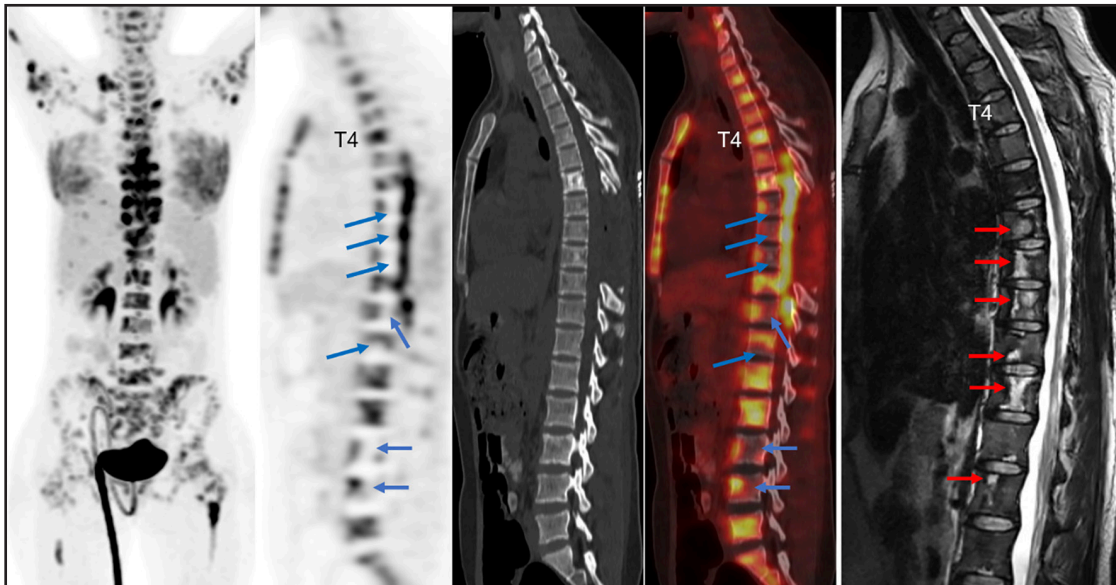
Molecular Imaging and Radionuclide Therapy

October 2024

Volume 33

Issue 3

www.tsnm.org



"Official Journal of the Turkish Society of Nuclear Medicine"

Scientific Advisory Board

Ayşegül Akgün

Ege University, Medical School, Department of Nuclear Medicine, İzmir, Türkiye

Esma Akın

The George Washington University, Medical School, Department of Diagnostic Radiology, Washington DC, USA

Akram Al-Ibraheem

King Hussein Cancer Center (KHCC), Department of Nuclear Medicine, Amman, Jordan

Claudine Als

Hopitaux Robert Schuman Zitha Klinik, Médecine Nucléaire, Luxembourg

Corinna Altini

Nuclear Medicine Unit, AOU Policlinic of Bari – University of Bari “Aldo Moro”, Bari, Italy

Vera Artiko

Clinical Center of Serbia, Center for Nuclear Medicine, Belgrade, Serbia

Nuri Arslan

University of Health Sciences Türkiye, Gülhane Medical School, Gülhane Training and Research Hospital, Clinic of Nuclear Medicine, Ankara, Türkiye

Lütfiye Özlem Atay

Gazi University Faculty of Medicine, Department of Nuclear Medicine, Ankara, Türkiye

Marika Bajc

Lund University Hospital, Clinic of Clinical Physiology, Lund, Sweden

Lorenzo Biassoni

Great Ormond Street Hospital for Children NHS Foundation Trust, Department of Radiology, London, United Kingdom

Hans Jürgen Biersack

University of Bonn, Department of Nuclear Medicine, Clinic of Radiology, Bonn, Germany

M. Donald Blafox

Albert Einstein College of Medicine, Department of Radiology, Division of Nuclear Medicine, New York, USA.

Patrick Bourguet

Centre Eugène Marquis Department of Nuclear Medicine, Clinic of Radiology, Rennes, France

Murat Fani Bozkurt

FEBNM Hacettepe University, Medical School, Department of Nuclear Medicine, Ankara, Türkiye

A. Cahid Civelek

NIH Clinical Center, Division of Nuclear Medicine, Bethesda, USA

Arturo Chiti

Humanitas University, Department of Biomedical Sciences; Humanitas Clinical and Research Center, Clinic of Nuclear Medicine, Milan, Italy

Josep Martin Comin

Hospital Universitari de Bellvitge, Department of Nuclear Medicine, Barcelona, Spain

Alberto Cuocolo

University of Naples Federico II, Department of Advanced Biomedical Sciences, Napoli, Italy

Tevfik Fikret Çermik

University of Health Sciences Türkiye, İstanbul Training and Research Hospital, Clinic of Nuclear Medicine, İstanbul, Türkiye

Angelika Bischof Delaloye

University Hospital of Lausanne, Department of Radiology, Lausanne, Switzerland

Mustafa Demir

İstanbul University, Cerrahpaşa Medical School, Department of Nuclear Medicine, İstanbul, Türkiye

Hakan Demir

Kocaeli University Medical School, Department of Nuclear Medicine, Kocaeli, Türkiye

Peter Josef Ell

University College Hospital, Institute of Nuclear Medicine, London, United Kingdom

Tanju Yusuf Erdil

Marmara University, Pendik Training and Research Hospital, Clinic of Nuclear Medicine, İstanbul, Türkiye

Türkan Ertay

Dokuz Eylül University, Medical School, Department of Nuclear Medicine, İzmir, Türkiye

Jure Fettich

University Medical Centre Ljubljana, Department for Nuclear Medicine, Ljubljana, Slovenia

Christiane Franzius

Klinikum Bremen Mitte Center, Center for Modern Diagnostics, Bremen, Germany

The Owner on Behalf of Turkish Society of Nuclear Medicine

Prof. Murat Fani Bozkurt, MD.

FEBNM Hacettepe University, Medical School,
Department of Nuclear Medicine, Ankara, Türkiye
E-mail: fanibozkurt@gmail.com
ORCID ID: 0000-0003-2016-2624

Publishing Manager

Prof. Murat Fani Bozkurt, MD.

FEBNM Hacettepe University, Medical School,
Department of Nuclear Medicine, Ankara, Türkiye
E-mail: fanibozkurt@gmail.com
ORCID ID: 0000-0003-2016-2624

Editor in Chief

Prof. Murat Fani Bozkurt, MD.

FEBNM Hacettepe University, Medical School,
Department of Nuclear Medicine, Ankara, Türkiye
E-mail: fanibozkurt@gmail.com
ORCID ID: 0000-0003-2016-2624

Associate Editors

Prof. Tanju Yusuf Erdil, MD.

Marmara University Medical School,
Department of Nuclear Medicine, İstanbul, Türkiye
E-mail: yerdil@marmara.edu.tr
ORCID ID: 0000-0002-5811-4321

Prof. Nalan Selçuk, MD.

Yeditepe University, Medical School,
Department of Nuclear Medicine, İstanbul, Türkiye
E-mail: nalanselcuk@yeditepe.edu.tr
ORCID ID: 0000-0002-3738-6491

Statistics Editors

Prof. Gül Ergör, MD.

Dokuz Eylül University, Medical School,
Department of Public Health, İzmir, Türkiye
E-mail: gulergor@deu.edu.tr

Prof. Sadettin Kılıçkap, MD.

Hacettepe University, Medical School,
Department of Preventive Oncology, Ankara, Türkiye
E-mail: skilickap@yahoo.com

English Language Editor

Galenos Publishing House

Lars Friberg

University of Copenhagen Bispebjerg Hospital, Department of Nuclear Medicine, Copenhagen, Denmark

Jørgen Frøkiær

Aarhus University Hospital, Clinic of Nuclear Medicine and PET, Aarhus, Denmark

Maria Lyra Georgosopoulou

University of Athens, 1st Department of Radiology, Aretaieion Hospital, Radiation Physics Unit, Athens, Greece

Gevorg Gevorgyan

The National Academy of Sciences of Armenia, H. Buniatian Institute of Biochemistry, Yerevan, Armenia

Seza Güleç

Florida International University Herbert Wertheim College of Medicine, Departments of Surgery and Nuclear Medicine, Miami, USA

Liselotte Højgaard

University of Copenhagen, Department of Clinical Physiology, Nuclear Medicine and PET, Rigshospitalet, Copenhagen, Denmark

Ora Israel

Tel Aviv University Sackler Medical School, Assaf Harofeh Medical Center, Clinic of Otolaryngology-Head and Neck Surgery, Haifa, Israel

Csaba Juhasz

Wayne State University Medical School, Children's Hospital of Michigan, PET Center and Translational Imaging Laboratory, Detroit, USA

Gamze Çapa Kaya

Dokuz Eylül University, Medical School, Department of Nuclear Medicine, İzmir, Türkiye

Metin Kır

Ankara University, Medical School, Department of Nuclear Medicine, Ankara, Türkiye

Irena Dimitrova Kostadinova

Alexandrovska University Hospital, Clinic of Nuclear Medicine, Sofia, Bulgaria

Lale Kostakoğlu

The Mount Sinai Hospital, Clinic of Nuclear Medicine, New York, USA

Rakesh Kumar

All India Institute of Medical Sciences, Department of Nuclear Medicine, New Delhi, India

Georgios S. Limouris

Athens University, Medical School, Department of Nuclear Medicine, Athens, Greece

Luigi Mansi

Second University of Naples, Medical School, Department of Nuclear Medicine, Naples, Italy

Yusuf Menda

University of Iowa Health Care, Carver College of Medicine, Department of Radiology, Iowa City, USA

Vladimir Obradović

University of Belgrade, Faculty of Organizational Sciences, Department of Human Development Theory, Business Administration, Organizational Studies, Belgrade, Serbia

Zehra Özcan

Ege University Faculty of Medicine, Department of Nuclear Medicine, İzmir, Türkiye

Yekta Özer

Hacettepe University, Faculty of Pharmacy, Department of Radiopharmaceutical, Ankara, Türkiye

Francesca Pons

Hospital Clinic, Clinic of Nuclear Medicine, Barcelona, Spain

Monica Rossleigh

Sydney Children's Hospital, Clinic of Nuclear Medicine, Sydney, Australia

Dragana Sobic Saranovic

University of Belgrade, Medical School, Departments of Radiology, Oncology and Cardiology, Belgrade, Serbia

Mike Sathekge

University of Pretoria, Steve Biko Academic Hospital, Department of Nuclear Medicine, Pretoria, South Africa

Kerim Sönmezöğlü

İstanbul University, Cerrahpaşa Medical School, Department of Nuclear Medicine, İstanbul, Türkiye

Zsolt Szabo

The Johns Hopkins Hospital, Divisions of Radiology and Radiological Science, Baltimore, USA

Istvan Szilvasi

Semmelweis University, Medical School, Department of Nuclear Medicine, Budapest, Hungary

Berna Okudan Tekin

Ankara Numune Training and Research Hospital, Clinic of Nuclear Medicine, Ankara, Türkiye

Mathew L. Thakur

Thomas Jefferson University, Department of Radiology, Pennsylvania, USA

Bülent Turgut

Cumhuriyet University, Medical School, Department of Nuclear Medicine, Sivas, Türkiye

Turgut Turoğlu

Marmara University, Medical School, Department of Nuclear Medicine, İstanbul, Türkiye

Gülün Uçmak

University of Health Sciences Türkiye, Ankara Oncology Training and Research Hospital, Clinic of Nuclear Medicine, Ankara, Türkiye

Doğangün Yüksel

Pamukkale University, Medical School, Department of Nuclear Medicine, Denizli, Türkiye

Turkish Society of Nuclear Medicine

Cinnah Caddesi Pilot Sokak No: 10/12 Çankaya 06650 Ankara, Türkiye Phone: +90 312 441 00 45 Fax: +90 312 441 12 95 Web: www.tsnm.org E-mail: dernekmerkezi@tsnm.org

"Formerly Turkish Journal of Nuclear Medicine"

Reviewing the articles' conformity to the publishing standards of the Journal, typesetting, reviewing and editing the manuscripts and abstracts in English, creating links to source data, and publishing process are realized by Galenos.

**Publisher Contact**

Address: Molla Gürani Mah. Kaçamak Sk. No: 21/1 34093 İstanbul, Türkiye

Phone: +90 (530) 177 30 97 / +90 539 307 32 03

E-mail: info@galenos.com.tr/yayin@galenos.com.tr

Web: www.galenos.com.tr

Publisher Certificate Number: 14521

Online Publication Date: October 2024

ISSN: 2146-1414 E-ISSN: 2147-1959

International scientific journal published quarterly.

MIRT

Molecular Imaging and Radionuclide Therapy

Please refer to the journal's webpage (<https://mirt.tsnmjournals.org/>) for "Aims and Scope", "Instructions to Authors" and "Ethical Policy".

The editorial and publication process of Molecular Imaging and Radionuclide Therapy are shaped in accordance with the guidelines of ICMJE, WAME, CSE, COPE, EASE, and NISO. The journal is in conformity with the Principles of Transparency and Best Practice in Scholarly Publishing.

Molecular Imaging and Radionuclide Therapy is indexed in **Pubmed, Pubmed Central (PMC), Emerging Sources Citation Index (ESCI), TUBITAK-ULAKBIM, Scopus, Gale/Cengage Learning, EBSCO databases, ProQuest Health & Medical Complete, CINAHL, Embase, J-Gate, IdealOnline, Türkiye Atıf Dizini-Türkiye Citation Index, Turk Medline, Hinari, GOALI, ARDI, OARE, AGORA** and **CNKI**.

The journal is published electronically.

Owner: Murat Fani Bozkurt on Behalf of Turkish Society of Nuclear Medicine

Responsible Manager: Murat Fani Bozkurt



CONTENTS

Original Articles

- 138** Deep-learning-based Attenuation Correction for ^{68}Ga -DOTATATE Whole-body PET Imaging: A Dual-center Clinical Study
 ^{68}Ga -DOTATATE Tüm Vücut PET Görüntüleme için Derin Öğrenme Tabanlı Atenüasyon Düzeltmesi: Çift Merkezli Bir Klinik Çalışma
Mahsa Sobhi Lord, Jalil Pirayesh Islamian, Negisa Seyyedi, Rezvan Samimi, Saeed Farzanehfaz, Mahsa Shahrbabki, Peyman Sheikhzadeh; Tabriz, Tehran, Iran
- 147** Impacts of ^{18}F -FDG PET/CT Parameters on Differential Diagnosis and Outcome of Patients with Primary Invasive Mucinous and Lepidic Predominant Adenocarcinoma of the Lung
 ^{18}F -FDG PET/CT Parametrelerinin Primer İnvaziv Müsinöz ve Lepidik Baskın Akciğer Adenokarsinomlu Hastaların Ayırıcı Tanısı ve Sonuçları Üzerindeki Etkileri
Ebru Tatçı, Özlem Özmen, Derya Kızılgöz, Funda Demirağ, Seçkin Bilgiç; Ankara, Kocaeli, Türkiye
- 156** Assessment of Y-90 Radioembolization Treatment Response for Hepatocellular Carcinoma Cases Using MRI Radiomics
MRG Radiomics Kullanılarak Hepatosellüler Karsinom Olgularında Y-90 Radyoembolizasyon Tedavisine Yanıtın Değerlendirilmesi
Mennaallah Mahmoud, Ko-Han Lin, Rheun-Chuan Lee, Chien-an Liu; Taipei, Taiwan
- 167** Prognostic Importance of ^{18}F -FDG Positron Emission Tomography in Uterine Cervical Cancer
Uterin Serviks Kanserinde ^{18}F -FDG Pozitron Emisyon Tomografisinin Prognostik Önemi
Çiğdem Soydal, Muhammet Halil Baltacıoğlu, Mine Araz, Burak Demir, Ecenur Dursun, Salih Taşkın, Nuriye Özlem Küçük, Fırat Ortaç; Ankara, Trabzon, Türkiye
- 174** Cooccurrence of Capsular Liver Lesions Along with Peritoneal Carcinomatosis and Hematogenous Metastases in Ovarian Cancer Patients on Consecutive ^{18}F -FDG PET/CT Studies
Ardışık ^{18}F -FDG PET/CT İncelemeleri Olan Over Kanseri Hastalarındaki Kapsüler Karaciğer Lezyonlarının, Peritoneal Karsinomatozis ve Hematojen Metastazlar ile Birlikteliği
Kemal Ünal, Levent Güner, Erkan Vardareli; İstanbul, Türkiye
- 179** An Unusual Case of Oligometastases in a Patient with Renal Cell Carcinoma: Insights from ^{18}F -FDG PET/CT
Renal Hücreli Karsinomlu Bir Hastada Olağandışı Bir Oligometastaz Olgusu: ^{18}F -FDG PET/CT'nin Faydası
Akram Al-Ibraheem, Ahmed Saad Abdulkadir, Batool Albalooshi, Alaa' Abufara, Kamal Al-Rabi; Amman, Jordan; Dubai, United Arab Emirates; Amman, Jordan
- 182** ^{18}F -FDG PET/CT and ^{68}Ga -DOTATATE PET/CT Findings of Polycystic Kidney-derived Paraganglioma
Polikistik Böbrek Kaynaklı Paragangliomanın ^{18}F -FDG PET/CT ve ^{68}Ga -DOTATATE PET/CT Bulguları
Zehranur Tosunoğlu, Sevim Baykal Koca, Nurhan Ergül, Tevfik Fikret Çermik, Esra Arslan; İstanbul, Türkiye
- 185** Testicular Incidentaloma on ^{18}F -choline PET/CT in a Patient with Prostatic Adenocarcinoma
Prostatik Adenokarsinomlu Bir Hastada ^{18}F -kolin PET/CT ile Saptanan Testiküler İnsidentaloma
Chaymae Bensaïd, Salah Oueriagli Nabih, Meryem Aboussabr, Omar Ait Sahel, Yassir Benameur, Abderrahim Doudouh; Rabat, Morocco
- 189** ^{18}F -FDG PET/CT Correctly Differentiates Idiopathic Pericarditis from Recurrent Lymphoma in a Patient with Primary Mediastinal Lymphoma
 ^{18}F -FDG PET/CT, Primer Mediastinal Lenfomalı Bir Hastada İdiyopatik Perikarditi Tekrarlayan Lenfomadan Doğru Şekilde Ayırt Eder
Sira Vachatanont, Chanittha Buakhao, Napisa Bunnag; Bangkok, Thailand

CONTENTS

- 193** A Case of Diffuse Infiltrative Hepatocellular Carcinoma with Marked Response to Sorafenib Treatment Evidenced by ^{18}F -FDG PET/MRI
 ^{18}F -FDG PET/MRG ile Sorafenib Tedavisine Belirgin Yanıt Verdiđi Gösterilen Diffüz İnfiltratif Hepatosellüler Karsinom Olgusu
Elgin Özkan, Burak Demir, Diđdem Kuru Öz, Yüksel Ürün, Nuriye Özlem Küçük; Ankara, Türkiye
- 196** Distinguishing Bronchial Carcinoid from Benign Bronchocele using ^{68}Ga -DOTATOC PET/CT Imaging
 ^{68}Ga -DOTATOC PET/BT Görüntüleme Kullanılarak Bronşiyal Karsinoidin Benign Bronkoselden Ayrılması
Akram Al-Ibraheem, Raghad Alhouwari, Baraa Alsyof, Ahmed Saad Abdlkadir, Hussam Haddad; Amman, Jordan
- 199** Paget's Disease Mimicking Prostate Cancer Metastasis with ^{68}Ga -PSMA PET/CT
 ^{68}Ga -PSMA PET/BT'de Prostat Kanseri Metastazını Taklit Eden Paget Hastalığı
Melis Oflas, Emine Gökner Işık, Zeynep Gözde Özkan, Duygu Has Şimşek, Yasemin Şanlı; İstanbul, Türkiye
- 203** Bone Marrow Necrosis with Underlying Skeletal Lymphoma Evaluated by ^{18}F -FDG PET/CT and MRI
 ^{18}F -FDG PET/BT ve MRG ile Saptanan Altta Yatan İskelet Lenfomasına Bağlı Kemik İliđi Nekrozu
Le Song, Hui Li, Weifang Zhang; Beijing, China
- 206** Multiple Bone Involvement in Low-grade Myofibroblastic Sarcoma Demonstrated on ^{18}F -FDG PET/CT
Düşük Dereceli Miyofibroblastik Sarkomda ^{18}F -FDG PET/BT'de Gösterilen Çoklu Kemik Tutulumu
Hui Li, Xiaoyan Hou, Na Guo, Le Song, Weifang Zhang; Beijing, China
- 209** Intrathyroidal Parathyroid Adenoma
İntratiroidal Paratiroid Adenomu
Sara Zougari, Mohamed Aziz Bsis, Aboubaker Matrane, Abdelouahed Marrat, Ibtissam Zrara Touit; Marrakesh, Morocco
- 211** Tc-99m-MDP Uptake in Extrasosseous Metastases from Ovarian Papillary Serous Adenocarcinoma
Over Papiller Seröz Adenokarsinomuna Bağlı Ekstraosseöz Metastazlarda Tc-99m-MDP Tutulumu
Komal Bishnoi, Kanhaiyalal Agrawal, P. Sai Sradha Patro, Girish Kumar Parida; Bhubaneswar, India

Indexes

- 2024 Referee Index / 2024 Hakem Dizini
2024 Author Index / 2024 Yazar Dizini
2024 Subject Index / 2024 Konu Dizini



Deep-learning-based Attenuation Correction for ^{68}Ga -DOTATATE Whole-body PET Imaging: A Dual-center Clinical Study

^{68}Ga -DOTATATE Tüm Vücut PET Görüntüleme için Derin Öğrenme Tabanlı Atenüasyon Düzeltmesi: Çift Merkezli Bir Klinik Çalışma

✉ Mahsa Sobhi Lord¹, ✉ Jalil Pirayesh Islamian¹, ✉ Negisa Seyyedi², ✉ Rezvan Samimi³, ✉ Saeed Farzanehfara⁴,
✉ Mahsa Shahrbabki⁵, ✉ Peyman Sheikhzadeh^{4,5}

¹Tabriz University of Medical Sciences School of Medicine, Department of Medical Physics, Tabriz, Iran

²Iran University of Medical Sciences, Nursing and Midwifery Care Research Center, Tehran, Iran

³Shahid Beheshti University, Department of Medical Radiation Engineering, Tehran, Iran

⁴Tehran University of Medical Sciences Faculty of Medicine, Imam Khomeini Hospital Complex, Department of Nuclear Medicine, Tehran, Iran

⁵Tehran University of Medical Sciences Faculty of Medicine, Department of Medical Physics and Biomedical Engineering, Tehran, Iran

Abstract

Objectives: Attenuation correction is a critical phenomenon in quantitative positron emission tomography (PET) imaging with its own special challenges. However, computed tomography (CT) modality which is used for attenuation correction and anatomical localization increases patient radiation dose. This study was aimed to develop a deep learning model for attenuation correction of whole-body ^{68}Ga -DOTATATE PET images.

Methods: Non-attenuation-corrected and computed tomography-based attenuation-corrected (CTAC) whole-body ^{68}Ga -DOTATATE PET images of 118 patients from two different imaging centers were used. We implemented a residual deep learning model using the NiftyNet framework. The model was trained four times and evaluated six times using the test data from the centers. The quality of the synthesized PET images was compared with the PET-CTAC images using different evaluation metrics, including the peak signal-to-noise ratio (PSNR), structural similarity index (SSIM), mean square error (MSE), and root mean square error (RMSE).

Results: Quantitative analysis of four network training sessions and six evaluations revealed the highest and lowest PSNR values as (52.86 ± 6.6) and (47.96 ± 5.09) , respectively. Similarly, the highest and lowest SSIM values were obtained (0.99 ± 0.003) and (0.97 ± 0.01) , respectively. Additionally, the highest and lowest RMSE and MSE values fell within the ranges of (0.0117 ± 0.003) , (0.0015 ± 0.000103) , and (0.01072 ± 0.002) , $(0.000121\pm 5.07\text{e}^{-5})$, respectively. The study found that using datasets from the same center resulted in the highest PSNR, while using datasets from different centers led to lower PSNR and SSIM values. In addition, scenarios involving datasets from both centers achieved the best SSIM and the lowest MSE and RMSE.

Conclusion: Acceptable accuracy of attenuation correction on ^{68}Ga -DOTATATE PET images using a deep learning model could potentially eliminate the need for additional X-ray imaging modalities, thereby imposing a high radiation dose on the patient.

Keywords: Deep-learning, attenuation correction, PET/CT, ^{68}Ga -DOTATATE, medical imaging

Address for Correspondence: Peyman Sheikhzadeh PhD, Tehran University of Medical Sciences Faculty of Medicine, Imam Khomeini Hospital Complex, Department of Nuclear Medicine, Tehran, Iran

Phone: +982161192400 **E-mail:** psh82@yahoo.com, sheikhzadeh-p@sina.tums.ac.ir ORCID ID: orcid.org/0000-0003-3053-2641

Address for Correspondence: Jalil Pirayesh Islamian PhD, Tabriz University of Medical Sciences School of Medicine, Department of Medical Physics, Tabriz, Iran

Phone: +984133364660 **E-mail:** pirayeshj@tbzmed.ac.ir ORCID ID: orcid.org/0000-0001-8628-7564

Received: 24.02.2024 **Accepted:** 05.06.2024 **Epub:** 17.07.2024



Copyright© 2024 The Author. Published by Galenos Publishing House on behalf of the Turkish Society of Nuclear Medicine. This is an open access article under the Creative Commons Attribution-NonCommercial-NoDerivatives 4.0 (CC BY-NC-ND) International License.

Öz

Amaç: Atenuasyon düzeltmesi, kantitatif pozitron emisyon tomografisi (PET) görüntülemeye kendine özgü zorlukları olan kritik bir olgudur. Ancak atenuasyon düzeltmesi ve anatomik lokalizasyonun sağlanması amacıyla kullanılan bilgisayarlı tomografi (BT) yöntemi hastanın aldığı radyasyon dozunu artırmaktadır. Bu çalışmada, tüm vücut ^{68}Ga -DOTATATE PET görüntülerinin atenuasyon düzeltmesi için bir derin öğrenme modelinin geliştirilmesi amaçlandı.

Yöntem: İki farklı görüntüleme merkezinden 118 hastanın atenuasyon düzeltmesiz ve bilgisayarlı tomografi tabanlı atenuasyon düzeltmeli (CTAC) tüm vücut ^{68}Ga -DOTATATE pozitron emisyon tomografi (PET) görüntüleri kullanıldı. NiftyNet çerçevesini kullanarak bir artık derin öğrenme modeli uygulandı. Model, merkezlerden alınan test verileri kullanılarak dört kez eğitildi ve altı kez değerlendirildi. Sentezlenen PET görüntülerinin kalitesi, tepe sinyal-gürültü oranı (PSNR), yapısal benzerlik indeksi (SSIM), ortalama kare hatası (MSE) ve kök ortalama kare hatası (RMSE) dahil olmak üzere farklı değerlendirme ölçümleri kullanılarak PET-CTAC görüntüleriyle karşılaştırıldı.

Bulgular: Dört ağ eğitimi oturumunun ve altı değerlendirmenin kantitatif analizi ile en yüksek ve en düşük PSNR değerlerini sırasıyla ($52,86\pm 6,6$) ve ($47,96\pm 5,09$) olarak elde edildi. Benzer şekilde en yüksek ve en düşük SSIM değerleri sırasıyla ($0,99\pm 0,003$) ve ($0,97\pm 0,01$) olarak elde edildi. Ek olarak, en yüksek ve en düşük RMSE ve MSE değerleri sırasıyla ($0,0117\pm 0,003$), ($0,0015\pm 0,000103$) ve ($0,01072\pm 0,002$), ($0,000121\pm 5,07\text{e}^{-5}$) aralığında kaldı. Çalışma, aynı merkezden gelen veri kümelerinin kullanılmasının en yüksek PSNR değeri ile sonuçlandığını, farklı merkezlerden gelen veri kümelerinin kullanılmasının ise daha düşük PSNR ve SSIM değerleri ile sonuçlandığını buldu. Ayrıca her iki merkezden veri kümelerini içeren senaryolar ile en iyi SSIM ve en düşük MSE ve RMSE elde edildi.

Sonuç: Derin öğrenme modeli kullanılarak ^{68}Ga -DOTATATE PET görüntülerinde atenuasyon düzeltmesinin kabul edilebilir doğruluğu, potansiyel olarak, hastaya yüksek radyasyon dozu uygulanmasına neden olan ek X-ışını görüntüleme yöntemlerine olan ihtiyacı ortadan kaldırılabılır.

Anahtar kelimeler: Derin öğrenme, atenuasyon düzeltmesi, PET/BT, ^{68}Ga -DOTATATE, tıbbi görüntüleme

Introduction

^{68}Ga -DOTATATE positron emission tomography/computed tomography (PET/CT) has emerged as a sensitive and accurate functional imaging method with significant advantages over conventional imaging in the diagnosis and management of neuroendocrine tumors (1,2). In PET imaging, a positron emitter radiopharmaceutical is administered to a patient that emits two 511-keV gamma photons in opposite directions following positron annihilation. However, the gamma pair can undergo photoelectric and Compton interactions before reaching the detector, leading to photon attenuation, poor contrast, and errors in quantitative calculations (3,4).

If the PET images obtained from the standard uptake value (SUV) for diagnosis, prognosis, and treatment-related issues are adequately corrected, it can enable quantitative measures with considerable accuracy (5). The use of CT-based attenuation correction (CTAC) algorithms is considered one of the most common and well-known methods of attenuation correction (AC) in PET (4). The main drawback of these methods is the imposed high effective dose on patients. There was a report in the early days of introducing PET/CT that showed that the average effective dose of patients from whole-body ^{18}F -fluorodeoxyglucose (^{18}F -FDG)-PET/CT examinations was approximately 25 mSv (6). On the other hand, PET radiopharmaceuticals usually have an effective dose of 10 mSv (7). Therefore, the majority of the radiation dose received from imaging is related to CT scans. Because obtaining the tissue attenuation map directly from magnetic resonance imaging (MRI) signals poses challenges, various methods have been employed to address this issue (8,9,10,11,12). One of the

commonly used methods for AC in PET/MRI scanners is the Dixon-based method (9). Nevertheless, a major drawback of this method is its failure to account for bone tissue (10). Consequently, a model-based approach was adopted to address this limitation (11). However, this method introduces a quantification error due to inconsistent registration (12). The inconsistency and small field of view of MRI compared with PET can result in the loss of information from certain body parts (13). Meanwhile, the maximum likelihood reconstruction of activity and attenuation (MLAA) algorithm can be used to obtain missing information and create an attenuation map from the PET emission data (14). However, one drawback of this algorithm is the presence of high noise and induced cross-talk artifacts (15). Additionally, atlas-based segmentation methods (16,17,18) have been employed, but they suffer from incorrect classification of tissue, anatomic abnormalities, noise, and metal-induced artifacts, making AC a challenging issue in PET/MRI (19). In recent years, deep learning has demonstrated great potential in enhancing medical image quality, denoising, and artifact reduction (20,21). So far, deep learning has been used in producing synthetic CT using MRI images for AC in PET (22), including direct transformation to pseudo-CT from T1-weighted MR, ultrashort echo time, zero-TE MR, Dixon, estimation of AC factors from time-of-flight data (23,24,25,26,27), generation of synthetic CT images from non-AC (NAC) PET images on whole-body PET/MRI imaging, and MLAA-based AC maps (28,29,30). However, there is a need for structural images, and accuracy is compromised by image artifacts from misregistration and inter-modality errors (31). Several studies have attempted to directly convert NAC PET images to corrected PET images

without the need for multiple imaging modalities such as MRI and CT (31,32). These studies employed different approaches and models in different areas of the body and with different radiopharmaceuticals.

In the present study, we aimed to develop an optimal deep-learning model for AC of whole-body ⁶⁸Ga-DOTATATE PET images without relying on anatomical structures.

Materials and Methods

Data Acquisition

⁶⁸Ga-DOTATATE whole-body PET images of 118 patients from two imaging centers (59 images from center 1 and 59 images from center 2) were retrospectively included in the study. This study was approved by the Research Ethics Committee of Tabriz University of Medical Sciences (approval no.: IR.TBZMED.REC.1401.584, approval date: 03.10.2022), which ensures adherence to ethical standards. The examinations were performed using 5-ring BGO-based PET/CT and 3-ring LSO-based PET/CT scanners. PET imaging was performed approximately 60 min after injection of 1.85 MBq ⁶⁸Ga-DOTATATE per kilogram of patient weight. Before radiotracer injection, a low-dose CT scan was performed for AC and anatomical localization.

Data Preprocessing

From the 118 ⁶⁸Ga-DOTATATE PET images, 85% of the data from each center were considered for training the model, while 15% were used for external validation. In addition, 15% of the training dataset was set aside for validation during the training process to evaluate the loss function

and prevent overfitting. To reduce the dynamic range of image intensity, all PET images, including CTAC and NAC images, were converted to SUVs. In addition, to reduce the computational load, the image intensities were normalized by an empirical fixed value of 9 and 3, respectively.

Network Architecture

A deep learning algorithm based on the NiftyNet platform was utilized to generate PET/CT image AC using reference (PET-CTAC) images. NiftyNet is an infrastructure built upon the TensorFlow library and is designed to be used in various image analysis programs. It supports segmentation, regression, image generation, and reconstruction tasks. Therefore, it plays a vital and fundamental role in speeding up clinical work, including diagnostic and therapeutic procedures (33). The NiftyNet platform is a high-resolution residual neural network (HighResNet) (34). Our prepared network was composed of 20 residual layers. In the first seven layers, a 3x3x3 voxel kernel is employed to encode low-level image features, such as edges and corners. This kernel is dilated by factors of 2 and 4 in subsequent layers to extract mid- and high-level features. Then, a residual connection is used to link all two layers. In the residual blocks, each layer comprises an element-wise rectified linear unit (ReLU) and batch normalization. The structural details of the model are shown in Figure 1.

Implementation Details

In this study, we used the following parameters to train the network: lr=0.001, activation function=leakyReLU, loss

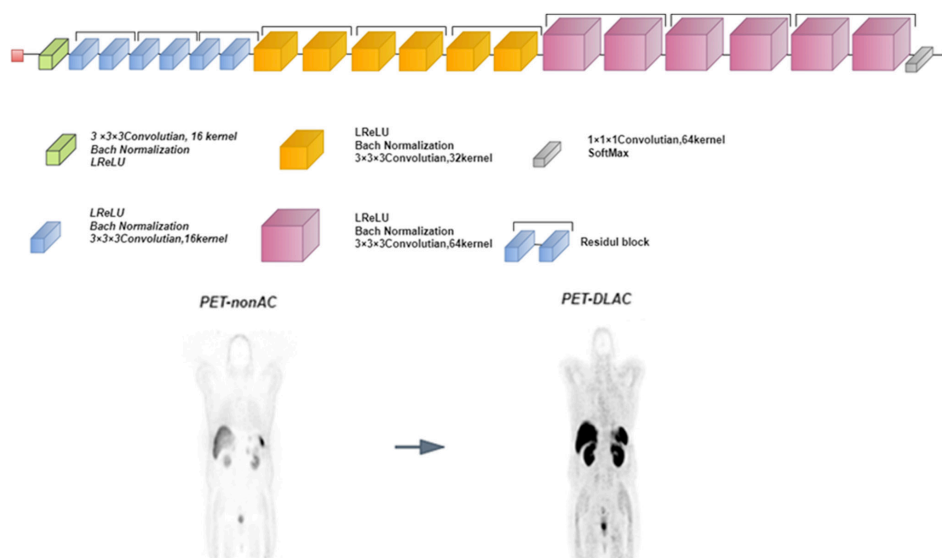


Figure 1. Illustrates the intricacies of the architecture used in the ResNet model. This model is designed to take PET-non-AC images as input and generate PET-DLAC images as output
 PET-non-AC: Positron emission tomography non attenuation correction, PET-DLAC: PET deep learning attenuation correction

function=l2 loss, optimizer=Adam, decay factor=0.00001, batch size=12, queue length=480. The model was trained four times but was evaluated six times using test datasets with different matrix sizes.

Initially, a dataset comprising 50 samples from center 1 with a matrix size of 192x192 was used to train the network. However, the test was separately conducted using 9 images from each center, namely, center 1 and 2 test datasets for the first and second evaluations, with a matrix size of 192x192. Specifically, the matrix size of 9 test datasets from center 2 was resized from 200x200 to 192x192.

The second training was performed using only 50 data samples from center 2, with a matrix size of 192x92. The model was then tested using 9 datasets from both centers, i.e., center 1 and 2 test datasets for the third and fourth evaluations, with a matrix size of 192x192. For the third training phase, a total of 100 samples were used to train the network with 50 data from each center and a matrix size of 192x192. Additionally, 18 samples (9 datasets from each center) were used as the test dataset in the fifth evaluation. For the fourth training session of the network, a dataset of 100 samples from both centers was used, with a matrix size of 200x200. The matrix size of the 50 images from center 1 was resized from 192x192 to 200x200. Eighteen data points were utilized for network testing from both centers, as the sixth evaluation with a matrix size of 200x200.

Statistical Analysis

In this study, we performed statistical analyses to explore the relationship between the two variables. Specifically, we utilized the Pearson correlation coefficient to assess the type of connection, and the paired sample t-test to calculate the p-value. Additionally, we computed several evaluation metrics, including peak signal-to-noise ratio (PSNR), structural similarity index (SSIM), mean squared error (MSE), and root mean squared error (RMSE) for parameters such as the view signal-to-noise peak ratio, structural similarity, and average error rate.

Evaluation Strategy

The performance of the prepared model was assessed using various quantitative metrics, including quantitative metrics such as PSNR (Eq.1), MSE (Eq.2), RMSE (Eq.3), and SSIM (Eq.4). The metrics were computed by comparing the reference PET-CTAC images with the images generated by the network [PET-deep learning AC (PET-DLAC)]. The metrics are defined as follows:

$$PSNR = 10 \log_{10} \left(\frac{R^2}{MSE} \right) \quad (1)$$

$$MSE = \frac{1}{n} \sum_{i=1}^n (PET_{predict}(i) - PET_{ref}(i))^2 \quad (2)$$

$$RMSE = \sqrt{\frac{1}{n} \sum_{i=1}^n (PET_{predict}(i) - PET_{ref}(i))^2} \quad (3)$$

$$SSIM = \frac{(2\mu_{ref}\mu_{pre} + c_1)(2\sigma_{ref,pre} + c_2)}{(\mu_{ref}^2 + \mu_{pre}^2 + c_1)(\sigma_{ref}^2 + \sigma_{pre}^2 + c_2)} \quad (4)$$

where in Equation (Eq.) (1), R^2 represents the maximum value of the PET-CTAC images as the reference image, represents the predicted image, and MSE denotes the mean squared error. In Eq. (2), "n" indicates the number of voxels inside the region of interest, "i" denotes the voxel index, $pet_{predict}$ stands for AC PET images, and pet_{ref} stands for the reference PET-CTAC images.

In Eq. (4), μ_{ref} and μ_{pre} represent the mean values of the reference and predicted PET images, respectively, σ_{ref} and σ_{pre} are the variances of the pet_{ref} and $pet_{predict}$ images, where $\sigma_{ref,pre}$ represents their covariance. Additionally, c_1 and c_2 are two parameters with constants $c_1 = 0.01$ and $c_2 = 0.02$ in Eq. (3), respectively, to avoid division by very small values.

Furthermore, to illustrate the voxel-wise distribution of radiotracer uptake correlation between PET-CTAC and PET-DLAC images, a joint histogram analysis was performed for SUV values ranging from 0.1 to 18 using 200 bins.

Results

The summary of the mean \pm standard deviation of the image quantitative assessment parameters, including MSE, PSNR, RMSE, and SSIM, that were calculated between the SUV of PET-CTAC images as the reference and the 18 test datasets predicted by the model for the six evaluations, are demonstrated in Table 1. Although the values of these parameters in all evaluations were acceptable, there were some variations among them. Among all evaluations, the fourth evaluation obtained the highest PSNR value (52.86 \pm 6.6), indicating a better representation of image quality. The third evaluation showed the lowest PSNR (47.96 \pm 5.09), and the fifth evaluation had the lowest MSE value (0.000121 \pm 5.07 $\times 10^{-5}$) and RMSE (0.01072 \pm 0.002) value, indicating a smaller deviation from the reference images. The second evaluation demonstrated the highest MSE (0.0015 \pm 0.000103) and RMSE (0.0117 \pm 0.003). Additionally, the sixth evaluation showed the highest SSIM level (0.99 \pm 0.003) among all evaluations, while the second evaluation showed the lowest SSIM level (0.97 \pm 0.01)

compared to the reference images. A box plot comparing the parameters in the six evaluations is shown in Figure 2. Furthermore, we calculated the maximum SUV (SUV_{max}) difference between PET-CTAC and PET-DLAC images in 20 superficial regions of interest (ROIs) and 20 deep ROIs in

the axial section along the x-axis for each evaluation. For all evaluations p-value <0.05, Only for some evaluations where the original size of the images had been changed such as the sixth evaluation p-value >0.05. Additionally, the SUV_{max} difference was calculated for 5 ROIs within the tumor

Table 1. The results of quantitative analysis of the predicted (PET-DLAC) and the reference (PET-CTAC) images that were calculated for 6 evaluations

Evaluation	PSNR	SSIM	MSE	RMSE
1	48.22±6.16	0.98±0.005	0.00013±0.000102	0.0110±0.0035
2	49.53±6.81	0.97±0.01	0.0015±0.000103	0.0117±0.003
3	47.96±5.09	0.98±0.009	0.00013 ±7.7xe ⁻⁵	0.0112±0.0037
4	52.86±6.6	0.98±0.019	0.000125±7.5xe ⁻⁵	0.01073±0.0033
5	50.5±6.52	0.97±0.02	0.000121±0.000050	0.01072±0.002
6	49.89±5.68	0.99±0.003	0.00014±6.6xe ⁻⁵	0.0116±0.0029

PET-DLAC: Positron emission tomography deep learning attenuation correction, PET-CTAC: Positron emission tomography computed tomography-based attenuation correction, PSNR: Peak signal-to-noise ratio, SSIM: Structural similarity index, MSE: Mean square error, RMSE: Root mean square error

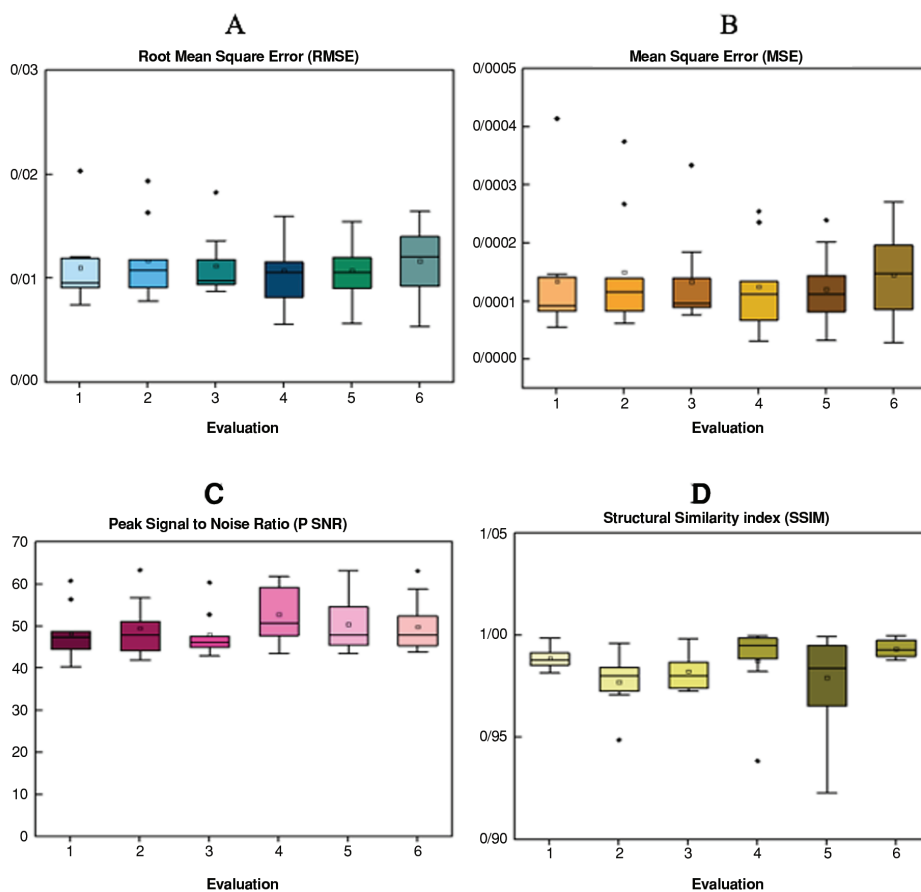


Figure 2. Boxplot displaying image quantitative metrics calculated between PET-CTAC, as the reference, and PET-DLAC, as the predicted image. The metrics include RMSE (A), MSE (B), PSNR (C), and SSIM (D) for six evaluations

PET-DLAC: Positron emission tomography deep learning attenuation correction, PET-CTAC: Positron emission tomography computed tomography-based attenuation correction, PSNR: Peak signal-to-noise ratio, SSIM: Structural similarity index, MSE: Mean square error, RMSE: Root mean square error

volumes for each evaluation in the axial section along the y-axis, for the first, fourth, and fifth evaluations p-value <0.05 . The coronal views of the NAC, PET-CTAC, and PET-DLAC images, as well as the bias map between PET-CTAC and PET-DLAC images, are shown in Figures 3 and 4. The images represent the results of the four training sessions performed on the image represents the nine test data from two imaging centers. In all nine test data related to the four train sets, errors and underestimations were visually observed compared to the reference images. In particular, where the matrix size of images was set to 200×200 , the rate of underestimation increased, and it should be noted that center 2 had data of the same matrix size. However,

when the matrix size of 192×192 , the underestimation was at its lowest level. Additionally, by reducing the size of the images, the number of errors observed in the lungs was significantly reduced; thus, images related to center 2 in the second training set showed the lowest number of errors and underestimation. These images were created using only data from the same center and were resized to 192×192 pixels. In general, most images exhibited the highest amount of error in the lungs, while the liver, kidneys, and bladder images exhibited the highest amount of underestimation. The joint histogram in Figure 5 reveals that there was the highest voxel-wise similarity between PET-CTAC and PET-DLAC images in the first evaluation and

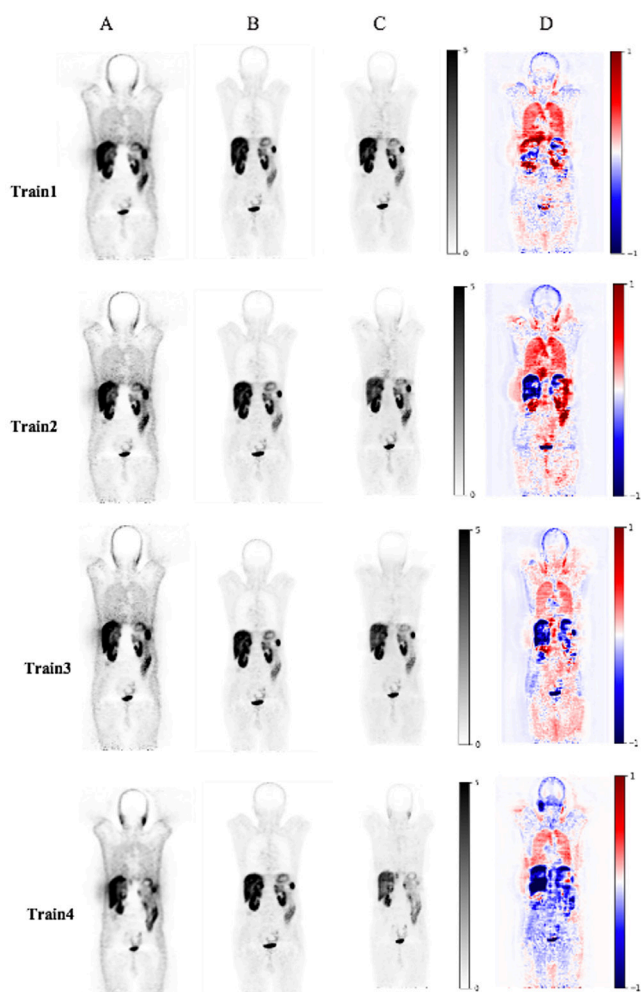


Figure 3. Coronal view of NAC (A), PET-CTAC (B), PET-DLAC images (C), and the calculated bias map between PET-CTAC and PET-DLAC images (D) at the imaging center 1

PET-DLAC: Positron emission tomography deep learning attenuation correction, PET-CTAC: Positron emission tomography computed tomography-based AC, NAC: Non-attenuation correction

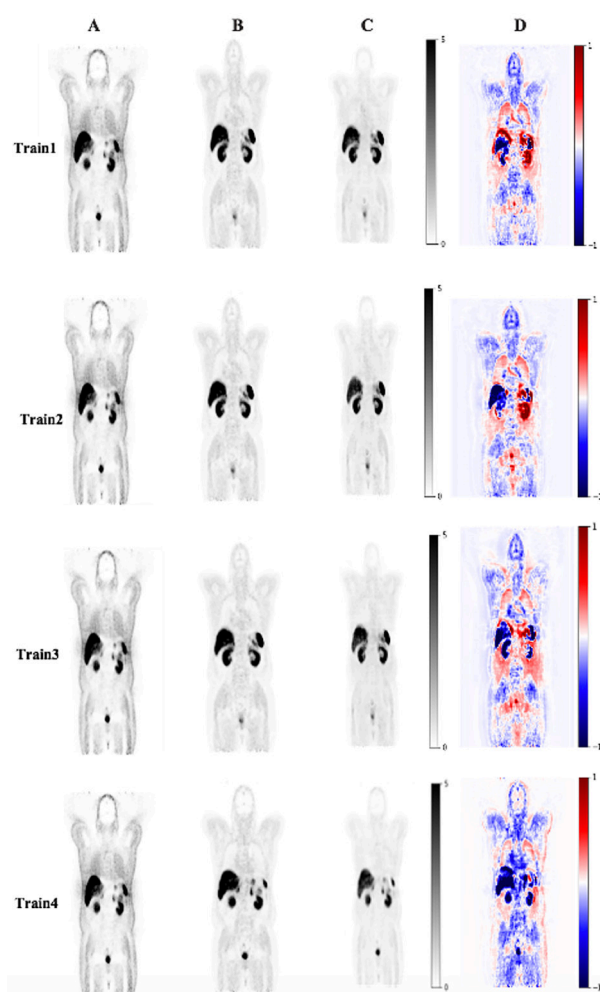


Figure 4. Coronal view of NAC (A), PET-CTAC (B), PET-DLAC images (C), and the calculated bias map between PET-CTAC and PET-DLAC images (D) at the imaging center 2

PET-DLAC: Positron emission tomography deep learning attenuation correction, PET-CTAC: Positron emission tomography computed tomography-based AC, NAC: Non-attenuation correction

first training within the data from center1, $R^2=0.95$, and a curve slope of 1.10. In contrast, for the fourth evaluation related to the second train, the correlation coefficient remained high at $R^2=0.95$, but the slope was slightly lower at 0.95. The lowest R^2 value of 0.82 was observed in the second evaluation, which is related to the first training. In this case, the training dataset was obtained from center 1, and the test dataset was obtained from center 2. Both datasets were resized to match the size of the training

dataset. In summary, joint histogram analysis revealed a significant level of similarity between PET-CTAC and PET-DLAC images.

Discussion

In this study, we used a deep learning model for the AC of whole-body ^{68}Ga -DOTATATE PET images without the need for structural information. The model was also evaluated using training and test datasets from

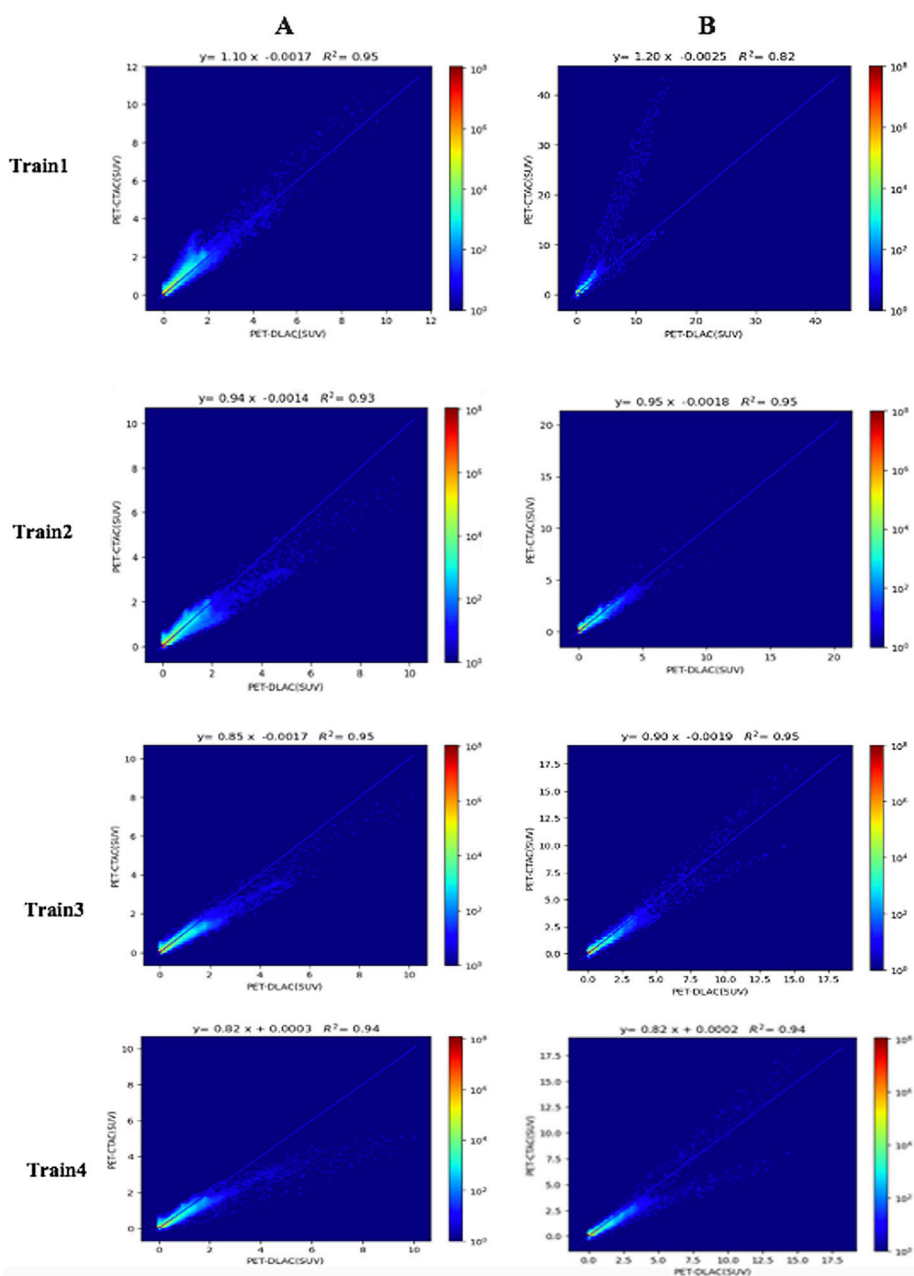


Figure 5. Joint histogram resulting from four network training sessions conducted using test datasets from the imaging center 1 (A) and 2 (B)

two distinct imaging centers to assess and enhance its performance. In recent years, there has been a significant concern about AC in PET images using deep learning methods. Many studies have been conducted to generate pseudo-CT images using MRI (22,23,24,25,26,27) or NAC images (28,29) for AC purposes, but these methods require an additional modality as well as insufficient accuracy due to the large mismatch of images between the two modalities, and many artifacts and errors can be observed between them (31). Hence, there are many studies on PET image AC based on NAC images, without the need for structural images (CT or MRI). Shiri et al. (32) used a deep convolutional encoder-decoder (deep-DAC) network to calculate AC directly for ^{18}F -FDG PET brain images. They achieved promising results on 18 images with a PSNR of 38.7 ± 3.54 and SSIM of 0.988 ± 0.006 , respectively. Dong et al. (31) proposed 3D patch-based cycle-consistent generative adversarial networks (CycleGAN) for AC of ^{18}F -FDG PET whole-body ($n=30$) images and reported an average PSNR of 44.3 ± 3.5 and NMSE of 0.72 ± 0.34 . Likewise, Mostafapour et al. (35) proposed the ResNet model for AC of 46 PET images with ^{68}Ga -PSMA and reported PSNR and SSIM 48.17 ± 2.96 and 0.973 ± 0.034 , respectively. However, to enhance and elevate the accuracy of outcomes, further studies are needed. In this study, we used the Resnet model to obtain ^{68}Ga -DOTATATE PET whole-body images. Our proposed model was trained four times and evaluated six times using 18 test datasets from two imaging centers for ^{68}Ga -DOTATATE PET images with different matrix sizes. In all 18 test data bias maps across six evaluations, high error rates were observed in the lungs, whereas the liver, bladder, and kidneys displayed a marked tendency toward underestimation. It is worth noting that the magnitude of these errors was substantially diminished by decreasing the dimensions of the images. Although the evaluations did not show significant differences, certain errors undoubtedly stemmed from the incomplete AC of the reference images, which cannot be overlooked. It may be advisable to use data from the same center to train the model at a specific center to achieve optimal AC. Additionally, the results indicate that reducing the image matrix size relative to the increase in size can improve model performance. From the viewpoint of image quality, although our model was not comparable with the CTAC approach, it ruled out the radiation dose from CT. However, our promising finding reveals the potential of the model for further exploration on larger datasets with possibly enhanced levels of accuracy in future studies.

Conclusion

This study demonstrated the performance and feasibility of a deep learning model for AC in whole-body ^{68}Ga -DOTATATE PET images. The results indicate the accuracy and high performance of the model, demonstrating its potential for effectively correcting attenuation in PET imaging. It appears that the model can reduce the reliance on CT images for AC of PET images, thereby minimizing additional radiation exposure to the patient.

Acknowledgement: We acknowledge the use of ChatGPT, a language model developed by OpenAI, in enhancing the grammatical accuracy and overall writing quality of this article.

Ethics

Ethics Committee Approval: This study was approved by the Research Ethics Committee of Tabriz University of Medical Sciences (approval no.: IR.TBZMED.REC.1401.584, approval date: 03.10.2022), which ensures adherence to ethical standards.

Informed Consent: Retrospective study.

Authorship Contributions

Concept: J.P.I., N.S., P.S., Design: M.S.L., M.S., P.S., Data Collection or Processing: M.S.L., J.P.I., R.S., S.F., M.S., P.S., Analysis or Interpretation: M.S.L., J.P.I., M.S., P.S., Literature Search: M.S.L., N.S., Writing: M.S.L., J.P.I., N.S., R.S., S.F., M.S., P.S.

Conflict of Interest: No conflict of interest was declared by the authors.

Financial Disclosure: This research is financially supported by a grant from Tabriz University of Medical Sciences, Tabriz, Iran (Grant #70064), under the research ethics ID: IR.TBZMED.REC.1401.584.

References

1. Sanli Y, Garg I, Kandathil A, Kendi T, Zanetti MJB, Kuyumcu S, Subramaniam RM. Neuroendocrine Tumor Diagnosis and Management: ^{68}Ga -DOTATATE PET/CT. *AJR Am J Roentgenol.* 2018;211:267-277.
2. Tirosh A, Kebebew E. The utility of ^{68}Ga -DOTATATE positron-emission tomography/computed tomography in the diagnosis, management, follow-up and prognosis of neuroendocrine tumors. *Future Oncol.* 2018;14:111-122.
3. Zaidi H, Koral KF. Scatter modelling and compensation in emission tomography. *Eur J Nucl Med Mol Imaging.* 2004;31:761-782.
4. Kinahan PE, Hasegawa BH, Beyer T. X-ray-based attenuation correction for positron emission tomography/computed tomography scanners. *Semin Nucl Med.* 2003;33:166-179.
5. Zaidi H, Karakatsanis N. Towards enhanced PET quantification in clinical oncology. *Br J Radiol.* 2018;91:20170508.

6. Brix G, Lechel U, Glatting G, Ziegler SI, Münzing W, Müller SP, Beyer T. Radiation exposure of patients undergoing whole-body dual-modality ¹⁸F-FDG PET/CT examinations. *J Nucl Med.* 2005;46:608-613.
7. Mattsson S, Johansson L, Leide Svegborn S, Liniecki J, Noßke D, Riklund KÅ, Stabin M, Taylor D, Bolch W, Carlsson S, Eckerman K, Giussani A, Söderberg L, Valind S; ICRP Radiation Dose to Patients from Radiopharmaceuticals: a Compendium of Current Information Related to Frequently Used Substances. *Ann ICRP.* 2015;44:7-321.
8. Martinez-Möller A, Nekolla SG. Attenuation correction for PET/MR: problems, novel approaches and practical solutions. *Z Med Phys.* 2012;22:299-310.
9. Berker Y, Franke J, Salomon A, Palmowski M, Donker HC, Temur Y, Mottaghy FM, Kuhl C, Izquierdo-Garcia D, Fayad ZA, Kiessling F, Schulz V. MRI-based attenuation correction for hybrid PET/MRI systems: a 4-class tissue segmentation technique using a combined ultrashort-echo-time/Dixon MRI sequence. *J Nucl Med.* 2012;53:796-804.
10. Koesters T, Friedman KP, Fenchel M, Zhan Y, Hermosillo G, Babb J, Jelescu IO, Faul D, Boada FE, Shepherd TM. Dixon Sequence with Superimposed Model-Based Bone Compartment Provides Highly Accurate PET/MR Attenuation Correction of the Brain. *J Nucl Med.* 2016;57:918-924.
11. Paulus DH, Quick HH, Geppert C, Fenchel M, Zhan Y, Hermosillo G, Faul D, Boada F, Friedman KP, Koesters T. Whole-Body PET/MR Imaging: Quantitative Evaluation of a Novel Model-Based MR Attenuation Correction Method Including Bone. *J Nucl Med.* 2015;56:1061-1066.
12. Hwang D, Kang SK, Kim KY, Seo S, Paeng JC, Lee DS, Lee JS. Generation of PET Attenuation Map for Whole-Body Time-of-Flight ¹⁸F-FDG PET/MRI Using a Deep Neural Network Trained with Simultaneously Reconstructed Activity and Attenuation Maps. *J Nucl Med.* 2019;60:1183-1189.
13. Tang J, Haagen R, Blaffert T, Renisch S, Blaeser A, Salomon A, Schweizer B, Hu Z. Effect of MR truncation compensation on quantitative PET image reconstruction for whole-body PET/MR. 2011 IEEE Nucl Sci Symp Conf Rec. 2011:2506-2509.
14. Nuyts J, Bal G, Kehren F, Fenchel M, Michel C, Watson C. Completion of a truncated attenuation image from the attenuated PET emission data. *IEEE Trans Med Imaging.* 2013;32:237-246.
15. Nuyts J, Dupont P, Stroobants S, Banninck R, Mortelmans L, Suetens P. Simultaneous maximum a posteriori reconstruction of attenuation and activity distributions from emission sinograms. *IEEE Trans Med Imaging.* 1999;18:393-403.
16. Ribeiro AS, Kops ER, Herzog H, Almeida P. Hybrid approach for attenuation correction in PET/MR scanners. *Nucl Instrum Methods Phys Res A: Accelerators, Spectrometers, Detectors and Associated Equipment.* 2014;734:166-170.
17. Mérida I, Reilhac A, Redouté J, Heckemann RA, Costes N, Hammers A. Multi-atlas attenuation correction supports full quantification of static and dynamic brain PET data in PET-MR. *Phys Med Biol.* 2017;62:2834-2858.
18. Hofmann M, Bezrukov I, Mantlik F, Aschoff P, Steinke F, Beyer T, Pichler BJ, Schölkopf B. MRI-based attenuation correction for whole-body PET/MRI: quantitative evaluation of segmentation- and atlas-based methods. *J Nucl Med.* 2011;52:1392-1399.
19. Mehranian A, Arabi H, Zaidi H. Vision 20/20: Magnetic resonance imaging-guided attenuation correction in PET/MRI: Challenges, solutions, and opportunities. *Med Phys.* 2016;43:1130-1155.
20. Chan HP, Samala RK, Hadjiiski LM, Zhou C. Deep Learning in Medical Image Analysis. *Adv Exp Med Biol.* 2020;1213:3-21.
21. Ghafari A, Sheikhzadeh P, Seyyedi N, Abbasi M, Farzenefar S, Yousefirizi F, Ay MR, Rahmim A. Generation of ¹⁸F-FDG PET standard scan images from short scans using cycle-consistent generative adversarial network. *Phys Med Biol.* 2022;67.
22. Han X. MR-based synthetic CT generation using a deep convolutional neural network method. *Med Phys.* 2017;44:1408-1419.
23. Liu F, Jang H, Kijowski R, Bradshaw T, McMillan AB. Deep Learning MR Imaging-based Attenuation Correction for PET/MR Imaging. *Radiology.* 2018;286:676-684.
24. Jang H, Liu F, Zhao G, Bradshaw T, McMillan AB. Technical Note: Deep learning based MRAC using rapid ultrashort echo time imaging. *Med Phys.* 2018;10.1002/mp.12964.
25. Gong K, Yang J, Kim K, El Fakhri G, Seo Y, Li Q. Attenuation correction for brain PET imaging using deep neural network based on Dixon and ZTE MR images. *Phys Med Biol.* 2018;63:125011.
26. Leynes AP, Yang J, Wiesinger F, Kaushik SS, Shanbhag DD, Seo Y, Hope TA, Larson PEZ. Zero-Echo-Time and Dixon Deep Pseudo-CT (ZeDD CT): Direct Generation of Pseudo-CT Images for Pelvic PET/MRI Attenuation Correction Using Deep Convolutional Neural Networks with Multiparametric MRI. *J Nucl Med.* 2018;59:852-858.
27. Arabi H, Zaidi H. Deep learning-guided estimation of attenuation correction factors from time-of-flight PET emission data. *Med Image Anal.* 2020;64:101718.
28. Dong X, Wang T, Lei Y, Higgins K, Liu T, Curran WJ, Mao H, Nye JA, Yang X. Synthetic CT generation from non-attenuation corrected PET images for whole-body PET imaging. *Phys Med Biol.* 2019;64:215016.
29. Reimold M, Nikolaou K, Christian La Fougère M, Gatidis S. 18 Independent brain F-FDG PET attenuation correction using a deep learning approach with Generative Adversarial Networks. *Hell J Nucl Med.* 2019;22:179-186.
30. Shi L, Onofrey JA, Revilla EM, Toyonaga T, Menard D, Ankrah J, Carson RE, Liu C, Lu Y. A novel loss function incorporating imaging acquisition physics for PET attenuation map generation using deep learning. *MICCAI.* 2019. doi: 10.48550/arXiv.1909.01394
31. Dong X, Lei Y, Wang T, Higgins K, Liu T, Curran WJ, Mao H, Nye JA, Yang X. Deep learning-based attenuation correction in the absence of structural information for whole-body positron emission tomography imaging. *Phys Med Biol.* 2020;65:055011.
32. Shiri I, Ghafarian P, Geramifar P, Leung KH, Ghelichoghli M, Oveisi M, Rahmim A, Ay MR. Direct attenuation correction of brain PET images using only emission data via a deep convolutional encoder-decoder (Deep-DAC). *Eur Radiol.* 2019;29:6867-6879.
33. Gibson E, Li W, Sudre C, Fidon L, Shakir DI, Wang G, Eaton-Rosen Z, Gray R, Doel T, Hu Y, Whyntie T, Nachev P, Modat M, Barratt DC, Ourselin S, Cardoso MJ, Vercauteren T. NiftyNet: a deep-learning platform for medical imaging. *Comput Methods Programs Biomed.* 2018;158:113-122.
34. Li W, Wang G, Fidon L, Ourselin S, Cardoso MJ, Vercauteren T. On the compactness, efficiency, and representation of 3D convolutional networks: brain parcellation as a pretext task. *IPMI.* 2017:348-360.
35. Mostafapour S, Gholamiankhah F, Dadgar H, Arabi H, Zaidi H. Feasibility of Deep Learning-Guided Attenuation and Scatter Correction of Whole-Body ⁶⁸Ga-PSMA PET Studies in the Image Domain. *Clin Nucl Med.* 2021;46:609-615.



Impacts of ¹⁸F-FDG PET/CT Parameters on Differential Diagnosis and Outcome of Patients with Primary Invasive Mucinous and Lepidic Predominant Adenocarcinoma of the Lung

¹⁸F-FDG PET/CT Parametrelerinin Primer İnvaziv Müsinöz ve Lepidik Baskın Akciğer Adenokarsinomlu Hastaların Ayırıcı Tanısı ve Sonuçları Üzerindeki Etkileri

✉ Ebru Tatcı¹, ✉ Özlem Özmen¹, ✉ Derya Kızılgöz², ✉ Funda Demirağ³, ✉ Seçkin Bilgiç⁴

¹Ankara Atatürk Sanatorium Training and Research Hospital, Clinic of Nuclear Medicine, Ankara, Türkiye

²Ankara Atatürk Sanatorium Training and Research Hospital, Clinic of Pulmonology, Ankara, Türkiye

³Ankara Atatürk Sanatorium Training and Research Hospital, Clinic of Pathology, Ankara, Türkiye

⁴Kocaeli City Hospital, Clinic of Nuclear Medicine, Kocaeli, Türkiye

Abstract

Objectives: The purpose of this study was to investigate whether ¹⁸F-fluorodeoxyglucose (¹⁸F-FDG) positron emission tomography/computed tomography (PET/CT) parameters have a role in differentiating invasive mucinous lung adenocarcinoma (IMA) from lepidic predominant lung adenocarcinoma (LPA). Additionally, we compared the ¹⁸F-FDG-PET/CT features between survivors and non-survivors.

Methods: Tumors were divided into 2 groups according to CT appearance: Group 1: nodular-type tumor; group 2: mass- or pneumonic-type tumor. Unilateral and bilateral multifocal diseases were detected. Clinicopathological characteristics and PET/CT findings were compared between IMAs and LPAs, as well as between survivors and non-survivors.

Results: We included 43 patients with IMA and 14 with LPA. Tumor size (p=0.003), incidence of mass/pneumonic type (p=0.011), and bilateral lung involvement (p=0.049) were higher in IMAs than in LPAs. IMAs had more advanced T, M, and Tumor, Node, and Metastasis stages than in LPAs (p=0.048, p=0.049, and p=0.022, respectively). There was no statistically significant difference in maximum standardized uptake value (SUV_{max}) between the IMA and LPA (p=0.078). The SUV was significantly lower in the nodular group than in the mass/pneumonic-type group (p=0.0001). A total of 11 patients died, of whom SUV_{max} values were significantly higher in these patients (p=0.031). Male gender (p=0.0001), rate of stage III-IV (p=0.0001), T3-T4 (p=0.021), M1 stages (p=0.0001), multifocality (p=0.0001), and bilateral lung involvement (p=0.0001) were higher in non-survivor.

Conclusions: Although CT images were useful for the differential diagnosis of LPAs and IMAs, SUV_{max} was not helpful for differentiation of these 2 groups. However, both ¹⁸F-FDG uptake and CT findings may play an important role in predicting prognosis in these patients.

Keywords: ¹⁸F-FDG PET/CT, primary invasive mucinous adenocarcinoma of the lung, lepidic predominant adenocarcinoma of the lung

Öz

Amaç: Bu çalışmanın amacı ¹⁸F-florodeoksiglukoz (¹⁸F-FDG) pozitron emisyon tomografisi/bilgisayarlı tomografinin (PET/CT) parametrelerinin invaziv müsinöz akciğer adenokarsinomunu (İMA) lepidik predominant akciğer adenokarsinomundan (LPA) ayırmada bir rolü olup olmadığını araştırmaktır. Ayrıca hayatta kalanlar ve hayatta kalmayanlar arasındaki ¹⁸F-FDG PET/CT özelliklerini karşılaştırdık.

Address for Correspondence: Ebru Tatcı Assoc. Prof., Ankara Atatürk Sanatorium Training and Research Hospital, Clinic of Nuclear Medicine, Ankara, Türkiye

Phone: +90 505 914 53 61 **E-mail:** ebrualkandr@yahoo.com ORCID ID: orcid.org/0000-0002-9216-658X

Received: 13.01.2024 **Accepted:** 23.06.2024 **Epub:** 06.09.2024



Copyright© 2024 The Author. Published by Galenos Publishing House on behalf of the Turkish Society of Nuclear Medicine. This is an open access article under the Creative Commons Attribution-NonCommercial-NoDerivatives 4.0 (CC BY-NC-ND) International License.

Yöntem: Tümörler BT görünümüne göre 2 gruba ayrıldı: Grup 1: Nodüler tip tümör; grup 2: Kitle veya pnömonik tip tümör. Tek taraflı ve iki taraflı multifokal hastalıklar tespit edildi. Klinikopatolojik özellikler ve PET/BT bulguları, İMA'lar ve LPA'ların yanı sıra hayatta kalanlar ve hayatta kalmayanlar arasında karşılaştırıldı.

Bulgular: Kırk üç İMA ve 14 LPA hastasını dahil ettik. Tümör boyutu ($p=0,003$), kitle/pnömonik tip insidansı ($p=0,011$), iki taraflı akciğer tutulumu ($p=0,049$) İMA'larda LPA'lara göre daha yüksekti. İMA'larda LPA'lara göre daha ileri T, M ve Tümör, Nod ve Metastaz evreleri vardı (sırasıyla $p=0,048$, $p=0,049$ ve $p=0,022$). İMA'lar ve LPA arasında maksimum standardize tutulum değeri (SUV_{maks}) açısından istatistiksel olarak anlamlı bir fark yoktu ($p=0,078$). SUV, nodüler grupta kitle/pnömonik tip gruba göre anlamlı derecede düştü ($p=0,0001$). Toplam 11 hasta öldü ve bu hastalarda SUV_{maks} değerleri anlamlı derecede yüksekti ($p=0,031$). Erkek cinsiyet ($p=0,0001$), evre III-IV ($p=0,0001$), T3-T4 ($p=0,021$), M1 evreleri ($p=0,0001$), multifokalite ($p=0,0001$) ve iki taraflı akciğer tutulumu oranı ($p=0,0001$) hayatta kalmayanlarda daha yüksekti.

Sonuç: BT görüntüleri LPA ve İMA'larda ayırıcı tanıya yararlı olsa da SUV_{maks} bu iki grubun ayırımında yardımcı olmadı. Ancak bu hastalarda hem ^{18}F -FDG tutulumu hem de BT bulguları prognozu öngörmede önemli rol oynayabilir.

Anahtar kelimeler: ^{18}F -FDG PET/BT, akciğerin primer invaziv münöz adenokarsinomu, lepidik predominant akciğer adenokarsinomu

Introduction

In 2011, a new classification of lung adenocarcinoma (ADC) was proposed in an international and multidisciplinary panel supported by the International Association for the Study of Lung Cancer (IASLC)/American Thoracic Society (ATS), and European Respiratory Society (ERS). The use of the terms "bronchioloalveolar carcinoma (BAC)" and "mixed subtype ADC" was discontinued based on the proposal of this panel. According to the extent of lepidic versus invasive growth patterns, BACs are reclassified into 5 subtypes: 1) Adenocarcinoma *in situ* (AIS), 2) minimally invasive adenocarcinoma (MIA), 3) lepidic predominant adenocarcinoma (LPA) 4) invasive mucinous adenocarcinoma (IMA), 5) ADC predominantly invasive with some nonmucinous lepidic components (1).

AIS and MIA have similar clinical and prognostic characteristics. The 5-year disease-free survival (DFS) rate is 100% for patients with AIS. Patients with MIA have nearly 100% DFS if the lesion is completely resected (2). LPA and IMA are more invasive than AIS and MIA. Additionally, IMAs exhibit different clinicopathological, radiological, and prognostic characteristics from those of non-mucinous ADCs (1,3). Although non-mucinous ADCs tend to be localized, IMAs are more likely to be multifocal, multilobar, and bilateral (1). The radiological appearance of these tumors is associated with prognosis. Localized ADC has a better prognosis after resection. As a radiolabeled glucose analog, ^{18}F -fluorodeoxyglucose (^{18}F -FDG) reflects glucose metabolism in tumor tissue. ^{18}F -FDG positron emission tomography/computed tomography (PET/CT) is an effective molecular imaging method for the diagnosis, staging, and monitoring of lung cancer. The standardized uptake value (SUV) is commonly used as a semiquantitative measure of ^{18}F -FDG uptake in tissues. In this retrospective study, we compared the ^{18}F -FDG PET/CT findings of LPAs with those of IMAs. Moreover, we investigated the differences between the ^{18}F -FDG PET/CT findings of survivors and non-survivor.

Materials and Methods

Patients

Patients with histologically confirmed LPA and MIA who underwent pretreatment with ^{18}F -FDG PET/CT between August 2008 and May 2019 were included in this retrospective study. The exclusion criteria were as follows: 1) Patients with another cancer; 2) prior chemoradiotherapy. Histological confirmation was performed via biopsy or surgical resection in all cases according to the 2011 IASLC/ATS/ERS and 2015 World Health Organization classification schemes. We collected data on age at diagnosis, sex, surgical approach, histopathological subtype, stage, treatment information, and ^{18}F -FDG PET/CT findings. Furthermore, follow-up data of patients were recorded. The 8th edition of the Tumor, Node, and Metastasis lung cancer staging system was used for the staging of all patients (4). Stages I and II were defined as early stages, while Stages III and IV were defined as advanced stages. This retrospective study was approved by University of Health Sciences Türkiye, Ankara Atatürk Pulmonary Diseases and Thoracic Surgery Training and Research Hospital Institutional Review Board (decision no.: 682, date: 16.07.2020).

^{18}F -FDG PET/CT Imaging

PET/CT scanning was performed from the vertex to the upper thigh using the Siemens Biograph 6 HI-REZ integrated PET/CT scanner (Siemens Medical Solutions, Knoxville, TN, USA). All patients fasted for at least 4-6 hours before PET/CT examination. After determining that the patients' blood glucose levels were <200 mg/dL, ^{18}F -FDG (5.18 MBq/kg) was injected intravenously. Approximately 45-60 minutes after ^{18}F -FDG injection, PET/CT scanning was performed. First, CT images were acquired with 130 kV, automatic, real-time dose modulation amperage. After CT, the PET scan was performed in 3D mode with 3 min per bed position for a total of 6-8 bed positions. CT was used for attenuation correction and anatomical localization of

the PET images. PET data were reconstructed using the ordered-subset expectation-maximization algorithm.

¹⁸F-FDG PET/CT Analysis

Reconstructed transaxial, coronal, and sagittal PET, CT, fused PET/CT, and maximum-intensity projection images of all patients were reviewed using a dedicated Workstation. Tumors were divided into 2 groups according to CT appearance: Group 1: nodular-type tumor; group 2: mass- or pneumonic-type tumor. The nodular type was defined as a rounded or oval lesion 3 cm in diameter. The mass type was defined as a focal lesion >3 cm in diameter. The pneumonic type was defined as a lesion manifesting as pneumonia-like consolidation (5,6). Unilateral and bilateral multifocal disease was detected. Multifocal cases were classified as unilateral multifocal and bilateral multifocal. Maximal CT diameter, tumor site, characteristics of nodules [ground-glass opacity (GGO), solid or subsolid nodules], and accompanying radiolucencies (air bronchogram, air alveologram, pseudocavitation, true cavitation) within the tumor were noted. GGO was defined as increased hazy attenuation of the lung without obscuration of the underlying bronchial and vascular margins. A subsolid nodule was defined as a nodule with both ground glass and solid components. For semiquantitative analysis of ¹⁸F-FDG uptake, a region of interest (ROI) was drawn over the tumors using PET images. The maximum SUV (SUV_{max}), which are the maximum pixel values within the defined ROIs, were calculated automatically on the workstation. The SUV_{max} values of the mediastinal and hilar lymph nodes were also recorded. ¹⁸F-FDG uptake by lymph nodes was greater than that by the mediastinal blood pool and was interpreted as PET/CT positive.

Statistical Analysis

Survival time was defined as the period between the time of diagnosis and the time of death or last visit. Patients were divided into the following 2 groups: survivors and non-survivor. The associations between the categorical variables were evaluated by chi-square analysis. The Kruskal-Wallis H test was used to compare the three groups. The Mann-Whitney U test was used to compare the two groups. A p-value of less than 0.05 was considered statistically significant. Statistical analyses were performed using the Statistical Package for Social Sciences version 21.0.

Results

Clinicopathological Characteristics

A total of 57 patients were included in this study. Among the 57 patients, 43 (75.4%) were diagnosed with IMA and 14 (24.6%) with LPA. Curative surgery was

performed in 48 patients (40 lobectomies, 3 bilobectomy, 1 pneumonectomy, 4 wedge resections). Percutaneous transthoracic needle aspiration biopsy was performed in 8 IMA cases and 1 LPA case. These 9 patients were not operated. Lymph node biopsy and/or dissection were performed in 44 (12 LPA, 32 IMA) cases.

Comparison of Clinicopathological Characteristics Between IMAs and LPAs

The clinicopathological characteristics of the patients are compared in Table 1. There were no significant differences in age ($p=0.861$) and sex ($p=0.701$) between the two groups. LPAs had lower T, M, and overall stage than in IMAs ($p=0.048$, $p=0.0449$ and $p=0.022$, respectively). The rate of receiving chemotherapy was higher among patients with IMA ($p=0.011$).

Comparison of ¹⁸F-FDG PET/CT Findings in IMAs and LPAs

Among the 43 IMAs, 25 (58.2%) were mass ($n=11$) or pneumonic types ($n=14$) on CT images. Nodular IMAs presented as subsolid in 12 cases, solid in 3 cases, and cavitary in 3 cases. LPAs were of nodular type (1 solid, 10 subsolids, and 1 pure GGO) in 12 patients and pneumonic type in 2 patients. No mass-type tumor was observed in LPA. IMAs were more likely to occur as mass/pneumonic type tumors than LPAs ($p=0.011$) (Table 2).

The incidence of unilateral or bilateral multifocal disease was higher in IMAs than in LPAs, although there was no significant difference ($p=0.478$). However, bilateral involvement was significantly higher in IMAs than LPAs ($p=0.049$). No bilateral tumor involvement was observed in LPAs at the time of diagnosis. There was no significant difference in the presence of intralesional radiolucencies between LPAs and IMAs ($p=1$). Overt cavitation was obtained in 6 cases with IMAs.

The size of LPAs was significantly smaller than that of IMAs ($p=0.003$). There was no statistically significant difference in SUV_{max} between IMAs and LPAs ($p=0.078$). The SUV was significantly lower in the nodular group than in the mass/pneumonic-type group (mean \pm standard deviation: 3.25 ± 2.34 versus 5.28 ± 2.78 , respectively, $p=0.0001$). There was no distinctive ¹⁸F-FDG uptake in patients with LPA and GGO. In all cases apart from this, there was ¹⁸F-FDG uptake that could be distinguished from parenchymal activity. The SUV_{max} ranged from 0.79 to 14.7 in all 57 patients. The SUV_{max} was less than 2.5 in 10/47 (21.2%) patients with IMA. Otherwise, 6 of 14 patients (42.8%) with LPA had an SUV_{max} of less than 2.5. There was a significant correlation between the size of tumors and the SUV_{max} values ($p=0.002$).

The mediastinal and hilar lymph node stations were evaluated histopathologically (Table 1). There were 24 lymph node stations were ¹⁸F-FDG-positive. The SUV_{max} values ranged from 2.6 to 5.2. Four of the 24 lymph node stations were positive on histopathological examination. Reactive lymphoid proliferation and/or anthracosis were detected in the remaining 20 ¹⁸F-FDG-positive lymph node stations. A metastatic intrapulmonary lymph node was found on histopathological examination. However, this lymph node was not detected on PET/CT scan. The overall sensitivity, specificity, accuracy, positive predictive value, and negative predictive value of PET/CT in the detection of lymph node metastasis were 80%, 91.2%, and 90.9%, 16.6%, and 99.5%, respectively. All lymph node

metastases were detected in 2 patients with IMA. PET/CT imaging revealed extrathoracic metastases in 2 cases with IMA. There were no pathological nodal involvement or extrathoracic metastases in LPAs.

Analyses of Differences Between Survivors and Non-survivors

The mean follow-up duration was 40.9 months (range: 1-102). There was no significant difference in the mean survival time between IMA and LPA (46.2 versus 36 months, respectively, p=0.075). At the end of this study, a total of 11/57 (19.2%) patients died, including 9 IMA and 2 LPA patients (Table 3). One patient with LPA died 4 months after diagnosis. This patient had not undergone surgery. Another patient with LPA who underwent curative lower lobectomy died 15 months after the surgery. The causes of death in these patients were not available in the medical records.

No significant differences were found between groups regarding gender (p=0.0001), age (p=0.105), histopathological subtype of the tumor (0.714), size of the lesion (p=0.135), and the presence of intralesional radiolucencies (p=0.219). There were no significant differences in the incidence of nodular-type tumors versus mass/pneumonic-type tumors (p=0.386) between groups. Male gender (p=0.0001), rate of stages T3-T4 (p=0.021), M1 disease (p=0.0001), stages III-IV (p=0.0001), multifocality (p=0.0001), bilateral involvement (p=0.0001), and level of SUV_{max} (p=0.031) were higher in the dead group.

Table 1. Clinicopathological characteristics between the groups

	Histopathological subtypes		p-value
	IMA (n=43)	LPA (n=14)	
Gender			
Males, n (%)	23 (53.5%)	6 (42.9%)	0.701
Female, n (%)	20 (46.5%)	8 (57.1%)	
Age, years (mean ± SD)	57.9±12.6	57.4±9.3	0.861
Chemotherapy present, n (%)	25 (41.9%)	2 (14.3%)	0.011
T classification, n (%)			
T1/T2	22 (51.2)	12 (85.7)	0.048
T3/T4	21 (48.8)	2 (14.3)	
Number of resected LNs stations	164	69	
Number of pathologically positive LNs	5	0	
N classification[‡], n (%)			
N0	30 (93.7)	12 (100)	
N1	1 (3.1)	0 (0)	
N2	1 (3.1)	0 (0)	
N3	0 (0)	0 (0)	
M classification, n (%)			
M0	32 (74.4)	14 (100)	0.049
M1	11 (25.6)	0 (0)	
Stage, n (%)			
I/II	25 (58.1)	13 (92.9)	0.022
III/IV	18 (41.9)	1 (7.1)	

IMA: Invasive mucinous lung adenocarcinoma, LPA: Lepidic predominant lung adenocarcinoma, SD: Standard deviation, LNs: Lymph nodes
[‡]Lymph node biopsy and/or dissection were performed in 44 (12 LPA, 32 IMA) cases. Lymph node metastases were found in only 2 patients

Table 2. Comparison of ¹⁸F-FDG PET/CT characteristics between groups

	Histopathological subtypes		p-value
	IMA	LPA	
SUV _{max} of all cases (mean ± SD)	4.48±2.75	3.40±2.61	0.078
Diameter of lesion (cm), mean ± SD	4.8±3.3	2.5±1.2	0.003
CT appearances			
Mass/pneumonic type, n (%)	25 (58.1)	2 (14.3)	0.011*
Nodular type, n (%)	18 (41.9)	12 (85.7)	
Multifocality, n (%)	12 (27.9)	2 (14.3)	0.478
Bilateral multifocality, n (%)	11 (25.6)	0 (0)	0.049
Presence of intralesional radiolucency, n (%)	34 (79.1)	11 (78.6)	1

IMA: Invasive mucinous lung adenocarcinoma, LPA: Lepidic predominant lung adenocarcinoma, ¹⁸F-FDG: F-18 fluorodeoxyglucose, PET/CT: Positron emission tomography/computed tomography, SUV_{max}: Maximum standardized uptake value, SD: Standard deviation, *The mass/pneumonic-type was significantly more common in IMAs

Discussion

When we compared the CT features between LPAs and IMAs, we found that pneumonic/mass-type tumors were more associated with IMAs in our study. Patients with IMA had a higher incidence of multifocal involvement (Figure 1). These findings are consistent with those of previous studies (1,7). Tumor cells tend to spread through air spaces in IMAs. This pattern of invasion may lead to a pneumonia-like pattern

and increased rates of intrapulmonary metastasis in these patients (8). LPAs are more likely to manifest as pure GGO or subsolid nodules (1). A majority of LPAs manifested as subsolid nodules in our study. We did not find any mass-type tumors in the LPAs. Two LPA cases were pneumonic. Only one LPA exhibited a pure GGO appearance with a diameter of 3 cm. There was no ^{18}F -FDG uptake in this lesion (Figure 2). The GGO component of lung ADCs generally corresponds with lepidic tumor growth. The spreading of malignant cells along the alveolar walls and septa without destruction in the parenchyma is referred to as a lepidic growth pattern. There is no invasion into the stroma, blood vessels, or pleura of this growth type (9). The solid component within GGO lesions is correlated with invasive tumor growth, fibrosis, and alveolar collapse (10). Pure GGO tumors are usually ^{18}F -FDG-negative, slow-growing, and well-differentiated tumors (11). In addition,

Table 3. Analyses of differences between survivors and non-survivors			
	Survivors (n=46)	Non-survivors (n=11)	p-value
Gender			
Male, n (%)	18 (62.1)	11 (37.9)	0.0001
Female, n (%)	28 (100)	0 (0)	
Age (years), mean \pm SD	56.6 \pm 11.3	62.7 \pm 13.1	0.105
Histopathological subtype			
LPA, n (%)	12 (85.7)	2 (14.3)	0.714
IMA, n (%)	34 (79.1)	9 (20.9)	
T classification			
I/II	31 (91.2)	3 (8.8)	0.021
II/IV	15 (65.2)	8 (34.8)	
M classification			
M0	43 (93.5)	3 (6.5)	0.0001
M1	3 (27.3)	8 (72.7)	
Overall stage			
I/II	36 (94.7)	2 (5.3)	0.0001
III/IV	10 (52.6)	9 (47.4)	
Tumor size (cm), mean \pm SD	4.1 \pm 3.1	4.9 \pm 2.8	0.135
SUV _{max} of tumor, mean \pm SD	3.66 \pm 2	6.52 \pm 4.08	0.031
Multiple lung involvement			
Present	6 (42.9)	8 (57.1)	0.0001
Absent	40 (93)	3 (7)	
Bilateral lung involvement			
Present	3 (27.3)	8 (72.7)	0.0001
Absent	43 (93.5)	3 (6.5)	
CT presentation			
Nodular type	26 (86.7)	4 (33.3)	0.386
Mass/pneumonic type	20 (74.1)	7 (25.9)	
Intralesional air			
Present	38 (84.4)	4 (19.3)	0.219
Absent	8 (66.7)	11 (33.3)	

SD: Standard deviation, IMA: Invasive mucinous lung adenocarcinoma, LPA: Lepidic predominant lung adenocarcinoma, SUV_{max}: Maximum standardized uptake value, CT: Computed tomography

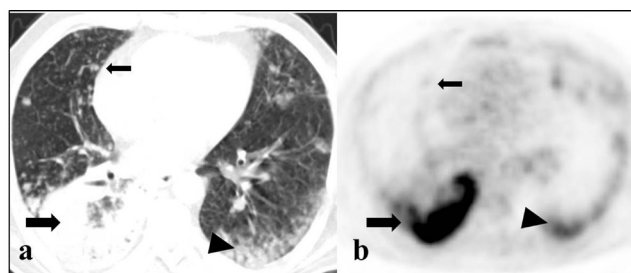


Figure 1. Axial ^{18}F -FDG PET/CT images of a 52-year-old male with bilateral IMA. a) CT image (lung window) showing pneumonic-type IMA on the right lower lobe (thick arrow), bilateral parenchymal infiltrates (arrowhead), and multiple small nodules (thin arrow). b) PET image demonstrating intense ^{18}F -FDG uptake in the pneumonic-type IMA. Mild-to-moderate ^{18}F -FDG uptake is observed in the bilateral parenchymal infiltrates and nodules (arrows)
 ^{18}F -FDG: F-18 fluorodeoxyglucose, PET/CT: Positron emission tomography/computed tomography, IMA: Invasive mucinous lung adenocarcinoma

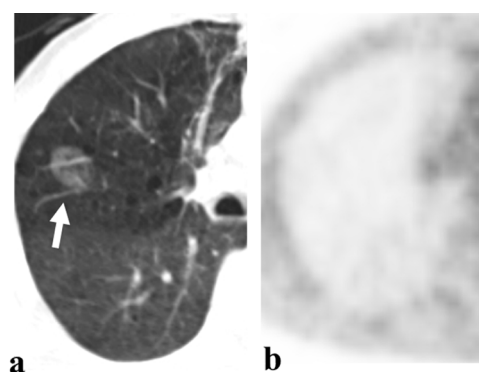


Figure 2. Axial ^{18}F -FDG PET/CT images of a 54-year-old male with LPA. a) CT image (lung window) showing a 30-mm-sized pure ground glass nodule in the right lung (arrow). b) There is no ^{18}F -FDG uptake in the nodule
 ^{18}F -FDG: F-18 fluorodeoxyglucose, PET/CT: Positron emission tomography/computed tomography, LPA: Lepidic predominant lung adenocarcinoma

the incidence of nodal and distant metastasis was low in these tumors. PET/CT imaging is not recommended for the diagnostic evaluation and staging of GGOs (12).

It has been reported that intralesional radiolucencies (air bronchogram, air alveologram, pseudocavitation, true cavitation) are characteristic findings of BACs (13). There was no significant difference in the presence of intralesional air between IMAs and LPAs in our study (Figure 3). It has been reported that cavity formation occurs in 5.6-13.9% of IMAs (14,15). We found overt cavitation in 6 of 47 patients with IMA (12.7%). Three of the cases were multifocal (Figure 4).

Variable ^{18}F -FDG uptake was observed in all 57 cases, ranging from 0.79 to 14.7. The predominant histologic subtype is associated with ^{18}F -FDG uptake. Several studies reported that AIS, MIA, LPA, and IMA had low SUV_{max} values, whereas acinar, papillary, micropapillary, and solid predominant ADCs had high SUV_{max} values (16). Consistent with these studies, the mean SUV_{max} was low in IMAs and LPAs in our study (mean SUV_{max} 4.4 and 3.4, respectively). However, no statistically significant difference was found in SUV_{max} between IMAs and LPAs ($p=0.078$). LPAs refer to the proliferation of type II pneumocyte or Clara cells. IMAs typically comprise neoplastic goblet or tall columnar cells with abundant intracytoplasmic mucin (17,18). Tumors that were formerly called BAC have a small number of active malignant cells (9). The ^{18}F -FDG uptake intensity is associated with the number of malignant cells in the tumor.

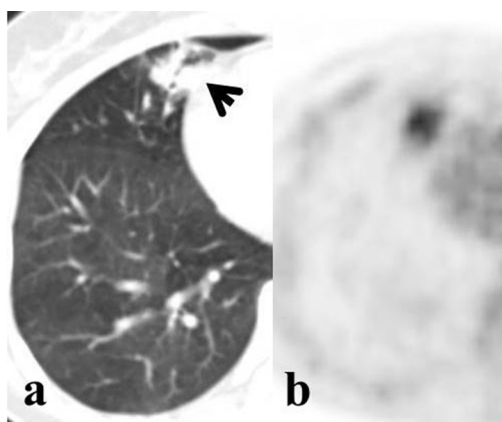


Figure 3. Axial ^{18}F -FDG PET/CT images of a 47-year-old female patient with a solitary LPA. a) CT image (lung window) showing a 25-mm-sized lobulated and spiculated nodule containing internal air densities in the right lung (arrow). b) PET image demonstrating ^{18}F -FDG uptake in the nodule with an SUV_{max} of 2.29

^{18}F -FDG: F-18 fluorodeoxyglucose, PET/CT: Positron emission tomography/computed tomography, LPA: Lepidic predominant lung adenocarcinoma, SUV_{max} : Maximum standardized uptake value

It is known that tumor size is correlated with ^{18}F -FDG uptake (19). Consistent with the literature, we found a positive and significant correlation between SUV_{max} and tumor size ($p=0.002$). The size of LPAs was significantly smaller than that of IMAs ($p=0.003$). Additionally, the SUV_{max} was significantly lower in the nodular group than in the mass/pneumonic-type group ($p=0.0001$). Lee et al. (20) found that consolidative patterns exhibited higher SUV_{max} than nodular patterns in IMAs.

The risk of lymph node involvement is associated with lung ADC subtypes. The incidence of regional nodal involvement was low for LPAs and IMAs (21,22). Yu et al. (21) investigated lymph node involvement in lung ADC with a tumor size ≤ 3 cm. They found that the percentages of lymph node involvement were: 47.6%, 47.2%, 24.0%, 18.9%, 18.1%, 0%, 0%, and 0% for solid predominant, micropapillary predominant, variants of invasive ADC, papillary predominant, acinar predominant, lepidic predominant, MIA, and AIS, respectively (21). The diameter of the tumor was 6 cm in a patient with LPA in our study. No lymph node was involved in this patient. The diameter of primary tumors was ≤ 3 cm in all other LPAs. In addition, we found lymph node involvement in 2 of 32 patients (6.25%) who underwent lymph node biopsy and/or dissection. Beck et al. (22) reported lymph node involvement in 7 of 46 patients (15.2%) with IMA. The overall sensitivity and specificity of PET/CT for the detection of lymph node involvement were 80% and 91.23%, respectively, in our study.

The prognosis of IMA is controversial. Several previous studies have demonstrated that mucinous ADCs are associated with poor survival (23,24). Kirsten rat sarcoma viral oncogene homolog (KRAS) mutation is detected in 28-87% of IMAs. The frequency of epidermal growth factor

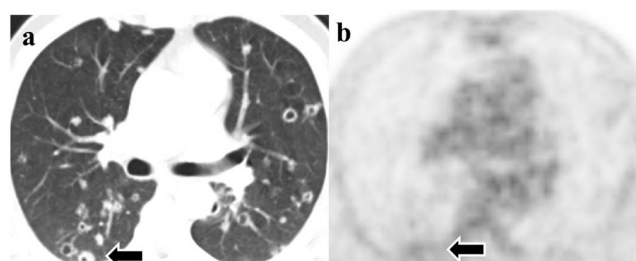


Figure 4. Axial ^{18}F -FDG PET/CT images of a 57-year-old female patient with IMA presenting as multiple cavitary lesions. a) CT image (lung window) showing multiple bilateral small cavitary nodules (arrow). b) PET image demonstrating mild ^{18}F -FDG uptake in the nodules (arrow)
 ^{18}F -FDG: F-18 fluorodeoxyglucose, PET/CT: Positron emission tomography/computed tomography, IMA: Invasive mucinous lung adenocarcinoma

receptor (EGFR) mutations in IMAs is 5% (25). LPAs, AIS, and MIAs are positively associated with EGFR mutations (26). Patients with EGFR mutation-positive tumors are sensitive to EGFR tyrosine kinase inhibitors. These agents are associated with significantly prolonged progression-free survival compared with standard chemotherapy (27). However, some recent studies have indicated that IMAs have a better prognosis than most ADCs (28,29). Cai et al. (29) indicated that there were no differences in overall survival (OS) between patients with IMAs and those with mucus-negative ADCs (OS: 49.5 months versus 63.5 months, $p=0.524$). Lee et al. (20) showed no significant difference in 5-year OS between IMAs, intermediate (acinar/papillary predominant) non-mucinous ADCs, and high-grade (micropapillary/solid predominant) non-mucinous ADCs. They found that patients with LPA (low-grade non-mucinous ADCs) had significantly better OS and DFS than those with other subtypes. Lee et al. (20) reported that the median survival of patients with IMAs was 47.8 months. Similarly, the median survival time was 46.2 months in patients with IMA. Although statistically insignificant, we found that the median survival time of patients with IMA was shorter than that of patients with LPA (69.3 months).

During follow-up, 11 (9 IMA and 2 LPA) patients died in our study. Male sex, rate of stage III-IV, T3-T4, M1 diseases, multifocality, and bilateral involvement were higher in the non-survivors group in our analyses. Previous studies reported that multifocal nodular tumors were associated with poor OS rates in IMAs (20). M1 disease was associated with multifocal lung involvement in our series. The incidence of extrathoracic metastases was low in both LPAs and IMAs (30,31). Consistent with previous reports, extrathoracic metastases were detected in only 2 patients with IMA in our study.

We found no significant difference between the nodular and mass/pneumonic forms in survivors and non-survivors. However, Lee et al. (20) demonstrated that IMAs with consolidative patterns had relatively poorer OS compared with nodular patterns. The differences were not statistically significant. Epstein (32) reported that the consolidative form has a poorer prognosis than the localized nodular form in patients with BAC. We found significantly higher T stages in IMAs than in LPAs ($p=0.048$). Tumors with a consolidative form tend to be large and occur in the advanced T stage.

There was no association between the presence of intralesional air and poor prognosis in our study. However, Yoshino et al. (33) demonstrated that air bronchogram was a good independent prognostic factor for stage I lung ADC. It has been reported that intralesional radiolucency

corresponds to patent intratumoral bronchioles (14). However, contrary to these results, Zhang et al. (34) showed that the number of air bronchogram progressively increased from preinvasive atypical adenomatous hyperplasia (5.3%) and AIS (17.7%) to invasive MIA (30.5%) and IAC (54.1%). They also demonstrated the relationship between air bronchogram patterns and lung ADC invasiveness. As invasiveness increased, the dilated or tortuous bronchus lumen and obstructed bronchus were observed more frequently in their study. They suggested that tumor cell infiltration of bronchioles leads to airway tortuosity, ectasis, and obstruction.

The SUV_{max} was higher in the death group than in the survival group ($p=0.031$) in our study. Lee et al. (20) found that SUV_{max} was a significant independent poor prognostic predictor for DFS but not OS in patients with IMA. They reported that patients with SUV_{max} below 4.4 and those with an SUV_{max} of 4.4 or higher were associated with significantly different rates of DFS.

Study Limitations

Our analysis has some limitations. First, this is a single-institution study. In addition, IMAs are rare tumors, accounting for approximately 5% of all lung ADCs (35). First, the number of patients was low. Second, this was a retrospective study. Further larger prospective studies are needed to validate these results.

Conclusion

CT has an important role in the differential diagnosis of IMAs and LPAs. Multifocal lung involvement and mass/pneumonic type presentation are related to IMAs. However, SUV_{max} was not a determinative factor in the differential diagnosis between the two groups. SUV_{max} may be an important factor affecting the prognosis of IMAs and LPAs.

Ethics

Ethics Committee Approval: The study was approved by University of Health Sciences Türkiye, Ankara Atatürk Pulmonary Diseases and Thoracic Surgery Training and Research Hospital Institutional Review Board (decision no.: 682, date: 16.07.2020).

Informed Consent: Retrospective study.

Authorship Contributions

Surgical and Medical Practices: E.T., F.D., D.K., S.B., Design: Ö.Ö., Data Collection or Processing: D.K., Analysis or Interpretation: E.T., Writing: E.T.

Conflict of Interest: No conflict of interest was declared by the authors.

Financial Disclosure: The authors declared that this study has received no financial support.

References

- Travis WD, Brambilla E, Noguchi M, Nicholson AG, Geisinger KR, Yatabe Y, Beer DG, Powell CA, Riely GJ, Van Schil PE, Garg K, Austin JH, Asamura H, Rusch VW, Hirsch FR, Scagliotti G, Mitsudomi T, Huber RM, Ishikawa Y, Jett J, Sanchez-Cespedes M, Sculier JP, Takahashi T, Tsuboi M, Vansteenkiste J, Wistuba I, Yang PC, Aberle D, Brambilla C, Flieder D, Franklin W, Gazdar A, Gould M, Hasleton P, Henderson D, Johnson B, Johnson D, Kerr K, Kuriyama K, Lee JS, Miller VA, Petersen I, Roggli V, Rosell R, Saijo N, Thunnissen E, Tsao M, Yankelewitz D. International association for the study of lung cancer/american thoracic society/european respiratory society international multidisciplinary classification of lung adenocarcinoma. *J Thorac Oncol.* 2011;6:244-285.
- Kadota K, Villena-Vargas J, Yoshizawa A, Motoi N, Sima CS, Riely GJ, Rusch VW, Adusumilli PS, Travis WD. Prognostic significance of adenocarcinoma in situ, minimally invasive adenocarcinoma, and nonmucinous lepidic predominant invasive adenocarcinoma of the lung in patients with stage I disease. *Am J Surg Pathol.* 2014;38:448-460.
- Kuhn E, Morbini P, Cancellieri A, Damiani S, Cavazza A, Comin CE. Adenocarcinoma classification: patterns and prognosis. *Pathologica.* 2018;110:5-11.
- Van Schil PE, Rami-Porta R, Asamura H. The 8th TNM edition for lung cancer: a critical analysis. *Ann Transl Med.* 2018;6:87.
- Choromańska A, Macura KJ. Evaluation of solitary pulmonary nodule detected during computed tomography examination. *Pol J Radiol.* 2012;77:22-34.
- Detterbeck FC, Franklin WA, Nicholson AG, Girard N, Arenberg DA, Travis WD, Mazzone PJ, Marom EM, Donington JS, Tanoue LT, Rusch VW, Asamura H, Rami-Porta R; IASLC Staging and Prognostic Factors Committee; Advisory Boards; Multiple Pulmonary Sites Workgroup. The IASLC Lung Cancer Staging Project: Background Data and Proposed Criteria to Distinguish Separate Primary Lung Cancers from Metastatic Foci in Patients with Two Lung Tumors in the Forthcoming Eighth Edition of the TNM Classification for Lung Cancer. *J Thorac Oncol.* 2016;11:651-665.
- Cha YJ, Kim HR, Lee HJ, Cho BC, Shim HS. Clinical course of stage IV invasive mucinous adenocarcinoma of the lung. *Lung Cancer.* 2016;102:82-88.
- Austin JH, Garg K, Aberle D, Yankelevitz D, Kuriyama K, Lee HJ, Brambilla E, Travis WD. Radiologic implications of the 2011 classification of adenocarcinoma of the lung. *Radiology.* 2013;266:62-71.
- Thompson WH. Bronchioloalveolar carcinoma masquerading as pneumonia. *Respir Care.* 2004;49:1349-1353.
- Moon Y, Sung SW, Lee KY, Park JK. Clinicopathological characteristics and prognosis of non-lepidic invasive adenocarcinoma presenting as ground glass opacity nodule. *J Thorac Dis.* 2016;8:2562-2570.
- Brandão DS, Haddad R, Marsico GA, Boasquevisque CH. Aspectos clínico-patológicos do carcinoma bronquioloalveolar e sobrevida em pacientes no estágio clínico I [Clinicopathological aspects of and survival in patients with clinical stage I bronchioloalveolar carcinoma]. *J Bras Pneumol.* 2010;36:167-174.
- Kim TJ, Park CM, Goo JM, Lee KW. Is there a role for FDG PET in the management of lung cancer manifesting predominantly as ground-glass opacity? *AJR Am J Roentgenol.* 2012;198:83-88.
- Gaeta M, Caruso R, Blandino A, Bartiromo G, Scribano E, Pandolfo I. Radiolucencies and cavitation in bronchioloalveolar carcinoma: CT-pathologic correlation. *Eur Radiol.* 1999;9:55-59.
- Watanabe Y, Kusumoto M, Yoshida A, Suzuki K, Asamura H, Tsuta K. Surgically resected solitary cavitary lung adenocarcinoma: association between clinical, pathologic, and radiologic findings and prognosis. *Ann Thorac Surg.* 2015;99:968-974.
- Wang T, Yang Y, Liu X, Deng J, Wu J, Hou L, Wu C, She Y, Sun X, Xie D, Chen C. Primary Invasive Mucinous Adenocarcinoma of the Lung: Prognostic Value of CT Imaging Features Combined with Clinical Factors. *Korean J Radiol.* 2021;22:652-662.
- Suárez-Piñera M, Belda-Sanchis J, Taus A, Sánchez-Font A, Mestre-Fusco A, Jiménez M, Pijuan L. FDG PET-CT SUVmax and IASLC/ATS/ERS histologic classification: a new profile of lung adenocarcinoma with prognostic value. *Am J Nucl Med Mol Imaging.* 2018;8:100-109.
- Oka S, Hanagiri T, Uramoto H, Baba T, Takenaka M, Yasuda M, Ono K, So T, Takenoyama M, Yasumoto K. Surgical resection for patients with mucinous bronchioloalveolar carcinoma. *Asian J Surg.* 2010;33:89-93.
- Goudarzi B, Jacene HA, Wahl RL. Diagnosis and differentiation of bronchioloalveolar carcinoma from adenocarcinoma with bronchioloalveolar components with metabolic and anatomic characteristics using PET/CT. *J Nucl Med.* 2008;49:1585-1592.
- Ozgül MA, Kirkil G, Seyhan EC, Cetinkaya E, Ozgül G, Yüksel M. The maximum standardized FDG uptake on PET-CT in patients with non-small cell lung cancer. *Multidiscip Respir Med.* 2013;8:69.
- Lee HY, Cha MJ, Lee KS, Lee HY, Kwon OJ, Choi JY, Kim HK, Choi YS, Kim J, Shim YM. Prognosis in Resected Invasive Mucinous Adenocarcinomas of the Lung: Related Factors and Comparison with Resected Nonmucinous Adenocarcinomas. *J Thorac Oncol.* 2016;11:1064-1073.
- Yu Y, Jian H, Shen L, Zhu L, Lu S. Lymph node involvement influenced by lung adenocarcinoma subtypes in tumor size ≤ 3 cm disease: A study of 2268 cases. *Eur J Surg Oncol.* 2016;42:1714-1719.
- Beck KS, Sung YE, Lee KY, Han DH. Invasive mucinous adenocarcinoma of the lung: Serial CT findings, clinical features, and treatment and survival outcomes. *Thorac Cancer.* 2020;11:3463-3472.
- Yoshizawa A, Motoi N, Riely GJ, Sima CS, Gerald WL, Kris MG, Park BJ, Rusch VW, Travis WD. Impact of proposed IASLC/ATS/ERS classification of lung adenocarcinoma: prognostic subgroups and implications for further revision of staging based on analysis of 514 stage I cases. *Mod Pathol.* 2011;24:653-664.
- Russell PA, Wainer Z, Wright GM, Daniels M, Conron M, Williams RA. Does lung adenocarcinoma subtype predict patient survival?: A clinicopathologic study based on the new International Association for the Study of Lung Cancer/American Thoracic Society/European Respiratory Society international multidisciplinary lung adenocarcinoma classification. *J Thorac Oncol.* 2011;6:1496-1504.
- Nakagomi T, Goto T, Hirotsu Y, Shikata D, Yokoyama Y, Higuchi R, Otake S, Amemiya K, Oyama T, Mochizuki H, Omata M. Genomic Characteristics of Invasive Mucinous Adenocarcinomas of the Lung and Potential Therapeutic Targets of B7-H3. *Cancers (Basel).* 2018;10:478.
- Tsuta K, Kawago M, Inoue E, Yoshida A, Takahashi F, Sakurai H, Watanabe SI, Takeuchi M, Furuta K, Asamura H, Tsuda H. The utility of the proposed IASLC/ATS/ERS lung adenocarcinoma subtypes for disease prognosis and correlation of driver gene alterations. *Lung Cancer.* 2013;81:371-376.
- Zhou C, Wu YL, Chen G, Feng J, Liu XQ, Wang C, Zhang S, Wang J, Zhou S, Ren S, Lu S, Zhang L, Hu C, Hu C, Luo Y, Chen L, Ye M, Huang J, Zhi X, Zhang Y, Xiu Q, Ma J, Zhang L, You C. Erlotinib versus chemotherapy as first-line treatment for patients with advanced EGFR mutation-positive non-small-cell lung cancer (OPTIMAL, CTONG-0802): a multicentre, open-label, randomised, phase 3 study. *Lancet Oncol.* 2011;12:735-742.
- Yoshizawa A, Sumiyoshi S, Sonobe M, Kobayashi M, Fujimoto M, Kawakami F, Tsuruyama T, Travis WD, Date H, Haga H. Validation of the IASLC/ATS/ERS lung adenocarcinoma classification for prognosis and association with EGFR and KRAS gene mutations: analysis of 440 Japanese patients. *J Thorac Oncol.* 2013;8:52-61.
- Cai D, Li H, Wang R, Li Y, Pan Y, Hu H, Zhang Y, Gong R, Pan B, Sun Y, Chen H. Comparison of clinical features, molecular alterations, and prognosis in morphological subgroups of lung invasive mucinous adenocarcinoma. *Onco Targets Ther.* 2014;7:2127-2132.

30. Araki K, Kidokoro Y, Hosoya K, Wakahara M, Matsuoka Y, Takagi Y, Haruki T, Miwa K, Taniguchi Y, Horie S, Nakamura H. Excellent prognosis of lepidic-predominant lung adenocarcinoma: low incidence of lymphatic vessel invasion as a key factor. *Anticancer Res.* 2014;34:3153-3156.
31. Breathnach OS, Kwiatkowski DJ, Finkelstein DM, Godleski J, Sugarbaker DJ, Johnson BE, Mentzer S. Bronchioloalveolar carcinoma of the lung: recurrences and survival in patients with stage I disease. *J Thorac Cardiovasc Surg.* 2001;121:42-47.
32. Epstein DM. Bronchioloalveolar carcinoma. *Semin Roentgenol.* 1990;25:105-111.
33. Yoshino I, Nakanishi R, Kodate M, Osaki T, Hanagiri T, Takenoyama M, Yamashita T, Imoto H, Taga S, Yasumoto K. Pleural retraction and intratumoral air-bronchogram as prognostic factors for stage I pulmonary adenocarcinoma following complete resection. *Int Surg.* 2000;85:105-112.
34. Zhang Y, Qiang JW, Shen Y, Ye JD, Zhang J, Zhu L. Using air bronchograms on multi-detector CT to predict the invasiveness of small lung adenocarcinoma. *Eur J Radiol.* 2016;85:571-577.
35. Park S, Lee SM, Noh HN, Hwang HJ, Kim S, Do KH, Seo JB. Differentiation of predominant subtypes of lung adenocarcinoma using a quantitative radiomics approach on CT. *Eur Radiol.* 2020;30:4883-4892.



Assessment of Y-90 Radioembolization Treatment Response for Hepatocellular Carcinoma Cases Using MRI Radiomics

MRG Radiomics Kullanılarak Hepatosellüler Karsinom Olgularında Y-90 Radyoembolizasyon Tedavisine Yanıtın Değerlendirilmesi

✉ Mennaallah Mahmoud¹, ✉ Ko-Han Lin², ✉ Rheun-Chuan Lee¹, ✉ Chien-an Liu¹

¹Taipei Veterans General Hospital, Clinic of Radiology, Taipei, Taiwan

²Taipei Veterans General Hospital, Clinic of Nuclear Medicine, Taipei, Taiwan

Abstract

Objectives: This study aimed to investigate the ability of radiomics features extracted from magnetic resonance imaging (MRI) images to differentiate between responders and non-responders for hepatocellular carcinoma (HCC) cases who received Y-90 transarterial radioembolization treatment.

Methods: Thirty-six cases of HCC who underwent MRI scans after Y-90 radioembolization were included in this study. Tumors were segmented from MRI T2 images, and then 87 radiomic features were extracted through the LIFEx package software. Treatment response was determined 9 months after treatment through the modified response evaluation criteria in solid tumours (mRECIST).

Results: According to mRECIST, 28 cases were responders and 8 cases were non-responders. Two radiomics features, "Grey Level Size Zone Matrix (GLSZM)-Small Zone Emphasis" and "GLSZM-Normalized Zone Size Non-Uniformity", were the radiomics features that could predict treatment response with the area under curve (AUC)= 0.71, sensitivity= 0.93, and specificity= 0.62 for both features. Whereas the other 4 features (kurtosis, intensity histogram root mean square, neighbourhood gray-tone difference matrix strength, and GLSZM normalized grey level non-uniformity) have a relatively lower but acceptable discrimination ability range from AUC= 0.6 to 0.66.

Conclusion: MRI radiomics analysis could be used to assess the treatment response for HCC cases treated with Y-90 radioembolization.

Keywords: MRI, radiomics, Y-90 radioembolization

Öz

Amaç: Bu çalışma, Y-90 transarteriyel radyoembolizasyon tedavisi gören hepatosellüler karsinomlu (HCC) olgularda manyetik rezonans görüntüleme (MRG) ile elde edilen görüntülerden çıkarılan radiomics özelliklerinin tedaviye yanıt verenler ile yanıt vermeyenler arasında ayırım yapma yeteneğini araştırmayı amaçlamaktadır.

Yöntem: Y-90 radyoembolizasyonundan sonra MRG taramaları yapılan 36 HCC olgusu bu çalışmaya dahil edildi. Tümörler MRG T2 görüntülerinden segmentlere ayrıldı ve ardından LIFEx paket yazılımı aracılığıyla 87 radiomics özelliği çıkarıldı. Tedavi yanıtı, tedaviden 9 ay sonra solid tümörlerde yanıt değerlendirme kriterleri (mRECIST) ile belirlendi.

Bulgular: mRECIST'e göre 28 olgu yanıt veren ve 8 olgu yanıt vermeyen olgulardı. İki radiomics özelliği "Gri seviye boyut bölgesi matrisi (GLSZM)-küçük bölge vurgusu" ve "GLSZM-normalize bölge boyutunun tekdüze olmaması", her iki özellik için de eğri altındaki alan (AUC)= 0,71 ve duyarlılık= 0,93 ve özgüllük= 0,62 ile tedavi yanıtını tahmin edebilen radiomics özellikleriydi. Diğer 4 özellik (kurtosis, yoğunluk histogramı ortalama karekökü, komşuluk gri ton farklılık matrisi gücü, GLSZM normalize gri seviye tekdüze olmaması) ise nispeten düşük ancak kabul edilebilir bir ayırım yeteneği aralığına sahiptir ve AUC= 0,6 ile 0,66 arasındadır.

Sonuç: MRG radiomics analizi, Y90 radyoembolizasyonu ile tedavi edilen HCC vakalarında tedavi yanıtını değerlendirmek için kullanılabilir.

Anahtar kelimeler: MRG, radiomics, Y-90 radyoembolizasyonu

Address for Correspondence: Ko-Han Lin MD, Taipei Veterans General Hospital, Clinic of Nuclear Medicine, Taipei, Taiwan

Phone: +0228712121 **E-mail:** khlin1979@gmail.com ORCID ID: orcid.org/0000-0002-1464-3483

Received: 19.10.2023 **Accepted:** 04.08.2024 **Epub:** 03.10.2024



Copyright© 2024 The Author. Published by Galenos Publishing House on behalf of the Turkish Society of Nuclear Medicine. This is an open access article under the Creative Commons Attribution-NonCommercial-NoDerivatives 4.0 (CC BY-NC-ND) International License.

Introduction

Hepatocellular carcinoma (HCC) stands as a significant contributor to cancer-related mortality worldwide, particularly prevalent in Asia and Africa (1). Yttrium-90 (Y-90) radioembolization emerges as a potent therapeutic modality for unresectable HCC, enabling precise delivery of high-dose of beta-radiation to the tumor while sparing adjacent healthy tissue (2). However, response to Y-90 radioembolization exhibits variability across patients, underscoring the importance of accurate response assessment in gauging treatment efficacy and guiding subsequent clinical decisions (3). Current response assessment criteria, such as modified response evaluation criteria in solid tumors (mRECIST), rely primarily on changes in tumor size, often falling short of capturing the nuanced treatment (4).

Radiomics, an advancing domain within medical imaging, presents a promising avenue for extracting quantitative features from medical images, potentially enhancing treatment response assessment. Moreover, radiomics delves into subtle nuances in image texture, shape, and intensity, imperceptible to the naked eye, yet likely correlated with tumor biology and treatment response (5). Notably, magnetic resonance imaging (MRI) radiomics has featured prominently in various studies predicting treatment responses in HCC patients. While some researchers have explored the utility of MRI-derived radiomics features in prognosticating response to transarterial chemoembolization (TACE) (6-10), few have examined their role in assessing response to transarterial radioembolization employing Y-90 in HCC patients (11,12). The aim of this current study is to investigate the efficacy of radiomic features extracted from MRI images in discriminating between responders and non-responder to Y-90 radioembolization in HCC patients.

Materials and Methods

Patients

A cohort of 36 patients with HCC (6 females and 30 males) were included in this study. Patients aged from (37 to 87) years with average age of 67.43 years. The patients' characteristics were shown in Figure 1. This study protocol was reviewed and approved by the Ethics Committee of Taipei Veterans General Hospital (IRB no: 2020-04-013BC, date: 13.04.2020). Informed consent was obtained from all subjects during inclusion in the study. Informed consent was obtained from all individual participants included in the study.

Imaging techniques

Planning Angiography and Technetium- 99m Macroaggregated Albumin (Tc-MAA) Single Photon Emission Computed Tomography (SPECT)/(CT)

All patients underwent a diagnostic angiogram and administration of 185 MBq (5 mCi) of Tc-MAA, followed by planar and SPECT/CT acquisitions on a hybrid SPECT/CT scanner (GE Discovery NM/CT670, USA) within one hour after Tc-MAA injection. Tc-MAA images were reconstructed on a GE Xeleris 3 workstation. The prescribed activity of the Y-90 microsphere was determined by medical internal radiation dosimetry (MIRD) model to reach a 120 Gy average dose in the target region for the glass microspheres and by partition model to reach tumor dose of 120 Gy.

Y-90 Radioembolization and Y-90 PET/MRI

All Y-90 treatments were done within 10 days after planning angiography using Y-90 glass microspheres (TheraSphere®; Boston Scientific Corp.) or Y-90 resin microspheres (SIR-Spheres®; Sirtex Medical Ltd.). After treatment, the post-Y90 internal pair production PET was obtained on a GE hybrid SIGNA PET/MRI with a maximum of two bed positions and 20-min acquisition per bed. MRI-T2 sequence was performed with 2D method, slice sequence= 6 mm, repetition time= 10000 msec, echo time= 106.88 msec, fat saturation= 3. All these scans and treatments occurred at our hospital between March 2018 and December 2021.

Radiomics Features

Images loaded to LIFEx Package versions 7.3.0 www.lifexsoft.org (13). Then images were segmented through three-dimensional semiautomatic tools in the package, and then 87 radiomic features were extracted, including

Characteristics of Patients	
Gender	M : F = 30 : 6
Age	37 – 87 years (mean: 67.43)
Lung shunt fraction (%)	2.4 – 20.6 (mead ± SD: 7.0 ± 4.3)
Treatment characteristics	
Glass (n=19)	1.1 – 7.3 GBq (mead ± SD: 3.1 ± 1.5)
Resin (n=17)	0.5 – 3.9 GBq (mead ± SD: 1.8 ± 1.2)
Bi-lobar treatment	28
Lobar treatment	4
Segmental treatment	4
Clinical features	
Child-Pugh score	A5 (n=30); A6 (n=6)
BCLC stage	B (n=26); C (n=10)
Alpha-fetoprotein	1.74 – 377340 ng/mL (median: 811)

Figure 1. Summary of patient characteristics that were included in this study

31 histogram features, 24 grey-level co-occurrence matrix Grey Level Cooccurrence Matrix (GLCM) features, 11 neighbourhood grey-level different matrix (GLRLM) features, 5 features grey-level run length matrix neighbourhood gray-tone difference matrix (NGTDM) features, and 16 Grey Level Size Zone Matrix (GLSZM) features. Figure 2 shows examples of HCC cases before and after segmentation.

Objective Response Rate (ORR)

The localized tumour response was defined as the response or progression within the radioembolization-treated liver. The response was evaluated using the mRECIST for HCC (14). Based on the best response of tumours observed on contrast-enhanced MRI or CT within 9 months after radioembolization. The ORR was defined as the sum of the complete response and the partial response. Eight cases were non-responders, while 28 cases were responders to treatment.

Statistical Analysis

The study used the Mann-Whitney U test to compare the responder and non-responder groups. The area under the curve from the receiver operating characteristic (ROC) was used to determine which features are sensitive to differentiating between responders and non-responders. The significance value for the tests was set at 0.05. All statistical tests were performed using Government of National Unity Public Social Private Partnership version 1.6.0.

Results

According to the Mann-Whitney U test, the only features with a significant difference between responders

and non-responders had a significance value of 0.02 (Table 1), whereas most of the features had a significance value higher than 0.05, indicating that there was no significant difference between the two groups, as shown in Table 2. The area under curve (AUC) was significant for two features, "GLSZM-Small Zone Emphasis" and "GLSZM-Normalized Zone Size Non-Uniformity", with an AUC of 0.71, and sensitivity= 0.93 and specificity= 0.62 for both features, as presented in Table 3 and Figure 3. Four features, kurtosis, intensity histogram root mean square, NGTDM strength, and GLSZM normalized grey level non-uniformity, had relatively lower but acceptable discrimination ability, with AUCs of 0.64, 0.66, 0.6, and 0.61, respectively.

The optimal cut-off values for the two highest features to distinguish between responders and non-responders were obtained using the maximum Youden index (sensitivity + specificity- 1), as shown in Table 3. Figure 4 shows a boxplot of the significant values for the optimal cut-off values obtained using the maximum Youden index.

Discussion

Several studies have explored the radiomic features of HCC patients undergoing Y-90 radioembolization, akin to our investigation. A study by Aujay et al. (11) examined 22 cases of HCC post-Y-90 radioembolization, identifying 14 patients as non-responders and 8 as responders. They extracted 107 radiomic features from arterial-phase and portal-venous phase MRI images. Their ROC analysis highlighted four radiomic parameters (long run emphasis, minor axis length, surface area, and grey level non-uniformity on arterial phase images) as predictors of early response. However, none of the statistically significant

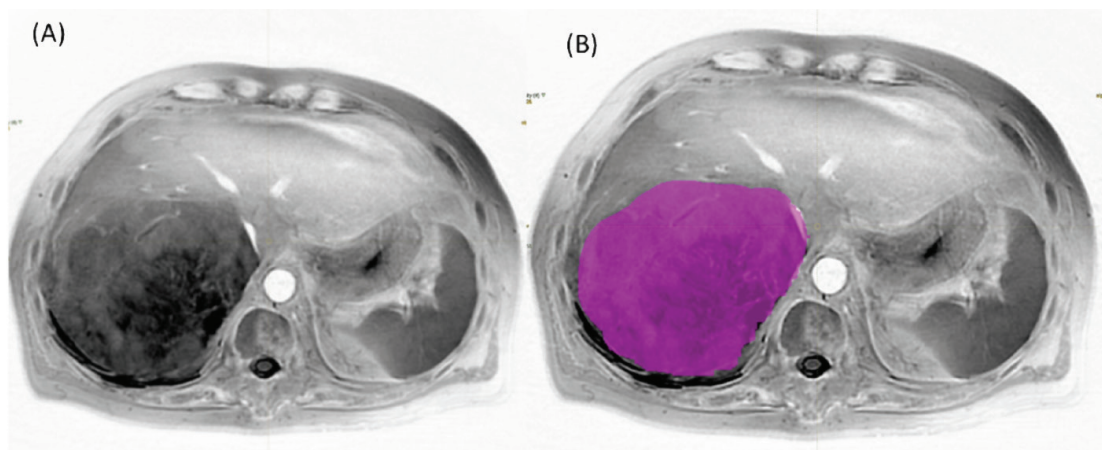


Figure 2. A case of a 58 years-old male with HCC (A) before, and (B) after segmentation in the LIFEx package
HCC: Hepatocellular carcinoma

Table 1. The results of the Mann-Whitney U test used to compare the responder and non-responder groups		
Variable	Test statistics z_R	p-value
Intensity histogram mean	-0.019	0.98
Intensity histogram variance	-0.704	0.48
Intensity histogram skewness	0.209	0.83
Intensity histogram kurtosis	1.199	0.23
Intensity histogram median	0.114	0.91
Intensity histogram 10 th percentile	0.514	0.61
Intensity histogram 25 th percentile	0.114	0.91
Intensity histogram 50 th percentile	-0.209	0.83
Intensity histogram 75 th percentile	-0.45	0.65
Intensity histogram 90 th percentile	-0.704	0.48
Intensity histogram standard deviation	-0.305	0.76
Intensity histogram mode	-0.93	0.35
Intensity histogram mean absolute deviation	-0.704	0.48
Intensity histogram robust mean absolute deviation	-0.704	0.48
Intensity histogram median absolute deviation	-0.66	0.51
Intensity histogram coefficient of variation	-1.123	0.26
Intensity histogram quartile coefficient of dispersion	-1.16	0.24
Intensity histogram entropy log ¹⁰	-0.74	0.46
Intensity histogram entropy log ²	-0.74	0.46
Intensity histogram area under curve	-0.59	0.55
Intensity histogram uniformity	0.78	0.43
Intensity histogram root mean square	1.31	0.19
Intensity histogram maximum histogram gradient	-0.59	0.55
Intensity histogram maximum histogram gradient grey level	0	1
Intensity histogram minimum histogram gradient	0.59	0.55
Intensity histogram minimum histogram gradient grey level	-0.019	0.98
Histogram intensity peak discretized volume sought	0.305	0.76
HISTOGRAM global intensity peak 0.5mL	-0.89	0.37
Intensity peak discretized volume sought 1mL	-0.87	0.38
Histogram global intensity peak 1mL	-1.23	0.21
GLCM joint maximum	-0.552	0.58
GLCM joint average	-0.209	0.83
GLCM joint variance	0.74	0.46
GLCM joint entropy log ²	-0.43	0.66
GLCM joint entropy log ¹⁰	-0.43	0.66
GLCM difference average	0.51	0.61
GLCM difference variance	0.36	0.72
GLCM difference entropy	-0.43	0.66
GLCM sum average	-0.209	0.83
GLCM sum variance	-0.971	0.33
GLCM sum entropy	-0.43	0.66

Table 1. Continued		
Variable	Test statistics z_R	p-value
GLCM angular second moment	0.47	0.63
GLCM contrast	0.36	0.71
GLCM dissimilarity	0.51	0.61
GLCM inverse difference	-0.36	0.72
GLCM normalised inverse difference	-0.51	0.61
GLCM inverse difference moment	-0.32	0.75
GLCM normalised inverse difference moment	-0.4	0.68
GLCM inverse variance	-0.55	0.58
GLCM correlation	-1.04	0.29
GLCM autocorrelation	-0.171	0.86
GLCM cluster tendency	-0.97	0.33
GLCM cluster shade	-0.47	0.63
GLCM cluster prominence	-0.85	0.39
GLRLM short runs emphasis	0.362	0.71
GLRLM long runs emphasis	-0.43	0.66
GLRLM low grey level run emphasis	-0.43	0.66
GLRLM high grey level run emphasis	-0.28	0.77
GLRLM short run low grey level emphasis	-0.095	0.92
GLRLM short run high grey level emphasis	-0.43	0.66
GLRLM long run low grey level emphasis	-0.476	0.63
GLRLM long run high grey level emphasis	-0.81	0.41
GLRLM grey level non uniformity	-0.704	0.48
GLRLM run length non uniformity	-1.047	0.29
GLRLM run percentage	0.209	0.83
NGTDM coarseness	0.72	0.47
NGTDM contrast	-0.209	0.83
NGTDM busyness	-0.78	0.43
NGTDM complexity	4	0.68
NGTDM strength	0.81	0.41
GLSZM small zone emphasis	1.8	0.07
GLSZM large zone emphasis	-0.85	0.39
GLSZM low gray level zone emphasis	-0.43	0.66
GLSZM high gray level zone emphasis	-0.13	0.89
GLSZM small zone low grey level emphasis	-0.24	0.804
GLSZM small zone high grey level emphasis	0.17	0.86
GLSZM large zone low grey level emphasis	-0.62	0.52
GLSZM large zone high grey level emphasis	-1.04	0.29
GLSZM grey level non-uniformity	-0.66	0.51
GLSZM normalized grey level non-uniformity	0.895	0.37
GLSZM zone size non-uniformity	-0.7	0.48
GLSZM normalized zone size non-uniformity	1.808	0.07
GLSZM zone percentage	0.704	0.48

Table 1. Continued		
Variable	Test statistics z_R	p-value
GLSZM grey level variance	-0.74	0.46
GLSZM zone size variance	-0.704	0.48
GLSZM zone size entropy	-2.3	0.02

GLCM: Grey Level Co-occurrence Matrix, GLRLM: Gray Level Run Length Matrix, NGTDM: Neighbourhood gray-tone difference matrix, GLSZM: Grey Level Size Zone Matrix

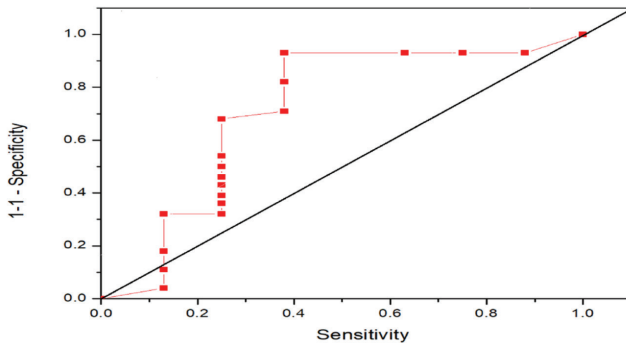


Figure 3. ROC curve for GLSZM-Small Zone Emphasis and GLSZM-Normalized Zone Size Non-Uniformity
 ROC: Receiver operating characteristic, GLSZM: Grey Level Size Zone Matrix

features from their study aligned with our findings. Conversely, Ince et al. (12) conducted a study with a larger cohort comprising 82 HCC patients (65 responders and 17 non-responders). They analyzed 1128 radiomic features extracted from pretreatment contrast-enhanced T1-weighted MRI scans obtained within three months before Y-90 treatment. Employing machine learning models, they identified eight radiomic features (including four first-

order features, such as kurtosis, three GLCM features, and one shape feature) as optimal predictors for treatment response. Interestingly, one significant feature from their study (Kurtosis) corroborates our findings. Table 4 presents a comparison between previous studies and our current investigation.

Other studies have explored the Y-90 treatment response for HCC or other liver malignancies using diverse imaging modalities(15-17). Reimer et al. (15) assessed the efficacy of texture analysis based on post-treatment MRI of liver metastases in 37 patients to predict response to Y-90 radioembolization during follow-up for colon cancer. They exclusively utilized first-order histogram features, with Kurtosis being the sole feature aligning with our current study. Blanc-Durand et al. (16) employed whole-liver radiomics to devise a scoring system predicting progression-free survival and overall survival in unresectable HCC patients undergoing Y-90 radioembolization. Utilizing 39 imaging features, they developed a two-predictive scoring system categorizing HCC patients into low- and high-risk subgroups in a retrospective cohort of 47 patients. Key radiomics features in their predictive model included variance and NGTDM strength, mirroring aspects of our study. In a separate study, Wei et al. (17) utilized a cohort

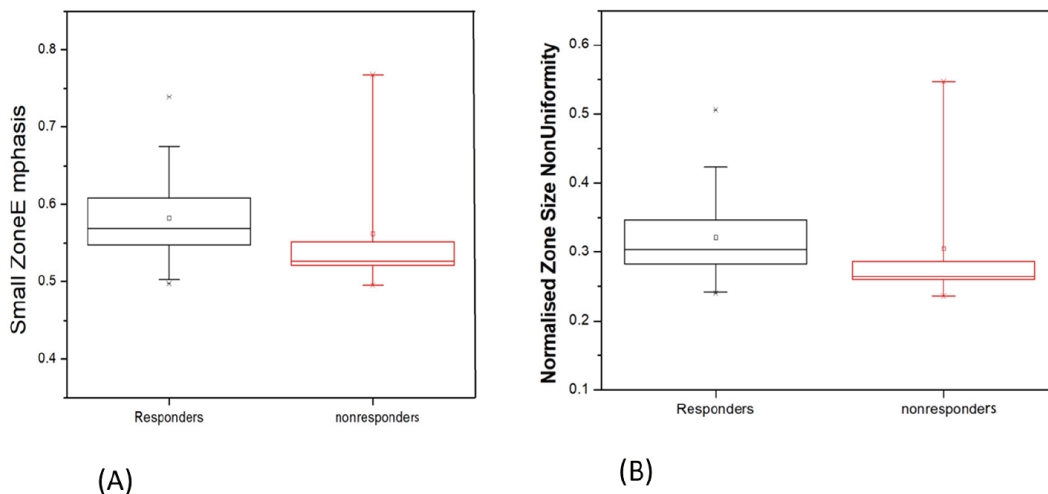


Figure 4. Box plot of (A) GLSZM-Small Zone Emphasis and (B) GLSZM-Normalized Zone Size Non-Uniformity
 GLSZM: Grey Level Size Zone Matrix

Table 2. Area under curve (AUC) as calculated from ROC. The below cell shows the features with a good agreement level to differentiate between responders and non-responders. Where green cells show the features with acceptable discrimination values

Variable	Area	Std. Error	Asymptotic Sig.	
			Upper bound	Lower bound
Intensity histogram mean	0.5	0.11	1	0.32
Intensity histogram variance	0.42	0.1	0.493	0.25
Intensity histogram skewness	0.53	0.1	0.819	0.37
Intensity histogram kurtosis	0.64	0.11	0.223	0.46
Intensity histogram median	0.52	0.11	0.894	0.34
Intensity histogram 10 th percentile	0.58	0.11	0.493	0.4
Intensity histogram 25 th percentile	0.56	0.1	0.594	0.4
Intensity histogram 50 th percentile	0.52	0.11	0.894	0.34
Intensity histogram 75 th percentile	0.48	0.11	0.849	0.3
Intensity histogram 90 th percentile	0.45	0.11	0.662	0.27
Intensity histogram standard deviation	0.42	0.1	0.493	0.25
Intensity histogram modei	0.47	0.11	0.775	0.29
Intensity histogram mean absolute deviation	0.39	0.11	0.361	0.22
Intensity histogram robust mean absolute deviation	0.42	0.11	0.493	0.24
Intensity histogram median absolute deviation	0.42	0.1	0.518	0.25
Intensity histogram coefficient of variation	0.37	0.11	0.27	0.2
Intensity histogram quartile coefficient of dispersion	0.37	0.11	0.254	0.19
Intensity histogram entropy log ¹⁰	0.42	0.1	0.47	0.24
Intensity histogram entropy log ²	0.42	0.1	0.47	0.24
Intensity histogram area under curve	0.43	0.12	0.568	0.24
Intensity histogram uniformity	0.59	0.11	0.424	0.42
Intensity histogram root mean square	0.66	0.13	0.183	0.44
Intensity histogram maximum histogram gradient	0.43	0.12	0.568	0.23
Intensity histogram maximum histogram gradient grey level	0.5	0.1	0.985	0.33
Intensity histogram minimum histogram gradient	0.57	0.12	0.543	0.37
Intensity histogram minimum histogram gradient grey level	0.5	0.11	1	0.32
Histogram intensity peak discretized volume sought	0.54	0.11	0.746	0.36
Histogram global intensity peak 0.5mL	0.4	0.12	0.381	0.2
Intensity peak discretized volume sought 1mL	0.4	0.1	0.392	0.23
Histogram global intensity peak 1mL	0.36	0.13	0.223	0.15
GLCM joint maximum	0.44	0.1	0.594	0.28
GLCM joint average	0.48	0.11	0.849	0.3
GLCM joint variance	0.42	0.1	0.47	0.25
GLCM joint entropy log ²	0.45	0.11	0.676	0.27
GLCM joint entropy log ¹⁰	0.45	0.11	0.676	0.27
GLCM difference average	0.56	0.12	0.594	0.37
GLCM difference variance	0.54	0.12	0.704	0.35
GLCM difference entropy	0.45	0.11	0.676	0.27
GLCM sum average	0.48	0.11	0.849	0.3

Table 2. Continued				
Variable	Area	Std. Error	Asymptotic Sig.	
			Upper bound	Lower bound
GLCM sum variance	0.39	0.1	0.341	0.22
GLCM sum entropy	0.45	0.11	0.676	0.27
GLCM angular second moment	0.56	0.1	0.621	0.39
GLCM contrast	0.54	0.11	0.704	0.36
GLCM dissimilarity	0.56	0.12	0.594	0.37
GLCM inverse difference	0.46	0.11	0.732	0.27
GLCM normalised inverse difference	0.44	0.12	0.621	0.25
GLCM inverse difference moment	0.46	0.11	0.761	0.28
GLCM normalised inverse difference moment	0.46	0.11	0.704	0.27
GLCM inverse variance	0.44	0.1	0.594	0.28
GLCM correlation	0.38	0.13	0.304	0.17
GLCM autocorrelation	0.48	0.11	0.879	0.3
GLCM cluster tendency	0.39	0.1	0.341	0.22
GLCM cluster shade	0.45	0.12	0.648	0.25
GLCM cluster prominence	0.4	0.1	0.403	0.24
GLRLM short runs emphasis	0.54	0.12	0.704	0.35
GLRLM long runs emphasis	0.45	0.11	0.676	0.27
GLRLM low grey level run emphasis	0.45	0.11	0.676	0.27
GLRLM high grey level run emphasis	0.49	0.11	0.909	0.31
GLRLM short run low grey level emphasis	0.47	0.11	0.79	0.28
GLRLM short run high grey level emphasis	0.49	0.11	0.939	0.31
GLRLM long run low grey level emphasis	0.45	0.11	0.648	0.27
GLRLM long run high grey level emphasis	0.41	0.1	0.424	0.23
GLRLM grey level non uniformity	0.42	0.13	0.493	0.21
GLRLM run length non uniformity	0.38	0.13	0.304	0.16
GLRLM run percentage	0.53	0.11	0.819	0.34
NGTDM coarseness	0.59	0.13	0.458	0.38
NGTDM contrast	0.48	0.11	0.849	0.3
NGTDM busyness	0.41	0.13	0.447	0.2
NGTDM complexity	0.55	0.11	0.676	0.36
NGTDM strength	0.6	0.14	0.403	0.37
GLSZM small zone emphasis	0.71	0.13	0.068	0.51
GLSZM large zone emphasis	0.4	0.12	0.403	0.2
GLSZM low gray level lzone emphasis	0.45	0.11	0.676	0.27
GLSZM high gray level zone emphasis	0.49	0.11	0.909	0.3
GLSZM small zone low grey level emphasis	0.47	0.11	0.819	0.29
GLSZM small zone high grey level emphasis	0.52	0.12	0.849	0.33
GLSZM large zone low grey level emphasis	0.43	0.11	0.543	0.24
GLSZM large zone high grey level emphasis	0.38	0.12	0.304	0.19
GLSZM grey level non-uniformity	0.42	0.13	0.518	0.2
GLSZM normalised grey level non-uniformity	0.61	0.11	0.361	0.43

Variable	Area	Std. Error	Asymptotic Sig.	
			Upper bound	Lower bound
GLSZM zone size non-uniformity	0.42	0.13	0.493	0.2
GLSZM normalised zone size non-uniformity	0.71	0.13	0.068	0.51
GLSZM zone percentage	0.58	0.12	0.47	0.39
GLSZM grey level variance	0.42	0.11	0.47	0.24
GLSZM zone size variance	0.42	0.12	0.493	0.23
GLSZM zone size entropy	0.23	0.13	0.022	0.02

ROC: Receiver operating characteristic, GLCM: Grey Level Co-occurrence Matrix, GLRLM: Gray Level Run Length Matrix, NGTDM: Neighbourhood gray-tone difference matrix, GLSZM: Grey Level Size Zone Matrix

Feature	Cut-off value	Sensitivity	Specificity	Yudin index
GLSZM-Small Zone Emphasis	0.53	0.93	0.62	0.51
GLSZM-Normalised Zone Size Non-Uniformity	0.27	0.93	0.62	0.55

GLSZM: Grey Level Size Zone Matrix

Factor/study	Aujay et al. (2022) (11)	Ince et al. (2023) (12)	Current study
Treatment type	Y-90 (glass+resin)	Y-90 (glass+resin)	Y-90 (glass+resin)
Patients population	22(5 glass, 17 resin)	82 (54 glass, 28 resin)	36 (19 glass, 17 resin)
Response	Responders= 14, Non-responders= 8	Responders= 65, Non-responders= 17	Responders= 28, Non-responders= 8
MRI phase	Arterial phase and portal venous phase MRI one month before and one month after treatment	contrast-enhanced T1-weighted MRI within 3 months before treatment	T2- MRI at the same day of receiving treatment
Post processing			
Number of Feature extracted	107	1.128	86 (the software extract 165 feature but some have errors and some not applicable on MRI so 86 features only included on the statistical work)
Number of significance features	4 (from the post arterial images pre and portal phase was non significance)	8 features	2 features
The most significant feature	GLRLM Long run emphasis With AUC= 1	Combined the 8 radiomics feature with 4 clinical feature to make 4 machine learning model models accuracy for the model between 80-87%	GLSZM-small zone emphasis, and GLSZM-normalized zone size non-uniformity with AUC= 0.71

MRI: Magnetic resonance imaging, GLSZM: Grey Level Size Zone Matrix, AUC: Area under curve,

of 30 patients with primary and secondary liver tumors treated with Y-90 and employed radiomics derived from Y-90 PET to predict treatment response. They identified 15 significant features, including NGTDM strength, consistent with our findings.

Discrepancies in features may stem from variations in sample size and the statistical analysis methodology. Additionally, radiomics holds promise in enhancing medical diagnosis, yet studies have uncovered variability in radiomics values due to several factors. These factors include the voxel size

(18,19), the algorithms used for reconstruction (20,21), the methods used for tumor segmentation (22,23), and the discretization of grey-level values (24,25). This variability in radiomics values can pose a challenge to the accuracy and reliability of radiomics-based diagnosis.

Study Limitations

The current study has certain limitations worth noting, such as a relatively small sample size, a restricted number of radiomic features analyzed, and absence of a comparison between our findings and other clinical information, such as histopathology results. Furthermore, we did not correlate the radiomics results with the clinical progression of the disease or liver function parameters. However, it's essential to emphasize that the primary objective of this study was to explore the predictive capacity of radiomics in determining Y-90 treatment response, with plans to expand upon these findings in our future research endeavors.

Conclusion

In conclusion, this study shows that radiomics extracted from MRI-T2 images could be used as a non-invasive tool for predicting the response of HCC to Y-90 treatment. Two radiomic features, "GLSZM-Small Zone Emphasis" and "GLSZM-Normalized Zone Size Non-Uniformity", were found to have the highest discrimination ability for differentiating responders from non-responders.

Ethics

Ethics Committee Approval: This study protocol was reviewed and approved by the Ethics Committee of Taipei Veterans General Hospital (IRB no: 2020-04-013BC, date: 13.04.2020). Informed consent was obtained from all subjects during inclusion in the study.

Informed Consent: Informed consent was obtained from all individual participants included in the study.

Authorship Contributions

Surgical and Medical Practices: M.M., K.H.L., R.C.L., Concept: M.M., Design: M.M., K.H.L., Data Collection or Processing: M.M., K.H.L., R.C.L., C.L., Analysis or Interpretation: M.M., K.H.L., R.C.L., C.L., Literature Search: M.M., Writing: M.M., K.H.L.

Conflict of Interest: No conflict of interest was declared by the authors.

Financial Disclosure: The authors declared that this study has received no financial support.

References

1. El-Serag HB. Hepatocellular carcinoma. *N Engl J Med.* 2011;365:1118-1127.
2. Salem R, Lewandowski RJ, Kulik L, Wang E, Riaz A, Ryu RK, Sato KT, Gupta R, Nikolaidis P, Miller FH, Yaghami V, Ibrahim SM, Senthilnathan S, Baker T, Gates VL, Atassi B, Newman S, Memon K, Chen R, Vogelzang RL, Nemcek AA, Resnick SA, Chrisman HB, Carr J, Omary RA, Abecassis M, Benson AB 3rd, Mulcahy MF. Radioembolization results in longer time-to-progression and reduced toxicity compared with chemoembolization in patients with hepatocellular carcinoma. *Gastroenterology.* 2011;140:497-507.
3. Kang TW, Kim JM, Rhim H, Lee MW, Kim YS, Lim HK, Choi D, Song KD, Kwon CH, Joh JW, Paik SW, Paik YH, Ahn JH. Small Hepatocellular Carcinoma: Radiofrequency Ablation versus Nonanatomic Resection-Propensity Score Analyses of Long-term Outcomes. *Radiology.* 2015;275:908-919.
4. Lencioni R, Llovet JM. Modified RECIST (mRECIST) assessment for hepatocellular carcinoma. *Semin Liver Dis.* 2010;30:52-60.
5. Aerts HJ, Velazquez ER, Leijenaar RT, Parmar C, Grossmann P, Carvalho S, Bussink J, Monshouwer R, Haibe-Kains B, Rietveld D, Hoebbers F, Rietbergen MM, Leemans CR, Dekker A, Quackenbush J, Gillies RJ, Lambin P. Decoding tumour phenotype by noninvasive imaging using a quantitative radiomics approach. *Nat Commun.* 2014;5:4006.
6. Kong C, Zhao Z, Chen W, Lv X, Shu G, Ye M, Song J, Ying X, Weng Q, Weng W, Fang S, Chen M, Tu J, Ji J. Prediction of tumor response via a pretreatment MRI radiomics-based nomogram in HCC treated with TACE. *Eur Radiol.* 2021;31:7500-7511.
7. Zhao Y, Wang N, Wu J, Zhang Q, Lin T, Yao Y, Chen Z, Wang M, Sheng L, Liu J, Song Q, Wang F, An X, Guo Y, Li X, Wu T, Liu AL. Radiomics Analysis Based on Contrast-Enhanced MRI for Prediction of Therapeutic Response to Transarterial Chemoembolization in Hepatocellular Carcinoma. *Front Oncol.* 2021;11:582788.
8. Kuang Y, Li R, Jia P, Ye W, Zhou R, Zhu R, Wang J, Lin S, Pang P, Ji W. MRI-Based Radiomics: Nomograms predicting the short-term response after transcatheter arterial chemoembolization (TACE) in hepatocellular carcinoma patients with diameter less than 5 cm. *Abdom Radiol (NY).* 2021;46:3772-3789.
9. Tian Y, Komolafe TE, Chen T, Zhou B, Yang X. Prediction of TACE Treatment Response in a Preoperative MRI via Analysis of Integrating Deep Learning and Radiomics Features. *J Med Biol Eng.* 2022;42:169-178.
10. Liu QP, Yang KL, Xu X, Liu XS, Qu JR, Zhang YD. Radiomics analysis of pretreatment MRI in predicting tumor response and outcome in hepatocellular carcinoma with transarterial chemoembolization: a two-center collaborative study. *Abdom Radiol (NY).* 2022;47:651-663.
11. Aujay G, Etchegaray C, Blanc JF, Lapuyade B, Papadopoulos P, Pey MA, Bordenave L, Trillaud H, Saut O, Pinaquy JB. Comparison of MRI-based response criteria and radiomics for the prediction of early response to transarterial radioembolization in patients with hepatocellular carcinoma. *Diagn Interv Imaging.* 2022;103:360-366.
12. Ince O, Önder H, Gençtürk M, Cebeci H, Golzarian J, Young S. Prediction of Response of Hepatocellular Carcinoma to Radioembolization: Machine Learning Using Preprocedural Clinical Factors and MR Imaging Radiomics. *J Vasc Interv Radiol.* 2023;34:235-243.
13. Nioche C, Orhac F, Boughdad S, Reuzé S, Goya-Outi J, Robert C, Pellot-Barakat C, Soussan M, Frouin F, Buvat I. LIFEX: A Freeware for Radiomic Feature Calculation in Multimodality Imaging to Accelerate Advances in the Characterization of Tumor Heterogeneity. *Cancer Res.* 2018;78:4786-4789.
14. Lencioni R, Llovet JM. Modified RECIST (mRECIST) assessment for hepatocellular carcinoma. *Semin Liver Dis.* 2010;30:52-60.
15. Reimer RP, Reimer P, Mahnken AH. Assessment of Therapy Response to Transarterial Radioembolization for Liver Metastases by Means of

- Post-treatment MRI-Based Texture Analysis. *Cardiovasc Intervent Radiol*. 2018;41:1545-1556.
16. Blanc-Durand P, Van Der Gucht A, Jreige M, Nicod-Lalonde M, Silva-Monteiro M, Prior JO, Denys A, Depeursinge A, Schaefer N. Signature of survival: a ^{18}F -FDG PET based whole-liver radiomic analysis predicts survival after ^{90}Y -TARE for hepatocellular carcinoma. *Oncotarget*. 2018;9:4549-4558.
 17. Wei L, Cui C, Xu J, Kaza R, El Naqa I, Dewaraja YK. Tumor response prediction in ^{90}Y radioembolization with PET-based radiomics features and absorbed dose metrics. *EJNMMI Phys*. 2020;7:74.
 18. Shafiq-Ul-Hassan M, Zhang GG, Latifi K, Ullah G, Hunt DC, Balagurunathan Y, Abdalah MA, Schabath MB, Goldgof DG, Mackin D, Court LE, Gillies RJ, Moros EG. Intrinsic dependencies of CT radiomic features on voxel size and number of gray levels. *Med Phys*. 2017;44:1050-1062.
 19. Shafiq-Ul-Hassan M, Latifi K, Zhang G, Ullah G, Gillies R, Moros E. Voxel size and gray level normalization of CT radiomic features in lung cancer. *Sci Rep*. 2018;8:10545.
 20. Altazi BA, Zhang GG, Fernandez DC, Montejó ME, Hunt D, Werner J, Biagioli MC, Moros EG. Reproducibility of F18-FDG PET radiomic features for different cervical tumor segmentation methods, gray-level discretization, and reconstruction algorithms. *J Appl Clin Med Phys*. 2017;18:32-48.
 21. van Velden FH, Kramer GM, Frings V, Nissen IA, Mulder ER, de Langen AJ, Hoekstra OS, Smit EF, Boellaard R. Repeatability of Radiomic Features in Non-Small-Cell Lung Cancer [(18)F]FDG-PET/CT Studies: Impact of Reconstruction and Delineation. *Mol Imaging Biol*. 2016;18:788-795.
 22. Qiu Q, Duan J, Duan Z, Meng X, Ma C, Zhu J, Lu J, Liu T, Yin Y. Reproducibility and non-redundancy of radiomic features extracted from arterial phase CT scans in hepatocellular carcinoma patients: impact of tumor segmentation variability. *Quant Imaging Med Surg*. 2019;9:453-464.
 23. Haniff NSM, Abdul Karim MK, Osman NH, Saripan MI, Che Isa IN, Ibahim MJ. Stability and Reproducibility of Radiomic Features Based Various Segmentation Technique on MR Images of Hepatocellular Carcinoma (HCC). *Diagnostics (Basel)*. 2021;11:1573.
 24. Duron L, Balvay D, Vande Perre S, Bouchouicha A, Savatovsky J, Sadik JC, Thomassin-Naggara I, Fournier L, Lecler A. Gray-level discretization impacts reproducible MRI radiomics texture features. *PLoS One*. 2019;14:e0213459.
 25. Mahmoud M, Shihab M, Saad S, Elhussiny F, Houseni M. Imaging differentiation of malignant hepatic tumors: Radiomics and metabolic features of ^{18}F -FDG PET/CT. *Russ Electron J Radiol*. 2021;11:165-170.



Prognostic Importance of ¹⁸F-FDG Positron Emission Tomography in Uterine Cervical Cancer

Uterin Serviks Kanserinde ¹⁸F-FDG Pozitron Emisyon Tomografisinin Prognostik Önemi

Çiğdem Soydal¹, Muhammet Halil Baltacıoğlu², Mine Araz¹, Burak Demir¹, Ecenur Dursun¹, Salih Taşkın³, Nuriye Özlem Küçük¹, Fırat Ortaç³

¹Ankara University Faculty of Medicine, Department of Nuclear Medicine, Ankara, Türkiye

²University of Health Sciences Türkiye, Trabzon Kanuni Training and Research Hospital, Clinic of Nuclear Medicine, Trabzon, Türkiye

³Ankara University Faculty of Medicine, Department of Obstetrics and Gynecology, Ankara, Türkiye

Abstract

Objectives: The aim of this study was to evaluate the prognostic value of ¹⁸F-fluorodeoxyglucose (¹⁸F-FDG) positron emission tomography/computed tomography (PET/CT) in the uterine cervix cancer patients.

Methods: Thirty-two women (mean age: 52.7±12.6) who underwent ¹⁸F-FDG PET/CT for staging of uterine cervix cancer were retrospectively recruited for the study. Maximum standardized uptake value (SUV_{max}), SUV_{mean}, metabolic tumor volume (MTV), and total lesion glycolysis (TLG) for primary tumors, lymph nodes, and distant metastases were calculated from ¹⁸F-FDG PET/CT images using the 40% threshold. Patients were divided into groups according to the presence of pelvic and para-aortic lymph node involvement on ¹⁸F-FDG PET/CT images. Life tables and Kaplan-Meier analyses were performed to compare the mean survival times of the different groups.

Results: Primary tumor of 27 (84%) patients were ¹⁸F-FDG avid. The median SUV_{max}, SUV_{mean}, MTV, and TLG of the primary tumors were 12.4, 6.1, 13.2 cm³ and 87.8 g/mL x cm³ respectively. Pathological uptake was detected in pelvic 14 (44%) patients and in paraaortic lymph nodes in 3 (10%) para-aortic lymph nodes. The median whole-body MTV and TLG were 21.7 cm³ and 91.1 g/mL x cm³. Disease progression was detected in 7 (22%) patients within a median follow-up period of 20.9 (minimum-maximum: 3-82) months. The only significant PET parameter to predict progression-free survival was SUV_{max} in the primary tumor (p=0.038). During follow-up period 8 patients died. SUV_{max} (p=0.007), MTV (p=0.036), TLG (p=0.001) of primary tumor, presence of pathological uptake on pelvic or paraaortic lymph nodes (p=0.015), whole-body MTV (p=0.047) and whole-body TLG (p=0.001) were found statistically significant PET parameters to predict overall survival.

Conclusion: Metabolic parameters of primary tumors derived from ¹⁸F-FDG PET/CT images have prognostic importance for patients with uterine cervical carcinoma. In patients with metastatic disease, higher whole-body MTV and TLG are also associated with poor prognosis.

Keywords: Uterine cervix cancer, ¹⁸F-FDG PET/CT, prognosis

Öz

Amaç: Bu çalışmanın amacı uterin serviks kanserli hastalarda ¹⁸F-florodeoksiglukoz (¹⁸F-FDG) pozitron emisyon tomografisi/bilgisayarlı tomografisinin (PET/BT) prognostik değerinin araştırılmasıdır.

Yöntem: Uterin serviks kanseri evrelemesi için ¹⁸F-FDG PET/BT yapılan 32 kadın (ortalama yaş: 52,7±12,6) retrospektif olarak çalışmaya dahil edildi. Primer tümörler, lenf nodları ve uzak metastazlar için maksimum standardize tutulum değeri (SUV_{max}), SUV_{ort} metabolik tümör hacmi

Presented in: Abstract of this manuscript has been accepted as poster presentation in 2023 annual meeting of EANM.

Address for Correspondence: Çiğdem Soydal MD, Ankara University Faculty of Medicine, Department of Nuclear Medicine, Ankara, Türkiye

Phone: +90 312 595 67 32 **E-mail:** csoyodal@yahoo.com ORCID ID: orcid.org/0000-0002-6199-8551

Received: 22.02.2024 **Accepted:** 23.06.2024 **Epub:** 17.07.2024



Copyright© 2024 The Author. Published by Galenos Publishing House on behalf of the Turkish Society of Nuclear Medicine. This is an open access article under the Creative Commons Attribution-NonCommercial-NoDerivatives 4.0 (CC BY-NC-ND) International License.

(MTV) ve toplam lezyon glikolizi (TLG) parametreleri, ¹⁸F-FDG PET/BT görüntülerinden %40 eşik değerine göre hesaplandı. Hastalar ¹⁸F-FDG PET/BT görüntülerinde pelvik ve paraaortik lenf nodu tutulumu varlığına göre gruplara ayrıldı. Farklı grupların ortalama sağkalım sürelerinin karşılaştırılması için sağkalım ve Kaplan-Meier analizleri yapıldı.

Bulgular: Hastaların 27'sinde (%84) primer tümörde ¹⁸F-FDG tutulumu gözlemlendi. Primer lezyonların SUV_{max}, SUV_{ort}, MTV ve TLG ortanca değerleri sırasıyla 12,4, 6,1, 13,2 cm³ ve 87,8 gr/mL x cm³ olarak hesaplandı. Hastaların 14'ünde (%44) pelvik ve 3'ünde (%10) paraaortik lenf nodlarında patolojik tutulum tespit edildi. Tüm vücut MTV ve TLG için ortanca değerler 21,7 cm³ ve 91,1 gr/mL x cm³ olarak hesaplandı. Ayrıca 20,9 aylık medyan takip (minimum-maksimum: 3-82) süresinde 7 (%22) hastada progresyon izlendi. Progresyonsuz sağkalımı öngören tek anlamlı parametere primer lezyonun SUV_{max}'i olarak bulundu (p=0,038). Takip süresi boyunca 8 hasta eksitus oldu. Genel sağkalımı öngören parametreler ise primer lezyonun SUV_{max}'i (p=0,007), MTV'si (p=0,036), TLG'si (p=0,001), pelvik veya paraaortik lenf nodlarında patolojik tutulum varlığı (p=0,015), tüm vücut MTV (p=0,047) ve tüm vücut TLG (p=0,001) olarak bulundu.

Sonuç: Uterin servikal karsinom hastalarında ¹⁸F-FDG PET/BT görüntülerinden elde edilen primer tümörün metabolik parametreleri prognostik öneme sahiptir. Metastatik hastalık durumunda daha yüksek toplam MTV ve TLG değerleri de kötü prognoz ile ilişkilidir.

Anahtar kelimeler: Uterin serviks kanseri, ¹⁸F-FDG PET/BT, prognoz

Introduction

Uterine cervical cancer is one of the most common cancers and the fourth leading cause of cancer-related death in women (1). Recurrence rates are changing based on the International Federation of Gynecology and Obstetrics (FIGO) staging range between 11% and 64% (2). In cases of recurrent disease, different treatment options are available according to disease spread. If local disease recurrence occurs, radical retreatment can be performed. However, this widespread disease can be treated with only systemic chemotherapy or supportive care (3).

FIGO stage, tumor size, presence of parametrial invasion, and presence of lymph node metastasis are well-known prognostic factors (4,5,6). Although they are not mandatory in disease staging, the role of non-invasive imaging modalities in the management of uterine cervical cancer is increasing (7,8,9). As a combined imaging technique, ¹⁸F-fluorodeoxyglucose (¹⁸F-FDG) positron emission tomography/computed tomography (PET/CT) has been proven to be a valuable tool in several aspects of uterine cervical cancer (10,11,12). Although maximum standardized uptake value (SUV_{max}) is the most widely used semiquantitative parameter for PET/CT evaluation, SUV_{max} has limitations, such as it is susceptible to noise and does not represent the entire tumor. For this reason, volume-based parameters, such as metabolic tumor volume (MTV) and total lesion glycolysis (TLG), are utilized to predict the biological behavior of tumors. They have been shown to be effective in prognostic prediction in several solid tumors (13,14). However, their role in patients with uterine cervical cancer is not yet well-established. For this reason, in this study, we aimed to evaluate the prognostic value of ¹⁸F-FDG PET/CT in the uterine cervix cancer patients.

Materials and Methods

Patient Population

Thirty-two women (mean age: 52.7±12.6) who underwent ¹⁸F-FDG PET/CT for the staging of uterine cervix cancer were retrospectively recruited for the study. All patients had pathologically proven uterine cervix cancer diagnosis. Patients were enrolled consecutively from January 2012 to September 2022. Informed consent was obtained from the patients for the scan and for accessing their hospital records. After PET/CT, patients were treated according to disease stage.

The Human Research Ethics Committee of Ankara University Faculty of Medicine approved this study (decision no.: İ01-68-24, date: 06.02.2024).

¹⁸F-FDG PET/CT Imaging

¹⁸F-FDG PET/CT imaging was performed using a GE Discovery 710 PET/CT scanner (GE Medical Systems, Milwaukee, USA) according to published guidelines for tumor imaging with PET/CT (15). Patients fasted at least 6 h before the examination, and their glucose levels were assessed. After 5.5 MBq/kg ¹⁸F-FDG injection, to clear background activity and reduce radiation exposure, patients were subjected to imaging after resting for 60 min in a quiet lead-lined room on semi-recumbent chairs. PET images were acquired for 4 min per bed position. The following parameters were used to obtain a low-dose CT scan before the PET scan. 140 kV, 70 mA, tube rotation time of 0.5 s per rotation, pitch of 6, and slice thickness of 5 mm.

Follow-up

Follow-up data were obtained from medical records, and surveillance was performed clinically, with aging [CT and/or magnetic resonance imaging (MRI) and/or ¹⁸F-FDG PET-CT] performed once a year, with a maximum (max) follow-

up period of up to 10 years. Progression was defined as the occurrence of cancer-related death, new lesions observed on follow-up imaging, or progression in the size and/or metabolic activity of existing lesions. Progression-free survival (PFS) was calculated from the day of PET/CT examination until disease progression was detected or the end of the follow-up period if no progression was detected. Overall survival (OS) was calculated from the day of PET/CT examination until death or end of the follow-up period if the patient was alive.

Image and Data Analysis

Reconstructed images were displayed as max intensity projection images, PET, CT, and fused PET/CT images in the axial, coronal, and sagittal planes re-evaluated retrospectively on a dedicated workstation (Advance Workstation 4.7 GE Medical Systems, Milwaukee, USA) for the presence of pathological uptake on primary tumors, pelvic lymph nodes, and distant organs by two experienced nuclear medicine specialists by consensus. SUV_{max} , SUV_{mean} , MTV, and TLG for primary tumors, lymph nodes, and distant metastases were calculated from ¹⁸F-FDG PET/CT images by the 40% threshold. In addition, whole-body MTV and TLG values were calculated by summing the MTV and TLG values for the primary tumor, lymph node, and distant organ metastases. Patients were divided into groups according to the presence of pelvic and para-aortic lymph node involvement on ¹⁸F-FDG PET/CT images.

Statistical Analysis

Baseline clinical and demographic information on the patients was analyzed using descriptive statistics. Categorical data are presented as frequencies, whereas continuous variables are presented as mean \pm standard deviation or median (interquartile range). Statistical analysis was performed using the commercially available software package SPSS 28.0. Normalcy was assessed using the Kolmogorov-Smirnov test. For non-normally distributed data, the Mann-Whitney U test, Kruskal-Wallis test, and Spearman rank test were used when appropriate. For normally distributed data, ANOVA with post-hoc Bonferroni correction, the student t-tests and the Pearson correlation test were used when appropriate. Life Tables and Kaplan-Meier analyses were performed to compare the mean survival times of the different groups. The log-rank method was used for this comparison. Statistical significance was defined as a p-value ≤ 0.05 .

Results

In total, 32 women with mean age: 52.7 ± 12.6 were included to the analysis. The majority of patients (75%)

had the squamous cell subtype, and the rest had adenocarcinoma. Following PET/CT imaging, 19 patients (60%) underwent total abdominal hysterectomy and bilateral salpingoophorectomy +/- pelvic lymph node dissection, 21 (65%) received radiation therapy, and 17 (53%) received chemotherapy. Patients were followed up for a mean of 52 months [minimum (min)- maximum (max): 3-133].

Primary tumors of 27 (84%) patients were ¹⁸F-FDG-avid. The median SUV_{max} , SUV_{mean} , MTV, and TLG of the primary tumors were 12.4, 6.1, 13.2 cm³ and 87.8 g/mL x cm³ respectively. Pathological uptake was detected in pelvic lymph nodes of 14 (44%) patients and in paraaortic lymph nodes in 3 (10%) para-aortic lymph nodes. Distant organ metastasis was detected in 7 (21%) patients. Two (6%) patients had peritoneal lymph node metastasis, 1 (3%) patient had surrenal gland metastasis, and 4 (13%) patients had distant lymph node metastasis. The median whole-body MTV and TLG were 21.7 cm³ and 91.1 g/mL x cm³.

Disease progression was detected in 7 (22%) patients within a median follow-up period of 20.9 (min-max: 3-82) months. The only significant PET parameter to predict PFS was SUV_{max} in the primary tumor. While patients who had a primary tumor with SUV_{max} higher than or equal to 12.4 had median 66.2 ± 13.6 months PFS, patients who have lower than 12.4 had 116.1 ± 8.5 months ($p=0.038$).

During the follow-up period 8 patients died. MTV (118.8 ± 9.1 vs. 78.8 ± 14.1 months, $p=0.036$), TLG (126.8 ± 6.4 vs. 47.4 ± 6.8 months, $p=0.001$), and SUV_{max} (125.6 ± 7.9 vs. 60.9 ± 10.1 months, $p=0.007$) values of the primary tumor, presence of pathological uptake on pelvic or para-aortic lymph nodes (111.0 ± 8.2 vs. 72.8 ± 17.2 months, $p=0.015$), whole-body MTV (118.8 ± 9.1 vs. 80.4 ± 14.0 months, $p=0.047$), and whole-body TLG (126.8 ± 6.4 vs. 47.4 ± 6.8 months, $p=0.001$) were found to be statistically significant PET parameters to predict OS. Survival analyses are detailed in Table 1. Examples of patients showing the relationship between PET/CT parameters and prognosis are shown in Figures 1 and 2. Survival curves of the different patient groups are presented in Figure 3. OS was better in patients without distant organ metastases, but the difference was not statistically significant (106.2 vs. 47.4 months, $p=0.11$).

Discussion

Because of the limitations of ¹⁸F-FDG PET/CT in the evaluation of primary tumors associated with myometrial and parametrial invasion, it is recommended for the assessment of pelvic lymph nodes and distant metastases in uterine

Table 1. Details of survival data of different patient groups			
Parameter	Median OS (months)	SD	p-value
MTV of primary tumor			
≥13.2	78.8	14.2	0.036
<13.2	118.9	9.1	
TLG of primary tumor			
≥87.8	47.4	6.8	0.001
<87.8	126.8	6.4	
SUV_{max} of primary tumor			
≥12.4	60.9	10.1	0.007
<12.4	125.6	7.9	
Presence of lymph node metastasis			
Present	72.8	17.2	0.015
Absent	111.0	8.2	
Whole-body MTV			
≥21.7	80.4	9.1	0.047
<21.7	118.8	14.0	
Whole-body TLG			
≥91.1	47.2	6.8	0.001
<91.1	126.8	6.4	

SUV: Standardized uptake value, MTV: Metabolic tumor volume, TLG: Total lesion glycolysis, OS: Overall survival, SD: Standard deviation

cervical cancer staging. However, metabolic parameters of primary tumors are known to have a prognostic role by providing information about the biological behavior of tumors in several solid tumors (16,17). Because of the rare incidence of uterine cervical cancer compared with other gynecological malignancies, the prognostic role of the metabolic parameters of the primary tumor assessed using ¹⁸F-FDG PET/CT is needed.

In this study, we investigated the prognostic role of ¹⁸F-FDG PET/CT in patients with uterine cervical carcinoma in terms of OS and PFS. Volume-based parameters, such as MTV and TLG, have been identified as predictors of PFS in patients with uterine cervical cancer in previous analyses (18,19). In a recent study, Markus et al. (20) showed that MTV and TLG were more effective in predicting the survival of patients with cervical cancer. In our study, we showed that primary tumor and whole-body MTV and TLG values were effective in predicting the OS. In addition, the SUV_{max} of the primary tumor and the presence of para-aortic-pelvic lymph nodes were found to be effective in predicting OS in our study. Budak et al. (21) showed that TLG and MTV were associated with PFS. In contrast to these findings in our analysis, only the SUV_{max} value of the primary tumor was found to be effective in predicting PFS for the prediction.

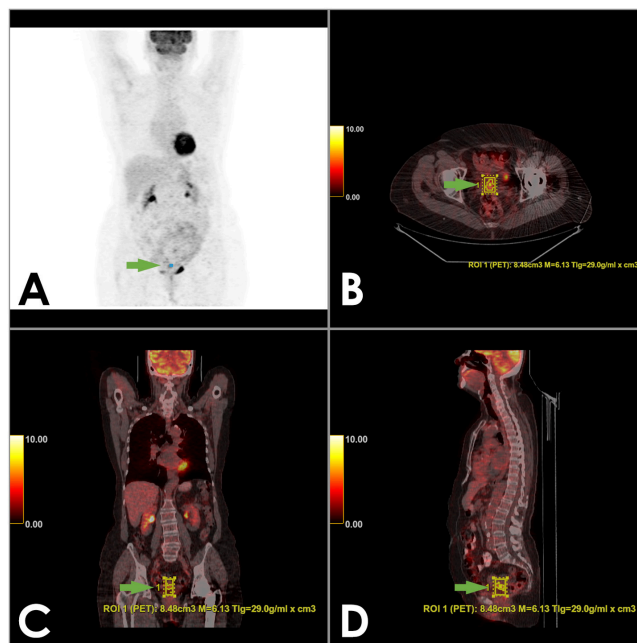


Figure 1. Maximum intensity projection PET (A), fused transaxial (B), coronal (C) and sagittal (D) PET/CT images of a 70 year-old woman with squamous cell uterine cervix carcinoma. She had a primary tumor with SUV_{max}: 6.13, MTV: 8.48 cm³ and TLG: 29.0 g/mL x cm³ without lymph node metastasis. After PET/CT imaging, she underwent TAH + BSO following by adjuvant chemo-radiation therapy. She has been followed-up for 46 months with no recurrent disease and still alive

PET: Positron emission tomography, CT: Computed tomography, SUV_{max}: Maximum standardized uptake value, MTV: Metabolic tumor volume, TLG: Total lesion glycolysis, TAH + BSO: Total abdominal hysterectomy with bilateral salpingo-oophorectomy, ROI: Region of interest

The limited number of included patients and different treatment strategies could be the reason for this difference in our group.

Despite these limitations in predicting OS, beyond SUV_{max}, MTV, and TLG were found to be significant factors. It is predicted that volume-based metabolic parameters have great potential for disease progression in uterine cervical cancer due to the heterogeneous nature of uterine cervical tumors due to the intra-tumoral variability of hypoxia, cellular proliferation, and blood flow; ¹⁸F-FDG uptake of the tumor is generally heterogeneous (5). Thus, SUV may not reflect exact metabolic activity of the entire tumor. The MTV reflects the volume of the area with higher uptake than the SUV_{max} threshold. The prognostic importance of TLG was not a surprise due to the known prognostic role of the tumor itself. TLG is calculated by multiplying MTV and SUV_{mean}, and it is hypothesized as a marker for the biological behavior of the tumor by providing information for tumor volume and glycolytic activity together. Despite the limited number of included patients, our analysis supported the hypothesis.

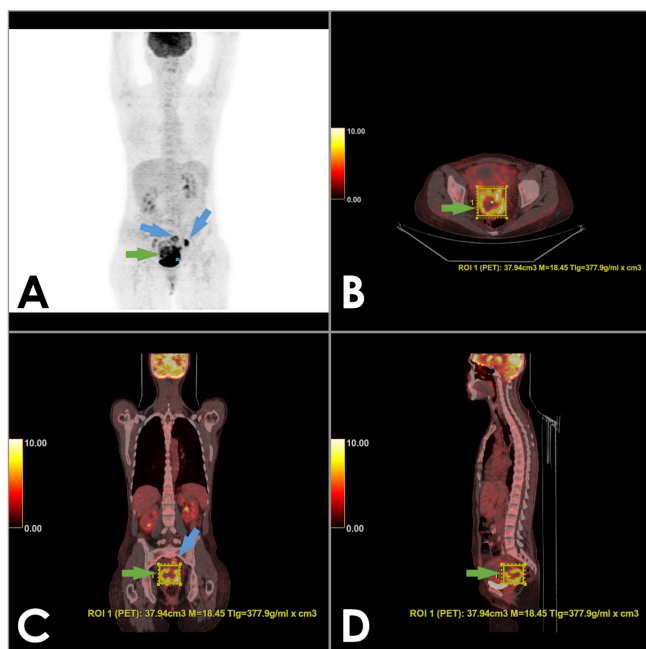


Figure 2. Maximum intensity projection (MIP) PET (A), fused transaxial (B), coronal (C) and sagittal (D) PET/CT images of a 33 year-old woman with squamous cell uterine cervix carcinoma. She had a primary tumor with SUV_{max} : 18.45, MTV: 37.94 cm^3 and TLG: 377.9 $\text{g/mL} \times \text{cm}^3$ with pelvic lymph node metastases. After PET/CT imaging, she underwent TAH + BSO following by adjuvant chemo-radiation therapy. She had recurrent disease at the 7th month and died at the 12th month after PET/CT

PET: Positron emission tomography, CT: Computed tomography, SUV_{max} : Maximum standardized uptake value, MTV: Metabolic tumor volume, TLG: Total lesion glycolysis, TAH + BSO: Total abdominal hysterectomy with bilateral salpingo-oophorectomy, ROI: Region of interest

The presence of lymph node metastases is a well-known prognostic factor in the uterine cervical cancer patients (22,23). Assessment of lymph node involvement using different imaging modalities showed a higher overall diagnostic performance of PET/CT in the per-patient and region- or node-based analyses. The sensitivity was 82%, 50%, and 56%, and the specificity was 95%, 90%, and 91% for PET/CT, CT, and MRI, respectively (23). In addition to the high diagnostic performance of ^{18}F -FDG PET/CT in the detection of lymph node metastases, the presence of pathological uptake in pelvic and para-aortic lymph nodes was found to be a significant prognostic factor in our analysis.

An advantage of ^{18}F -FDG PET/CT is that it is a whole-body imaging method. With this advantage, distant organ metastases were detected in 7 (22%) patients. To assess the prognostic importance of ^{18}F -FDG-positive distant organ metastasis, we additionally evaluated the prognostic role of whole-body MTV and TLG. Patients with a whole-body MTV higher than 21.7 cm^3 and TLG >91.1 $\text{gr/mL} \times \text{cm}^3$ were associated with shorter OS times than those without.

In a study investigating the effect of PET/MRI on survival in patients with cervical cancer, the SUV_{max} , MTV, and TLG values of the primary tumor were associated with PFS, but the SUV_{max} value was an independent predictor of PFS. It was also reported that the minimum apparent diffusion coefficient value was an independent predictor of OS. No significant correlation was found between MTV TLG and SUV_{max} and OS. This result was thought to be due to the small number of patients. In our study, we observed that

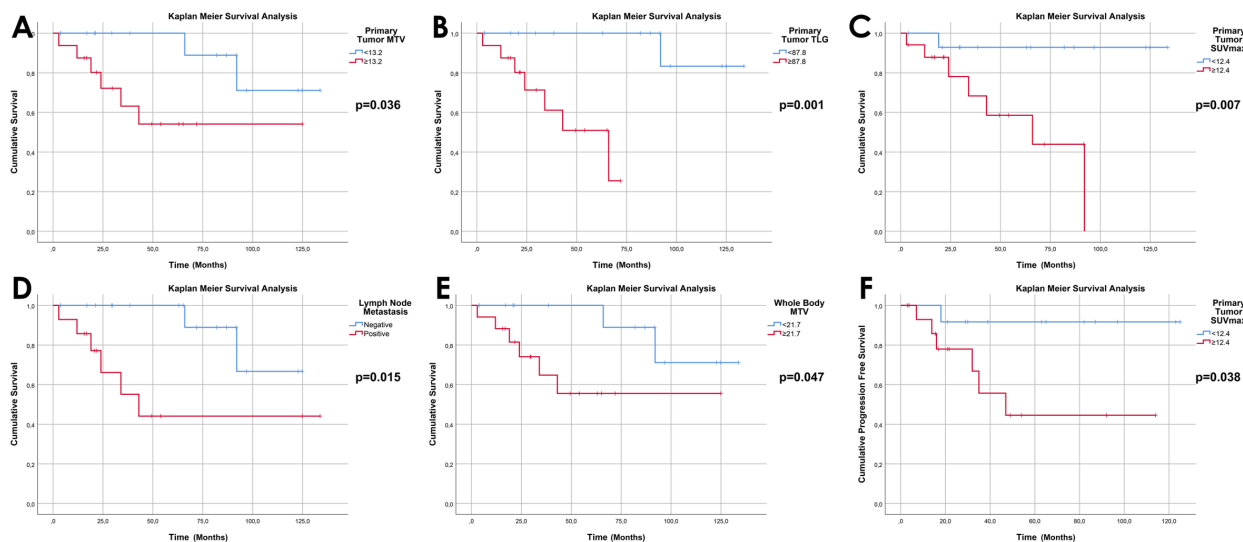


Figure 3. Kaplan-Meier survival curves of different subgroups of patients. Association of primary tumor MTV, TLG, SUV_{max} values with overall survival (A, B, C), Association of the presence of pelvic or paraaortic pathologic lymph nodes with overall survival (D), Association of whole-body MTV value with overall survival (E), Association of primary tumor SUV_{max} with progression-free survival (F). P-values were calculated with the long rank method
MTV: Metabolic tumor volume, TLG: Total lesion glycolysis, SUV_{max} : Maximum standardized uptake value

OS and PFS were lower in patients with higher SUV_{max} values for the primary tumor (24).

There are limitations to this study. First, it has a retrospective design and a limited number of patients. Second, the disease stages of the included patients were heterogeneous, and treatment strategies were not standardized. However, owing to its limitations, this study may contribute to the definition of the prognostic role of metabolic PET parameters for the prediction of uterine cervical cancer patients by considering the existence of limited data in this area.

Conclusion

Metabolic parameters of primary tumors derived from ¹⁸F-FDG PET/CT images have prognostic importance for patients with uterine cervical carcinoma. In patients with metastatic disease, higher whole-body MTV and TLG are also associated with poor prognosis.

Ethics

Ethics Committee Approval: The Human Research Ethics Committee of Ankara University Faculty of Medicine approved this study (decision no.: İ01-68-24, date: 06.02.2024).

Informed Consent: Patient consent was obtained.

Authorship Contributions

Surgical and Medical Practices: Ç.S., M.H.B., M.A., E.D., S.T., N.Ö.K., F.O., Concept: M.A., B.D., E.D., Design: Ç.S., M.H.B., M.A., B.D., E.D., Data Collection or Processing: Ç.S., M.H.B., M.A., B.D., Analysis or Interpretation: Ç.S., M.H.B., B.D., E.D., Literature Search: Ç.S., M.H.B., M.A., B.D., E.D., Writing: Ç.S., M.H.B.

Conflict of Interest: No conflict of interest was declared by the authors.

Financial Disclosure: The authors declared that this study has received no financial support.

References

- Sung H, Ferlay J, Siegel RL, Laversanne M, Soerjomataram I, Jemal A, Bray F. Global Cancer Statistics 2020: GLOBOCAN Estimates of Incidence and Mortality Worldwide for 36 Cancers in 185 Countries. *CA Cancer J Clin.* 2021;71:209-249.
- Quinn MA, Benedet JL, Odicino F, Maisonneuve P, Beller U, Creasman WT, Heintz AP, Ngan HY, Pecorelli S. Carcinoma of the cervix uteri. FIGO 26th Annual Report on the Results of Treatment in Gynecological Cancer. *Int J Gynaecol Obstet.* 2006;95(Suppl 1):43-103.
- Gandy N, Arshad MA, Park WE, Rockall AG, Barwick TD. FDG-PET Imaging in Cervical Cancer. *Semin Nucl Med.* 2019;49:461-470.
- Kantelhardt EJ, Moelle U, Begoihn M, Addissie A, Trocchi P, Yonas B, Hezkiel P, Stang A, Thomssen C, Vordermark D, Gemechu T, Gebrehiwot Y, Wondemagegnehu T, Aynalem A, Mathewos A. Cervical cancer in Ethiopia: survival of 1,059 patients who received oncologic therapy. *Oncologist.* 2014;19:727-734.
- Lee JH, Lee SW, Kim JR, Kim YS, Yoon MS, Jeong S, Kim JH, Lee JY, Eom KY, Jeong BK, Lee SH. Tumour size, volume, and marker expression during radiation therapy can predict survival of cervical cancer patients: a multi-institutional retrospective analysis of KROG 16-01. *Gynecol Oncol.* 2017;147:577-584.
- Twu NF, Ou YC, Liao CI, Chang WY, Yang LY, Tang YH, Chen TC, Chen CH, Chen TH, Yeh LS, Hsu ST, Chen YC, Chang CC, Cheng YM, Huang CY, Liu FS, Lin YS, Hsiao SM, Kan YY, Lai CH. Prognostic factors and adjuvant therapy on survival in early-stage cervical adenocarcinoma/adenosquamous carcinoma after primary radical surgery: A Taiwanese Gynecologic Oncology Group (TGOG) study. *Surg Oncol.* 2016;25:229-235.
- Wang YT, Li YC, Yin LL, Pu H. Can Diffusion-weighted Magnetic Resonance Imaging Predict Survival in Patients with Cervical Cancer? A Meta-Analysis. *Eur J Radiol.* 2016;85:2174-2181.
- Woo S, Suh CH, Kim SY, Cho JY, Kim SH. Magnetic resonance imaging for detection of parametrial invasion in cervical cancer: An updated systematic review and meta-analysis of the literature between 2012 and 2016. *Eur Radiol.* 2018;28:530-541.
- Patel CN, Nazir SA, Khan Z, Gleeson FV, Bradley KM. ¹⁸F-FDG PET/CT of cervical carcinoma. *AJR Am J Roentgenol.* 2011;196:1225-1233.
- Morkel M, Ellmann A, Warwick J, Simonds H. Evaluating the Role of F-18 Fluorodeoxyglucose Positron Emission Tomography/Computed Tomography Scanning in the Staging of Patients With Stage IIIB Cervical Carcinoma and the Impact on Treatment Decisions. *Int J Gynecol Cancer.* 2018;28:379-384.
- Ding XP, Feng L, Ma L. Diagnosis of recurrent uterine cervical cancer: PET versus PET/CT: a systematic review and meta-analysis. *Arch Gynecol Obstet.* 2014;290:741-747.
- Sarker A, Im HJ, Cheon GJ, Chung HH, Kang KW, Chung JK, Kim EE, Lee DS. Prognostic Implications of the SUVmax of Primary Tumors and Metastatic Lymph Node Measured by ¹⁸F-FDG PET in Patients With Uterine Cervical Cancer: A Meta-analysis. *Clin Nucl Med.* 2016;41:34-40.
- Pak K, Cheon GJ, Nam HY, Kim SJ, Kang KW, Chung JK, Kim EE, Lee DS. Prognostic value of metabolic tumor volume and total lesion glycolysis in head and neck cancer: a systematic review and meta-analysis. *J Nucl Med.* 2014;55:884-890.
- Im HJ, Pak K, Cheon GJ, Kang KW, Kim SJ, Kim IJ, Chung JK, Kim EE, Lee DS. Prognostic value of volumetric parameters of (18)F-FDG PET in non-small-cell lung cancer: a meta-analysis. *Eur J Nucl Med Mol Imaging.* 2015;42:241-251.
- Boellaard R, Delgado-Bolton R, Oyen WJ, Giammarile F, Tatsch K, Eschner W, Verzijlbergen FJ, Barrington SF, Pike LC, Weber WA, Stroobants S, Delbeke D, Donohoe KJ, Holbrook S, Graham MM, Testanera G, Hoekstra OS, Zijlstra J, Visser E, Hoekstra CJ, Pruim J, Willemsen A, Arends B, Kotzerke J, Bockisch A, Beyer T, Chiti A, Krause BJ; European Association of Nuclear Medicine (EANM). FDG PET/CT: EANM procedure guidelines for tumour imaging: version 2.0. *Eur J Nucl Med Mol Imaging.* 2015;42:328-354.
- Rijo-Cedeño J, Mucientes J, Álvarez O, Royuela A, Seijas Marcos S, Romero J, García-Berrocá JR. Metabolic tumor volume and total lesion glycolysis as prognostic factors in head and neck cancer: Systematic review and meta-analysis. *Head Neck.* 2020;42:3744-3754.
- Albano D. Metabolic tumor volume as prognostic factor in pediatric Hodgkin lymphoma: Dream or reality? *Pediatr Blood Cancer.* 2021;68:e29232.
- Han S, Kim H, Kim YJ, Suh CH, Woo S. Prognostic Value of Volume-Based Metabolic Parameters of ¹⁸F-FDG PET/CT in Uterine Cervical Cancer: A Systematic Review and Meta-Analysis. *AJR Am J Roentgenol.* 2018;211:1112-1121.

19. Herrera FG, Breuneval T, Prior JO, Bourhis J, Ozsahin M. [(18)F]FDG-PET/CT metabolic parameters as useful prognostic factors in cervical cancer patients treated with chemo-radiotherapy. *Radiat Oncol.* 2016;11:43.
20. Markus M, Sartor H, Bjurberg M, Trägårdh E. Metabolic parameters of [¹⁸F]FDG PET-CT before and after radiotherapy may predict survival and recurrence in cervical cancer. *Acta Oncol.* 2023;62:180-188.
21. Budak A, Budak E, Kanmaz AG, Inan AH, Tosun G, Beyan E, Aldemir OS, Ileri A. Volumetric PET parameters are predictive for the prognosis of locally advanced cervical cancer. *Q J Nucl Med Mol Imaging.* 2023;67:69-74.
22. Querleu D, Dargent D, Ansquer Y, Leblanc E, Narducci F. Extraperitoneal endosurgical aortic and common iliac dissection in the staging of bulky or advanced cervical carcinomas. *Cancer.* 2000;88:1883-1891.
23. Choi HJ, Ju W, Myung SK, Kim Y. Diagnostic performance of computer tomography, magnetic resonance imaging, and positron emission tomography or positron emission tomography/computer tomography for detection of metastatic lymph nodes in patients with cervical cancer: meta-analysis. *Cancer Sci.* 2010;101:1471-1479.
24. Shih IL, Yen RF, Chen CA, Cheng WF, Chen BB, Chang YH, Cheng MF, Shih TT. PET/MRI in Cervical Cancer: Associations Between Imaging Biomarkers and Tumor Stage, Disease Progression, and Overall Survival. *J Magn Reson Imaging.* 2021;53:305-318.



Cooccurrence of Capsular Liver Lesions Along with Peritoneal Carcinomatosis and Hematogenous Metastases in Ovarian Cancer Patients on Consecutive ¹⁸F-FDG PET/CT Studies

Ardışık ¹⁸F-FDG PET/BT İncelemeleri Olan Over Kanseri Hastalarındaki Kapsüler Karaciğer Lezyonlarının, Peritoneal Karsinomatozis ve Hematojen Metastazlar ile Birlikteliği

✉ Kemal Ünal, ✉ Levent Güner, ✉ Erkan Vardareli

Acıbadem University Faculty of Medicine, Department of Nuclear Medicine, İstanbul, Türkiye

Abstract

Objectives: The aim of our study was to evaluate the cooccurrence of capsular liver lesions along with peritoneal carcinomatosis and hematogenous metastases in other regions of the body in ovarian cancer patients on follow-up F-18 fluorodeoxyglucose (¹⁸F-FDG) positron emission tomography/computed tomography (PET/CT) studies.

Methods: Consecutive ¹⁸F-FDG PET/CT studies of 54 women with ovarian cancer between August 2012 and January 2020 and a total of 192 scans were analysed retrospectively. All patients had at least one hepatic and/or capsular lesion with high ¹⁸F-FDG uptake and at least two PET/CT examinations.

Results: According to interpretation, of 54 patients with hepatic or capsular lesions, 44 (81.4%), 5 (9.3%) and 5 (9.3%) of them were concluded as perihepatic implants, hematogenous liver metastases and both, respectively. Accompanying peritoneal carcinomatosis on follow-up PET/CT images was found in 42 (95.4%) and 3 (60%) patients with solely capsular lesions and solely hematogenous liver metastases, respectively. Extrahepatic hematogenous organ metastases on follow-up PET/CT images were seen in 4 (9.0%) and 3 (60%) patients with solely capsular lesions and solely hematogenous liver metastases, respectively. Lungs, bones, spleen and brain were detected metastases sites.

Conclusion: Cooccurrence of peritoneal carcinomatosis in other regions of abdomen was found to be higher in comparison to hematogenous organ metastases on consecutive PET/CT studies of ovarian cancer patients with capsular liver lesions. The primary opinion of the nuclear medicine physician is essential along with the other patient data for differential diagnosis and treatment approach in this particular patient group.

Keywords: Ovarian cancer, implants, liver metastasis, PET/CT

Öz

Amaç: Bu çalışmanın amacı over kanseri hastalarının ardışık F-18 florodeoksiglukoz (¹⁸F-FDG) pozitron emisyon tomografisi/bilgisayarlı tomografi (PET/BT) çalışmalarında görülen kapsüler karaciğer lezyonlarının, peritoneal karsinomatozis ve diğer vücut bölgelerindeki hematojen metastazlar ile olan birlikteliğini değerlendirmektir.

Yöntem: Over kanseri tanısı olan 54 kadının Ağustos 2012 ile Ocak 2020 tarihleri arasındaki toplam 192 ardışık¹⁸F-FDG PET/BT incelemesi retrospektif olarak değerlendirildi. Tüm hastaların yüksek düzeyde ¹⁸F-FDG tutulumu gösteren en az bir adet hepatik ve/veya kapsüler lezyonu ve en az iki tane PET/BT incelemesi vardı.

Bulgular: Değerlendirme sonrası hepatik veya kapsüler lezyonları olan 54 hastadan 44 tanesi (%81,4) perihepatik implant, 5 tanesi (%9,3) hematojen karaciğer metastazı ve 5 tanesi de (%9,3) her iki patolojiye de sahip olarak yorumlandı. Sadece kapsüler lezyon saptanan hastaların 42

Address for Correspondence: Kemal Ünal, Acıbadem University Faculty of Medicine, Department of Nuclear Medicine, İstanbul, Türkiye

Phone: +90 505 452 68 05 **E-mail:** kemalunal@dr.com ORCID ID: orcid.org/0000-0003-4023-7531

Received: 23.04.2024 **Accepted:** 11.08.2024 **Epub:** 03.10.2024



Copyright© 2024 The Author. Published by Galenos Publishing House on behalf of the Turkish Society of Nuclear Medicine. This is an open access article under the Creative Commons Attribution-NonCommercial-NoDerivatives 4.0 (CC BY-NC-ND) International License.

tanesinde (%95,4) ve sadece hematojen karaciğer metastazı saptanan hastaların da 3 tanesinde (%60) takip PET/BT incelemelerinde eşlik eden peritoneal karsinomatozis görüldü. Sadece kapsüler lezyon saptanan hastaların 4 tanesinde (%9,0) ve sadece hematojen karaciğer metastazı saptanan hastaların da 3 tanesinde (%60) ise takip PET/BT incelemelerinde eşlik eden ekstrahepatik hematojen organ metastazı görüldü. Akciğerler, kemikler, dalak ve beyin tespit edilen metastaz sahaları idi.

Sonuç: Ardışık PET/BT incelemeleri olan over kanseri hastalarında, kapsüler karaciğer lezyonlarına eşlik eden peritoneal karsinomatozis, hematojen organ metastazlarına oranla daha sık saptandı. Bu hasta grubu özelinde nükleer tıp uzmanının görüşü, ayırıcı tanı ve tedavi yaklaşımı açısından önemli bir role sahiptir.

Anahtar kelimeler: Over kanseri, implantlar, karaciğer metastazı, PET/BT

Introduction

The second most common gynaecological cancer among women is ovarian cancer. Early diagnosis is important, but mostly difficult due to low symptom rates. Most of the patients are diagnosed at advanced stage (1). It is more common in older women. Ovarian cancer has a high mortality rate with local and distant spread characteristics. Peritoneal, hematogenous and lymphatic metastases can be detected with several imaging modalities. Positron emission tomography/computed tomography (PET/CT), magnetic resonance imaging (MRI), CT, ultrasonography and bone scan are widely used for imaging. Each modality has its own advantages and limitations. Tumour markers can monitor disease progression. Surgical staging and interventional diagnostic procedures are also used for diagnostic and therapeutic approaches.

Cytoreductive surgery plays an important role in the treatment of ovarian cancer. Therefore, accurate staging or restaging should be done precisely. Implants can be seen especially in diaphragmatic, perihepatic, omental and paracolic regions (2). Hematogenous metastases are seen commonly in liver, lungs, bones and brain (3). Lymphatic spread is seen in pelvic, retroperitoneal, thoracic and supraclavicular stations.

^{18}F -fluorodeoxyglucose (^{18}F -FDG) is a glucose analogue with positron emission, which is used for PET/CT imaging. It is useful especially in detecting aggressive and poorly differentiated tumours. Whole-body scanning allows accurate imaging of cancer patients by detecting occult metastases or ruling out known suspicious lesions. Tissues with high metabolism have high glucose transporter activity, therefore, high ^{18}F -FDG uptake is seen in these lesions. ^{18}F -FDG PET/CT also allows to point the accurate biopsy site for lesions with faint borders or large necrotic components. High ^{18}F -FDG uptake is generally informative about poor prognosis. Lymphatic metastases without pathological enlargement can be detected by ^{18}F -FDG PET/CT. However, due to resolution characteristics of PET devices, subcentimeter foci may be missed, especially the lesions with low ^{18}F -FDG avidity. False positive findings

include infectious, inflammatory diseases and various benign pathologies. CT component of the device may be useful in differential diagnosis in these cases. Since ^{18}F -FDG is excreted via kidneys, lesions near bladder or ureters can be masked by these adjacent radiation sources. Intravenous diuretics, bladder catheterization and dual-phase images help reduce this limitation.

Peritoneal metastases adjacent to liver and subcapsular liver metastases are not rare conditions. Therefore, it is essential to differentiate peritoneal and hematogenous spread for accurate disease staging and decide treatment options.

The aim of our study was to evaluate the cooccurrence of capsular liver lesions along with peritoneal carcinomatosis and hematogenous metastases in other regions of the body in ovarian cancer patients on follow-up ^{18}F -FDG PET/CT studies.

Materials and Methods

Consecutive ^{18}F -FDG PET/CT studies of 54 women with ovarian cancer between August 2012 and January 2020 and a total of 192 scans were analysed retrospectively. All patients had at least one hepatic and/or capsular lesion with high ^{18}F -FDG uptake and at least two PET/CT examinations. Since all lesions in this particular group have high ^{18}F -FDG avidity, possible false negative PET studies were not evaluated in this paper. The median age of the patients was 58 years in our study (ranging 22-85). Imaging was performed 45-60 minutes after the intravenous injection of 0.1 mCi/kg FDG. Maximum standardized uptake value (SUV_{max}) measurement of the hottest lesion was calculated by volume of interest. Informed consent, patient preparation, imaging and reconstruction were made properly according to the European Association of Nuclear Medicine guideline (4). Follow-up PET/CT studies were performed after a minimum interval of three months (Figure 1). The mean number of PET/CT imaging per patient was 3.56 (ranging 2-12).

This study protocol was reviewed and approved by the Ankara Bilkent City Hospital Clinical Studies Ethics Committee (decision no.: E2-24-8598, date: 10.07.2024).

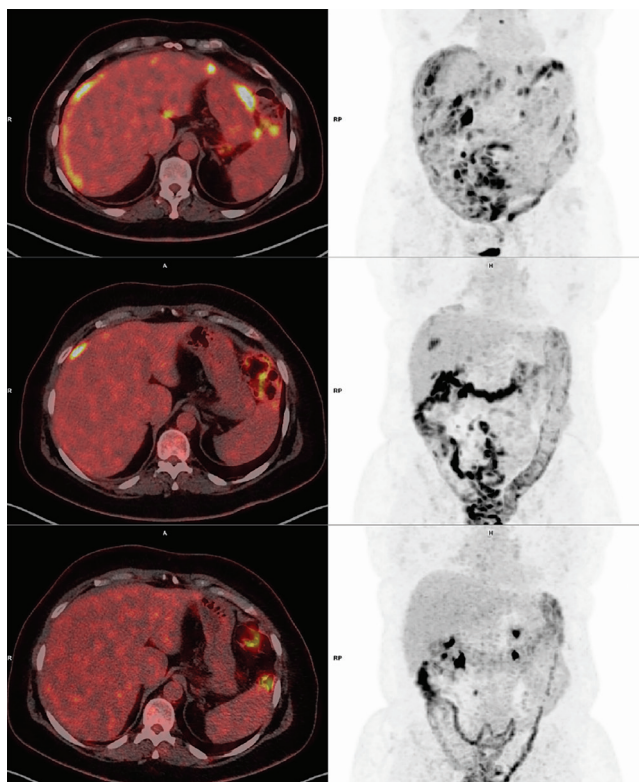


Figure 1. Fusion and maximum intensity projection images of ^{18}F -FDG PET/CT studies. No sign of capsular lesion on the bottom row images, which are the oldest dated. Development of hypermetabolic lesion on mid row. Progression and peritoneal carcinomatosis on top row, which are the most recent

^{18}F -FDG: F-18 fluorodeoxyglucose, PET/CT: Positron emission tomography/computed tomography

Statistical Analysis

Statistical analysis was performed by International Business Machines (IBM) Statistical Package for the Social Sciences Statistics for Windows (version 23.0, IBM Corp, Armonk, New York) software. For all analyses a p -value <0.05 was considered statistically significant. In this retrospective analysis, mean \pm Standard deviation of groups was calculated. Student's t -test was used to compare measurements of metastatic patient groups.

Results

According to interpretation, of 54 patients with hepatic or capsular lesions, 44 (81.4%), 5 (9.3%) and 5 (9.3%) of them were concluded as perihepatic implants, hematogenous liver metastases and both, respectively. Mean SUV_{max} measurements were calculated as 13.8 [standard deviation (SD) \pm 7.1] for capsular lesions and 16.2 (SD \pm 11.9) for liver metastases. No significant SUV_{max} difference was noted between these lesion groups ($p=0.2$).

Accompanying peritoneal carcinomatosis in other regions of abdomen on follow-up PET/CT images was found in 42 (95.4%) and 3 (60%) patients with solely capsular lesions and solely hematogenous liver metastases, respectively.

Lymphatic metastases on follow-up PET/CT images were detected in 31 (70.4%) and 3 (60%) patients with solely capsular lesions and solely hematogenous liver metastases, respectively.

Extrahepatic hematogenous organ metastases on follow-up PET/CT images were seen in 4 (9.0%) and 3 (60%) patients with solely capsular lesions and solely hematogenous liver metastases, respectively (Table 1). Lungs, bones, spleen and brain were detected metastases sites.

The ratio of "peritoneal carcinomatosis in other regions of abdomen" to "extrahepatic hematogenous organ metastases" in patients with solely capsular lesions were 42/4 (10.5). This ratio was found to be 3/3 (1) for patients with solely hematogenous liver metastases.

The ratio of "peritoneal carcinomatosis in other regions of abdomen" to "lymphatic metastases" in patients with solely capsular lesions were 42/31 (1.35). This ratio was found to be 3/3 (1) for patients with solely hematogenous liver metastases.

Discussion

Hypermetabolic lesion on ^{18}F -FDG PET/CT imaging in capsular region of liver can be a challenging diagnosis to locate, if it is an extracapsular implant or a subcapsular hematogenous metastasis. CT images of the study may even seem normal, especially when intravenous contrast agent is not used. We do not routinely inject intravenous contrast like most of the PET/CT facilities in our country. MR or PET/MRI may

Table 1. Cooccurrence of hepatic and extrahepatic lesions in ovarian cancer patients on ^{18}F -FDG PET/CT studies

	Number of patients	Peritoneal carcinomatosis in other regions of abdomen	Extrahepatic hematogenous organ metastases	Lymphatic metastases
Solely capsular lesions	44	42 (95.4%)	4 (9.0%)	31 (70.4%)
Solely hematogenous liver metastases	5	3 (60%)	3 (60%)	3 (60%)
Both capsular and parenchymal lesions	5	5 (100%)	1 (20%)	3 (60%)

^{18}F -FDG: F-18 fluorodeoxyglucose, PET/CT: Positron emission tomography/computed tomography

be helpful in these cases. Surgical staging also plays an important role in ovarian cancer (5). Since ovarian cancer tends to spread through peritoneal fluid and cytoreductive surgery plays an important role in treatment, differential diagnosis of peritoneal and hematogenous lesions are essential. Capsular region is the intersection of these two entities. Furthermore, patients with liver metastases have a poorer prognosis than patients with peritoneal implants. Our goal in this study was not to verify the exact location of capsular lesions of our patients. We used our data to identify the cooccurrence of these lesions along with peritoneal carcinomatosis and hematogenous metastases in other regions of the body on follow-up ^{18}F -FDG PET/CT studies.

In the literature, ^{18}F -FDG PET/CT was reported to alter the management of 60% of recurrent ovarian cancer patients by detecting especially subdiaphragmatic occult lesions (6). ^{18}F -FDG PET/CT is known to be valuable when detecting peritoneal carcinomatosis (7). Better diagnostic performance than MRI is also reported in the literature (8). Most of the patients with capsular lesions had peritoneal carcinomatosis on follow-up PET/CT examinations in our study. On the contrary, few of these patients developed extrahepatic metastatic disease on follow-up PET/CT studies. The high cooccurrence of capsular lesions with peritoneal carcinomatosis may be helpful when concluding PET/CT reports. This might also alert the nuclear medicine physician to acquire additional images to detect more implants in abdomen (9).

Furthermore, same cooccurrence was not found with lymphatic metastases. Since the mechanism of lymphatic spread is different than peritoneal and hematogenous metastases, it should be accurate to define hypermetabolic lymph nodes in comparison with previous studies and according to patient's clinical info, like histopathological type of tumour or infection and surgery history.

Study Limitations

The major limitation of our study is the lack of surgical and histopathological confirmation of lesions. However, unlike lymphatic or pulmonary lesions, few false-positive results have been found in literature (10,11) in perihepatic region, especially a long interval after surgery. The number of patients with solely hematogenous liver metastases were low. This may be another limitation of the study. However, our main purpose was to evaluate and follow-up capsular lesions.

Since the liver has moderate metabolic activity, it is obvious that capsular lesions must have higher ^{18}F -FDG uptake than adjacent parenchyma. This is one of the main limitations of

^{18}F -FDG PET/CT especially in small lesions with no significant mass formation on CT images. Perihepatic implants in our study had variable SUV_{max} measurements, all of which were higher than liver activity. No significant SUV_{max} difference was noted between perihepatic implants and hematogenous liver metastases. Literature results also reported variable ^{18}F -FDG uptake in these patient groups (12,13,14).

Extrahepatic hematogenous metastases sites in our study were consistent with the literature (3). ^{18}F -FDG PET/CT has also the capability of diagnosing second primary tumours (15). However, all extrahepatic lesions in our study were concluded as metastases related to ovarian cancer.

Conclusion

Hypermetabolic lesions in capsular region of liver on ^{18}F -FDG PET/CT imaging may be related to perihepatic implants or hematogenous liver metastases in ovarian cancer patients. The primary opinion of the nuclear medicine physician is essential along with the other patient data for differential diagnosis and treatment approach in this particular patient group. Cooccurrence of peritoneal carcinomatosis in other regions of abdomen was found to be higher in comparison to hematogenous organ metastases on follow-up PET/CT studies of these patients. Further studies with surgical and histopathological confirmation may help describing uptake patterns and the most common locations of perihepatic implants.

Ethics

Ethics Committee Approval: This study protocol was reviewed and approved by the Ankara Bilkent City Hospital Clinical Studies Ethics Committee (decision no.: E2-24-8598, date: 10.07.2024).

Informed Consent: Retrospective study.

Authorship Contributions

Surgical and Medical Practices: K.Ü., L.G., E.V., Concept: K.Ü., E.V., Design: K.Ü., L.G., Data Collection or Processing: K.Ü., L.G., Analysis or Interpretation: K.Ü., E.V., Literature Search: K.Ü., Writing: K.Ü.

Conflict of Interest: No conflict of interest was declared by the authors.

Financial Disclosure: The authors declared that this study has received no financial support.

References

1. Siegel RL, Miller KD, Jemal A. Cancer statistics, 2018. *CA Cancer J Clin.* 2018;68:7-30.
2. Meyers MA. Distribution of intra-abdominal malignant seeding: dependency on dynamics of flow of ascitic fluid. *Am J Roentgenol Radium Ther Nucl Med.* 1973;119:198-206.

3. Deng K, Yang C, Tan Q, Song W, Lu M, Zhao W, Lou G, Li Z, Li K, Hou Y. Sites of distant metastases and overall survival in ovarian cancer: A study of 1481 patients. *Gynecol Oncol.* 2018;150:460-465.
4. Boellaard R, Delgado-Bolton R, Oyen WJ, Giammarile F, Tatsch K, Eschner W, Verzijlbergen FJ, Barrington SF, Pike LC, Weber WA, Stroobants S, Delbeke D, Donohoe KJ, Holbrook S, Graham MM, Testanera G, Hoekstra OS, Zijlstra J, Visser E, Hoekstra CJ, Pruim J, Willemsen A, Arends B, Kotzerke J, Bockisch A, Beyers T, Chiti A, Krause BJ; European Association of Nuclear Medicine (EANM). FDG PET/CT: EANM procedure guidelines for tumour imaging: version 2.0. *Eur J Nucl Med Mol Imaging.* 2015;42:328-354.
5. Bogani G, Cromi A, Serati M, Di Naro E, Casarin J, Pinelli C, Ghezzi F. Laparoscopic and open abdominal staging for early-stage ovarian cancer: our experience, systematic review, and meta-analysis of comparative studies. *Int J Gynecol Cancer.* 2014;24:1241-1249.
6. Fulham MJ, Carter J, Baldey A, Hicks RJ, Ramshaw JE, Gibson M. The impact of PET-CT in suspected recurrent ovarian cancer: A prospective multi-centre study as part of the Australian PET Data Collection Project. *Gynecol Oncol.* 2009;112:462-468.
7. De Gaetano AM, Calcagni ML, Rufini V, Valenza V, Giordano A, Bonomo L. Imaging of peritoneal carcinomatosis with FDG PET-CT: diagnostic patterns, case examples and pitfalls. *Abdom Imaging.* 2009;34:391-402.
8. Sanli Y, Turkmen C, Bakir B, Iyibozkurt C, Ozel S, Has D, Yilmaz E, Topuz S, Yavuz E, Unal SN, Mudun A. Diagnostic value of PET/CT is similar to that of conventional MRI and even better for detecting small peritoneal implants in patients with recurrent ovarian cancer. *Nucl Med Commun.* 2012;33:509-515.
9. Lee JK, Min KJ, So KA, Kim S, Hong JH. The effectiveness of dual-phase 18F-FDG PET/CT in the detection of epithelial ovarian carcinoma: a pilot study. *J Ovarian Res.* 2014;5:7:15.
10. Ge J, Zuo C, Guan Y, Zhang X. Increased 18F-FDG uptake of widespread endometriosis mimicking ovarian malignancy. *Clin Nucl Med.* 2015;40:186-188.
11. Chen CJ, Yao WJ, Chou CY, Chiu NT, Lee BF, Wu PS. Peritoneal tuberculosis with elevated serum CA125 mimicking peritoneal carcinomatosis on F-18 FDG-PET/CT. *Ann Nucl Med.* 2008;22:525-527.
12. Li Y, Li F, Li X, Qu L, Han J. Value of 18F-FDG PET/CT in patients with hepatic metastatic carcinoma of unknown primary. *Medicine (Baltimore).* 2020;11;99:e23210.
13. Sacks A, Peller PJ, Surasi DS, Chatburn L, Mercier G, Subramaniam RM. Value of PET/CT in the management of liver metastases, part 1. *AJR Am J Roentgenol.* 2011;197:256-259.
14. Son H, Khan SM, Rahaman J, Cameron KL, Prasad-Hayes M, Chuang L, Machac J, Heiba S, Kostakoglu L. Role of FDG PET/CT in staging of recurrent ovarian cancer. *Radiographics.* 2011;31:569-583.
15. Kempainen J, Hynninen J, Virtanen J, Seppänen M. PET/CT for Evaluation of Ovarian Cancer. *Semin Nucl Med.* 2019;49:484-492.



An Unusual Case of Oligometastases in a Patient with Renal Cell Carcinoma: Insights from ¹⁸F-FDG PET/CT

Renal Hücreli Karsinomlu Bir Hastada Olağandışı Bir Oligometastaz Olgusu:
¹⁸F-FDG PET/BT'nin Faydası

✉ Akram Al-Ibraheem¹, ✉ Ahmed Saad Abdlkadir¹, ✉ Batool Albalooshi², ✉ Alaa' Abufara³, ✉ Kamal Al-Rabi³

¹King Hussein Cancer Center (KHCC), Department of Nuclear Medicine, Amman, Jordan

²Dubai Nuclear Medicine and Molecular Imaging Center, Dubai Health Authority, Dubai, United Arab Emirates

³King Hussein Cancer Center (KHCC), Department of Medical Oncology, Amman, Jordan

Abstract

Renal cell carcinoma (RCC) is a significant cause of mortality worldwide. To date, many atypical metastatic sites have been observed and reported in patients with RCC. However, to the best of our knowledge, there have been no reported cases of thyroid cartilage metastasis in the context of RCC metastasis. Herein, we present the case of a 68-year-old man who developed left arm pain that led to an RCC diagnosis. First, evaluation by pan-computed tomography (CT) denoted right kidney RCC and identified left humeral metastasis. Subsequently, ¹⁸F-fluorodeoxyglucose positron emission tomography/CT (¹⁸F-FDG PET/CT) was performed after right nephrectomy and left humeral lesion excision and fixation. Interestingly, few intramedullary hypermetabolic lesions were observed in addition to a single intensely hypermetabolic thyroid cartilage lesion indicative of oligometastases. This case underscores the importance of ¹⁸F-FDG PET/CT in the evaluation of RCC disease for baseline staging and beyond.

Keywords: Renal cell carcinoma, thyroid cartilage, renal cancer, ¹⁸F-FDG, cartilage metastasis, ¹⁸F-FDG PET/CT

Öz

Renal hücreli karsinom (RHK) dünya çapında önemli bir ölüm nedenidir. Bugüne kadar RHK'li hastalarda birçok atipik metastatik bölge gözlemlenmiş ve rapor edilmiştir. Ancak bildiğimiz kadarıyla RHK metastazı bağlamında tiroid kırkdak metastazı bildirilmiş bir olgu bulunmamaktadır. Burada RHK tanısı ile sonuçlanan sol kol ağrısı gelişen 68 yaşında bir erkek hastayı sunuyoruz. İlk olarak, pan-bilgisayarlı tomografi (BT) ile yapılan değerlendirmede sağ böbrekte RHK ve sol humerusta metastaz saptandı. Ardından sağ nefrektomi ve sol humerus lezyonunun eksizyonu ve fiksasyonu sonrası ¹⁸F-florodeoksiglukoz pozitron emisyon tomografisi/BT (¹⁸F-FDG PET/BT) yapıldı. İlginç bir şekilde, oligometastazın göstergesi olan tek bir yoğun hipermetabolik tiroid kırkdak lezyonuna ek olarak az sayıda intramedüller hipermetabolik lezyon gözlemlendi. Bu olgu, başlangıç evrelemesi ve ötesi için RHK değerlendirmesinde ¹⁸F-FDG PET/BT'nin önemini altını çizmektedir.

Anahtar kelimeler: Renal hücreli karsinom, tiroid kırkdak, böbrek kanseri, ¹⁸F-FDG, kırkdak metastazı, ¹⁸F-FDG PET/BT

Address for Correspondence: Akram Al-Ibraheem, MD, FEBNM, DCBNC, FANMB, King Hussein Cancer Center (KHCC), Department of Nuclear Medicine, Amman, Jordan

Phone: +96265300460 **E-mail:** akramalibrahim@gmail.com ORCID ID: orcid.org/0000-0002-0978-4716

Received: 02.12.2023 **Accepted:** 11.01.2024 **Epub:** 09.02.2024



Copyright© 2024 The Author. Published by Galenos Publishing House on behalf of the Turkish Society of Nuclear Medicine. This is an open access article under the Creative Commons Attribution-NonCommercial-NoDerivatives 4.0 (CC BY-NC-ND) International License.

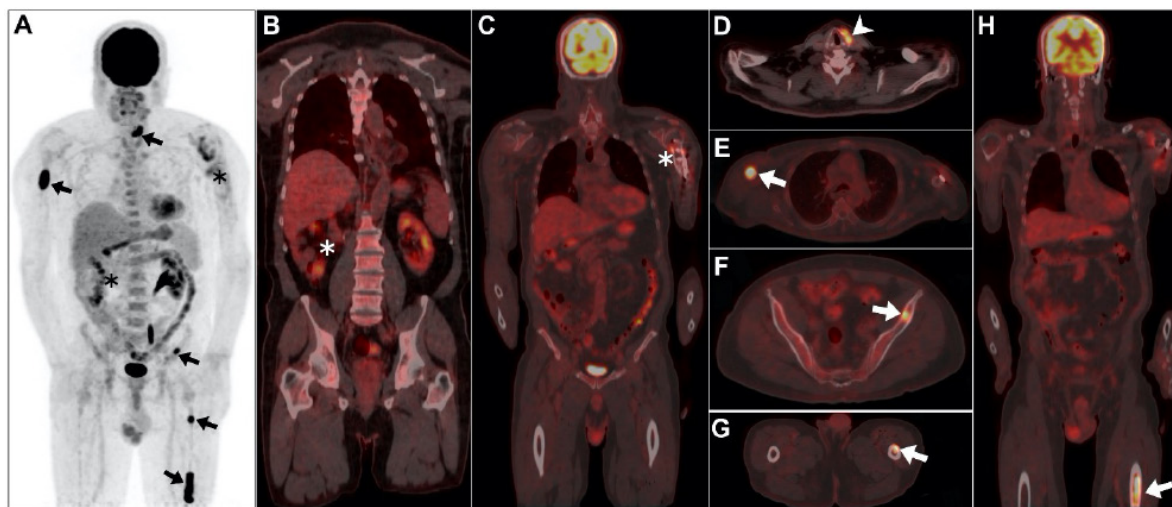


Figure 1. A 68-year-old male patient was recently diagnosed with renal cell carcinoma (RCC) of the right kidney. This was established after a major complaint of left arm pain, which necessitated further evaluation by pan-computed tomography (CT), which revealed evidence of a primary right renal malignancy and a single metastatic destructive left humeral shaft lesion. There was no radiological evidence of any other lesions elsewhere. Therefore, surgical interventions for both the primary and metastatic lesions were performed and included right nephrectomy and left humeral metastectomy with open reduction and internal fixation. The patient was then transferred to our cancer center for further management. Before starting therapy, a multidisciplinary clinic evaluation advocated further evaluation with ^{18}F -fluorodeoxyglucose positron emission tomography/CT (^{18}F -FDG PET/CT) before therapy initiation. The scan was conducted following the standard protocol after 60 min of intravenous administration of 7.3 mCi of ^{18}F -FDG. Maximum intensity projection image revealing evidence of multiple hypermetabolic metastatic extrarenal sites (A; arrows). This was observed concurrently with unremarkable surgical sites for both the primary tumor and the previously identified metastatic left arm lesion (A-C; asterisks). Notably, there is evidence of an intense hypermetabolic focus involving the left thyroid cartilage (maximum standardized uptake value of 13.9; arrowhead, D). In addition, multiple hypermetabolic intramedullary lesions were observed within the right proximal humerus, left iliac bone, and left femoral shaft (arrows; E-H). Histopathological examination of the oligometastatic lesions was considered unnecessary because of the patient's refusal and its lack of impact on the forthcoming management strategy. The hypermetabolic left thyroid cartilage deposit, which lacks identifiable structural characteristics, strongly suggests metastasis rather than primary involvement (1). This inference is supported by its distinct ^{18}F -FDG uptake, which is contrary to typical primary cartilaginous lesions, which usually exhibit lower ^{18}F -FDG uptake and evident radiographic manifestations (2). The lesion's unifocal and intense ^{18}F -FDG expression further diminishes the likelihood of a benign process. RCC is a lethal tumor that accounts for approximately 3% of all adult malignancies (3). The adoption and widespread use of molecular imaging techniques have led to a noteworthy rise in the accidental discovery of atypical metastatic manifestations (4). Our patient was initially diagnosed with a primary renal malignancy based on the presence of left arm discomfort caused by metastasis. Therefore, the traditional belief that primary RCC signs and symptoms should precede metastatic manifestations is more of an exception to a widespread principle. The progression of metastatic RCC does not always adhere to the traditional sequential metastatic pattern, suggesting a complex metastatic pathway (5). To date, numerous uncommon sites of metastasis have been identified (5). To the best of our knowledge, this is the first imaging instance where a patient with renal RCC established thyroid cartilage deposition as depicted on ^{18}F -FDG PET/CT. Thyroid cartilage metastasis is rare in all types of malignancies. Poor vascular supply of cartilaginous tissue is considered a contributing factor to its reduced tendency for metastasis (1). Nonetheless, there have been only a small number of documented instances where metastasis has occurred in the thyroid cartilage, typically associated with advanced cancer and serving as an indication of widespread metastatic disease (1,6,7,8,9). What makes this case more interesting is that thyroid cartilage metastasis is observed in patients with oligometastases. Notably, the previous evaluation using pan CT failed to depict cartilage and bone marrow oligometastases. This signifies the vital utility of ^{18}F -FDG PET/CT in the evaluation of RCC disease for baseline staging and beyond.

Ethics

Informed Consent: An informed consent was obtained from the patient.

Authorship Contributions

Surgical and Medical Practices: A.A-I., A.S.A., Concept: A.A-I., A.S.A., B.A., A.A., Design: A.A-I., A.S.A., B.A., K.A-R., Data Collection or Processing: A.A-I., A.A., Analysis or Interpretation: A.A-I., Literature Search: A.S.A., Writing: A.A-I., A.S.A., B.A., A.A., K.A-R.

Conflict of Interest: No conflicts of interest were declared by the authors.

Financial Disclosure: The authors declare that this study has received no financial support.

References

1. Gaber AM, Núñez R, Delpassand E. Cases of thyroid cartilage metastasis as abnormal findings seen in prostate cancer patients visualized by ⁶⁸Ga-PSMA-11 PET/CT. *Egypt J Radiol Nucl Med.* 2021;52:134.
2. Mendoza H, Nosov A, Pandit-Taskar N. Molecular imaging of sarcomas with FDG PET. *Skeletal Radiol.* 2023;52:461-475.
3. Siegel RL, Miller KD, Wagle NS, Jemal A. Cancer statistics, 2023. *CA Cancer J Clin.* 2023;73:17-48.
4. Griffin N, Gore ME, Sohaib SA. Imaging in metastatic renal cell carcinoma. *AJR Am J Roentgenol.* 2007;189:360-370.
5. Sountoulides P, Metaxa L, Cindolo L. Atypical presentations and rare metastatic sites of renal cell carcinoma: a review of case reports. *J Med Case Rep.* 2011;5:429.
6. Tripathy S, Parida GK, Singhal A, Shamim SA, Kumar R. Thyroid Cartilage Metastases on F-18 Fluorodeoxyglucose Positron Emission Tomography-Computed Tomography: A Tale of Two Cases with a Brief Review of Literature. *Indian J Nucl Med.* 2019;34:220-222.
7. Gupta N, Verma R, Belho ES. Metastatic Thyroid Cartilage Lesion from Prostatic Adenocarcinoma on ⁶⁸Ga-Prostate-Specific Membrane Antigen Positron Emission Tomography-Computed Tomography Scan: Case Series. *Indian J Nucl Med.* 2021;36:183-8.
8. Tupalli A, Damle NA, Thankarajan AS, Mangu BS, Kumar A, Khan D, Sagar S, Bal C. An Unusual Case of Simultaneous Cricoid and Thyroid Cartilage Metastases from Prostatic Adenocarcinoma on ⁶⁸Ga-PSMA PET/CT. *Nucl Med Mol Imaging.* 2020;54:61-62.
9. Usmani S, Ahmed N, Ilyas MW, Murad S, Al Kandari F. Rare Thyroid Cartilage Metastasis From Breast Cancer Visualized on ¹⁸F-NaF PET/CT. *Clin Nucl Med.* 2021;46:43-44.



¹⁸F-FDG PET/CT and ⁶⁸Ga-DOTATATE PET/CT Findings of Polycystic Kidney-derived Paraganglioma

Polikistik Böbrek Kaynaklı Paragangliomanın ¹⁸F-FDG PET/BT ve ⁶⁸Ga-DOTATATE PET/BT Bulguları

✉ Zehranur Tosunoğlu¹, ✉ Sevim Baykal Koca², ✉ Nurhan Ergül¹, ✉ Tevfik Fikret Çermik¹, ✉ Esra Arslan¹

¹University of Health Sciences Türkiye, İstanbul Training and Research Hospital, Clinic of Nuclear Medicine, İstanbul, Türkiye

²University of Health Sciences Türkiye, İstanbul Training and Research Hospital, Clinic of Pathology, İstanbul, Türkiye

Abstract

Paragangliomas (PGLs) are neuroendocrine tumors originating from the neural crest. They usually arise from the adrenal medulla and sympathetic or parasympathetic ganglions. Approximately 10% of PGLs are located in the extra-adrenal gland. Renal PGL is a rare condition. In this case report, we present the ¹⁸F-fluorodeoxyglucose positron emission tomography/computed tomography (PET/CT) and ⁶⁸Ga-DOTATATE PET/CT findings of polycystic kidney-derived PGL.

Keywords: Renal paraganglioma, ¹⁸F-FDG PET/CT, ⁶⁸Ga-DOTATATE PET/CT

Öz

Paragangliomalar (PGL'ler), nöral krestten köken alan nöroendokrin tümörlerdir. Genellikle adrenal medulla ve sempatik veya parasempatik ganglionlardan köken alırlar. PGL'lerin yaklaşık %10'u ekstraadrenal yerleşimlidir. Renal PGL nadir görülen bir durumdur. Bu olguda polikistik böbrek kaynaklı PGL'nin ¹⁸F-florodeoksiglukoz pozitron emisyon tomografisi/bilgisayarlı tomografi (PET/BT) ve ⁶⁸Ga-DOTATATE PET/BT bulgularını sunuyoruz.

Anahtar kelimeler: Renal paraganglioma, ¹⁸F-FDG PET/BT, ⁶⁸Ga-DOTATATE PET/BT

Address for Correspondence: Zehranur Tosunoğlu MD, University of Health Sciences Türkiye, İstanbul Training and Research Hospital, Clinic of Nuclear Medicine, İstanbul, Türkiye

Phone: +90 507 866 77 85 **E-mail:** zehranurtosunoglu@gmail.com **ORCID ID:** orcid.org/0000-0002-8509-1583

Received: 04.08.2023 **Accepted:** 28.01.2024 **Epub:** 09.02.2024



Copyright© 2024 The Author. Published by Galenos Publishing House on behalf of the Turkish Society of Nuclear Medicine. This is an open access article under the Creative Commons Attribution-NonCommercial-NoDerivatives 4.0 (CC BY-NC-ND) International License.

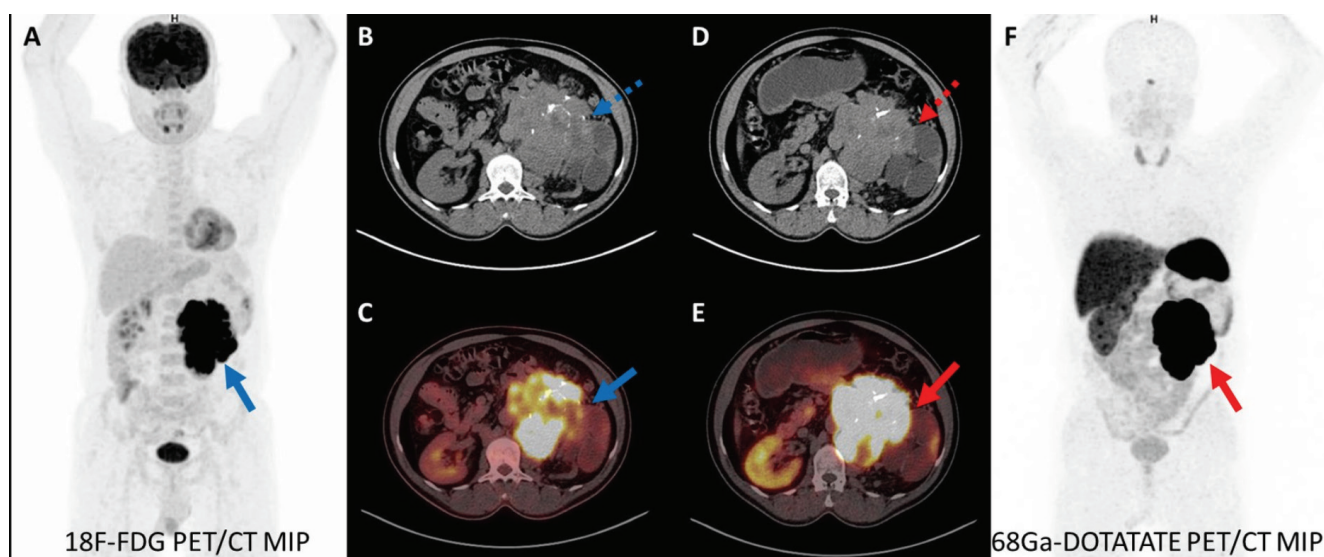


Figure 1. A 46-year-old man with no known medical conditions presented to the urology outpatient clinic with a complaint of left side pain and abdominal swelling that had been ongoing for 3 weeks. Blood and urine tests were normal. Abdominal magnetic resonance imaging and ultrasound revealed a mass in the lower pole of the left kidney measuring approximately 10x15 cm. ^{18}F -fluorodeoxyglucose positron emission tomography/computed tomography (^{18}F -FDG PET/CT) scan was performed with a preliminary diagnosis of renal cell cancer (RCC) (A). Transaxial CT sections showed a mass lesion with irregular borders measuring 8.5x15 cm that extended anteriorly from the inferior part of the left kidney and contained calcifications (B). Intense ^{18}F -FDG uptake was detected on the fusion images [maximum standardized uptake value (SUV_{max}): 32.7] (C). There were no regional or distant metastases. Tru-cut biopsy of the mass was diagnosed as paraganglioma (PGL) (Figure 2). ^{68}Ga -DOTATATE PET/CT imaging was performed for staging (F). Transaxial CT sections showed the left kidney to have a polycystic appearance, and a mass lesion measuring approximately 10x15 cm was present in the medial part of the left kidney (D). Intense DOTATATE receptor activation was observed on the fusion images (SUV_{max} : 75.8) (E). No regional or distant metastases were observed.

Extra-adrenal PGLs most commonly occur in the carotid body, vagal body, mediastinum, and retroperitoneum (1). Renal PGL is rare (1,2). In the genitourinary tract, the renal pelvis (4.9%) is the third primary site of PGLs, followed by the bladder (79.2%) and urethra (12.7%) (3). The clinical symptoms depend on the location of the mass in the kidney (2,4). Functional imaging methods play an important role in confirming diagnosis, staging, and restaging (5). PGLs contain high levels of somatostatin receptors (6,7). In a study evaluating 22 PGL patients with ^{68}Ga -DOTATATE PET/CT, the detection rate of lesions was 100% (8). In another study evaluating 23 patients with PGLs using ^{18}F -FDG PET/CT and ^{68}Ga -DOTATATE PET/CT, many regions were ^{68}Ga -DOTATATE and ^{18}F -FDG positive, but ^{18}F -FDG uptake was lower than ^{68}Ga -DOTATATE uptake (median SUV_{max} values were 12.5-21, respectively) (9). ^{68}Ga -DOTATATE PET/CT has higher diagnostic accuracy than ^{18}F -FDG PET/CT (10). Renal PGL should be considered when evaluating kidney masses because it can mimic RCC, and caution should be exercised.

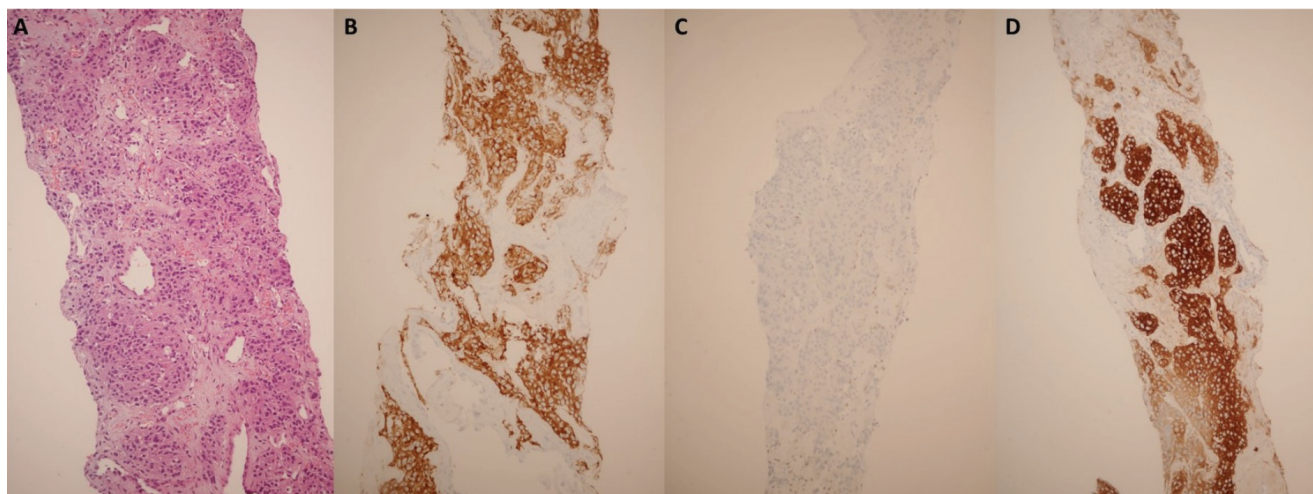


Figure 2. Tumor cells are arranged in a Zellballen pattern within a fibrovascular stroma (A, H&E x200). The tumor is strongly positive for chromogranin-A (B, x200). S-100 immunostain highlighting the focally preserved sustentacular cells (C, x200). Strong cytoplasmic positivity for tyrosine hydroxylase confirms the diagnosis of PGL (D, x200).

Ethics

Informed Consent: The patient consent was obtained.

Authorship Contributions

Surgical and Medical Practices: Z.T., S.B.K., N.E., T.FÇ., E.A., Concept: Z.T., S.B.K., T.FÇ., E.A., N.E., Design: Z.T., N.E., S.B.K., T.FÇ., E.A., Data Collection or Processing: Z.T., S.B.K., N.E., T.FÇ., E.A., Analysis or Interpretation: Z.T., S.B.K., N.E., T.FÇ., E.A., Literature Search: Z.T., S.B.K., N.E., T.FÇ., E.A., Writing: Z.T., T.FÇ., E.A., S.B.K., N.E.

Conflict of Interest: No conflicts of interest were declared by the authors.

Financial Disclosure: The authors declare that this study has received no financial support.

References

1. Neumann HPH, Young WF Jr, Eng C. Pheochromocytoma and Paraganglioma. *N Engl J Med.* 2019;381:552-565.
2. Bahar B, Pambuccian SE, Gupta GN, Barkan GA. Renal paraganglioma: report of a case managed by robotic assisted laparoscopic partial nephrectomy and review of the literature. *Case Rep Urol.* 2014;2014:527592.
3. Peng C, Bu S, Xiong S, Wang K, Li H. Non-functioning paraganglioma occurring in the urinary bladder: A case report and review of the literature. *Oncol Lett.* 2015;10:321-324.
4. Yi C, Han L, Yang R, Yu J. Paraganglioma of the renal pelvis: a case report and review of literature. *Tumori.* 2017;103(Suppl 1):e47-e49.
5. Taïeb D, Timmers HJ, Hindié E, Guillet BA, Neumann HP, Walz MK, Opocher G, de Herder WW, Boedeker CC, de Krijger RR, Chiti A, Al-Nahhas A, Pacak K, Rubello D; European Association of Nuclear Medicine. EANM 2012 guidelines for radionuclide imaging of pheochromocytoma and paraganglioma. *Eur J Nucl Med Mol Imaging.* 2012;39:1977-1995.
6. Sobocki BK, Perdyan A, Szot O, Rutkowski J. Management of Pheochromocytomas and Paragangliomas: A Case-Based Review of Clinical Aspects and Perspectives. *J Clin Med.* 2022;11:2591.
7. Şahin R, Baykal Koca S, Yüçetaş U, Çermik TF, Ergül N. 18F-FDG PET/CT and 68Ga-DOTATATE PET/CT Findings in a Patient With Primary Renal Well-Differentiated Neuroendocrine Tumor. *Clin Nucl Med.* 2022;47:e503-e505.
8. Skoura E, Priftakis D, Novruzov F, Caplin ME, Gnanasegaran G, Navalkisoor S, Bomanji J. The impact of Ga-68 DOTATATE PET/CT imaging on management of patients with paragangliomas. *Nucl Med Commun.* 2020;41:169-174.
9. Chang CA, Pattison DA, Tothill RW, Kong G, Akhurst TJ, Hicks RJ, Hofman MS. (68)Ga-DOTATATE and (18)F-FDG PET/CT in Paraganglioma and Pheochromocytoma: utility, patterns and heterogeneity. *Cancer Imaging.* 2016;16:22.
10. Carrasquillo JA, Chen CC, Jha A, Ling A, Lin FI, Pryma DA, Pacak K. Imaging of Pheochromocytoma and Paraganglioma. *J Nucl Med.* 2021;62:1033-1042.



Testicular Incidentaloma on ^{18}F -choline PET/CT in a Patient with Prostatic Adenocarcinoma

Prostatik Adenokarsinomlu Bir Hastada ^{18}F -kolin PET/BT ile Saptanan Testiküler İnsidentaloma

Chaymae Bensaid, Salah Oueriagli Nabih, Meryem Aboussabr, Omar Ait Sahel, Yassir Benameur, Abderrahim Doudouh

Mohammed V Military Training Hospital, Clinic of Nuclear Medicine, Rabat, Morocco

Abstract

Prostatic adenocarcinoma is characterized by elevated phosphatidylcholine metabolism. ^{18}F -choline positron emission tomography/computed tomography (PET/CT) is widely used for patients with biochemical recurrence and a prostate-specific antigen threshold above 2 ng/mL. We report a case of a patient with high-risk prostatic adenocarcinoma undergoing ^{18}F -choline PET/CT for biochemical recurrence. In addition to hypermetabolic abdominal lymph nodes, an unexpected right testicular hypermetabolism was observed. Such findings on ^{18}F -choline PET/CT may suggest a primary tumor or testicular metastasis of prostate cancer. Bilateral orchiectomy revealed a vitelline tumor associated with known primary prostatic cancer. The incidental discovery of a testicular vitelline tumor during prostate cancer imaging is rare, highlighting the importance of thorough diagnostics. This case underscores the need for comprehensive care in managing complex and atypical cancer cases, emphasizing the potential for unrelated tumor discoveries during diagnostic workup. Further research is essential for a better understanding of these rare co-occurring cancers and their treatment implications.

Keywords: ^{18}F -choline positron emission tomography/computed tomography, yolk tumor, prostatic adenocarcinoma

Öz

Prostatik adenokarsinom, yüksek fosfatidilkolin metabolizması ile karakterizedir. ^{18}F -kolin pozitron emisyon tomografisi/bilgisayarlı tomografi (PET/BT), biyokimyasal nüks olan ve prostat spesifik antijen düzeyi 2 ng/mL'nin üzerinde olan hastalarda yaygın olarak kullanılmaktadır. Biyokimyasal nüks nedeniyle ^{18}F -kolin PET/BT uygulanan yüksek riskli prostat adenokarsinomlu bir hastayı bildiriyoruz. Hipermetabolik karın lenf nodlarına ek olarak sağ testiste beklenmedik bir hipermetabolizma da gözlemlendi. ^{18}F -kolin PET/BT'deki bu tür bulgular, bir primer tümörü veya prostat kanserinin testiküler metastazını düşündürülebilir. Bilateral orşiektomi, bilinen primer prostat kanseri ile ilişkili bir vitellin tümörü ortaya çıkardı. Prostat kanseri görüntülemesi sırasında testiküler vitellin tümörünün tesadüfen keşfedilmesi nadirdir, bu da teşhise yönelik kapsamlı araştırmanın önemini vurgulamaktadır. Bu olgu, karmaşık ve atipik kanserli olgularının yönetilmesinde kapsamlı bakım ihtiyacının altını çizmekte ve teşhis için yapılan araştırmalar sırasında ilgisiz tümör keşiflerinin potansiyelini vurgulamaktadır. Nadiren birlikte ortaya çıkan bu kanserlerin ve bunların tedavilerinin yol açacağı etkilerin daha iyi anlaşılması için daha fazla araştırma yapılması gerekmektedir.

Anahtar kelimeler: ^{18}F -kolin pozitron emisyon tomografisi/bilgisayarlı tomografi, yolk tümörü, prostat adenokarsinomu

Address for Correspondence: Chaymae Bensaid MD, Mohammed V Military Teaching Hospital, Clinic of Nuclear Medicine, Rabat, Morocco

Phone: +212623511726 **E-mail:** chamabensaid@gmail.com ORCID ID: orcid.org/0009-0002-2164-0982

Received: 17.01.2024 **Accepted:** 12.02.2024 **Epub:** 20.02.2024



Copyright© 2024 The Author. Published by Galenos Publishing House on behalf of the Turkish Society of Nuclear Medicine. This is an open access article under the Creative Commons Attribution-NonCommercial-NoDerivatives 4.0 (CC BY-NC-ND) International License.

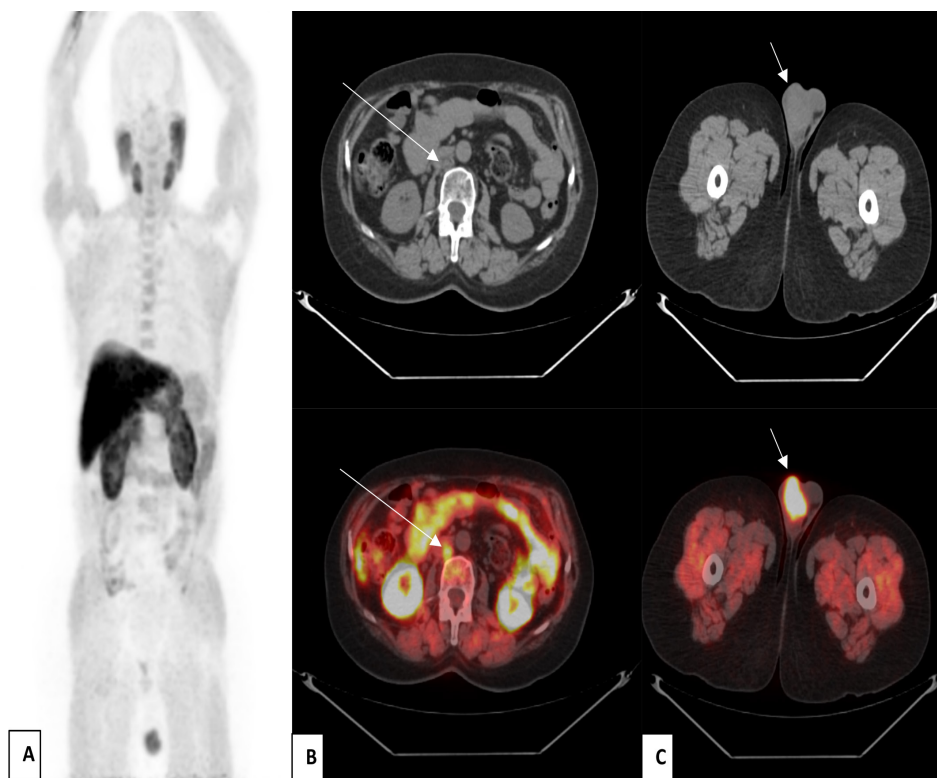


Figure 1. A 69-year-old patient was followed up since 2019 for high-risk prostatic adenocarcinoma Gleason 9 (4+5), which was treated by external radiotherapy and subsequently introduced to novel hormonotherapy. The evolution was unremarkable for 2 years. The patient was lost to follow-up for 1 year and returned in 2023 with a prostate-specific antigen level of 7.3 ng/mL. ^{18}F -choline positron emission tomography/computed tomography (PET/CT) scan was ordered as part of recurrence assessment, which showed the physiological and pathological distribution of the radiopharmaceutical (^{18}F -choline) (maximum intensity projection; A) and revealed the presence of a suspicious pathological hypermetabolic lymphadenopathy interaortic cavity [the maximum standardized uptake value (SUV_{max}) was 4.4], suggesting of lymph node recurrence (CT and fusion images in axial sections; arrow; B), besides the absence of suspicious hypermetabolism in the prostatic lodge.

In the CT and fusion images in axial sections (arrow; C), we also noted the presence of a suspicious right testicular nodule measuring 43x30 mm with an intense hypermetabolism ($\text{SUV}_{\text{max}}=8.8$). Our findings suggest two diagnoses: primary cancer or rare testicular metastasis of prostate cancer.

Rare testicular hypermetabolism requires prompt reporting by the nuclear medicine physician, prompting a follow-up testicular ultrasound, especially if CT scan shows suspicious abnormalities. Testicular ultrasonography showed two contiguous, well-limited, heterogeneous tissue nodules taking color Doppler and containing microcalcifications, measuring 23x27 mm and 19x20 mm respectively.

Few cases of testicular involvement in prostate cancer have been reported in the literature using ^{18}F -choline PET/CT. Identifying a testicular lesion in a familial neoplastic context, particularly in prostatic cases, requires careful investigation and histological confirmation to distinguish metastatic from primary origin (1).

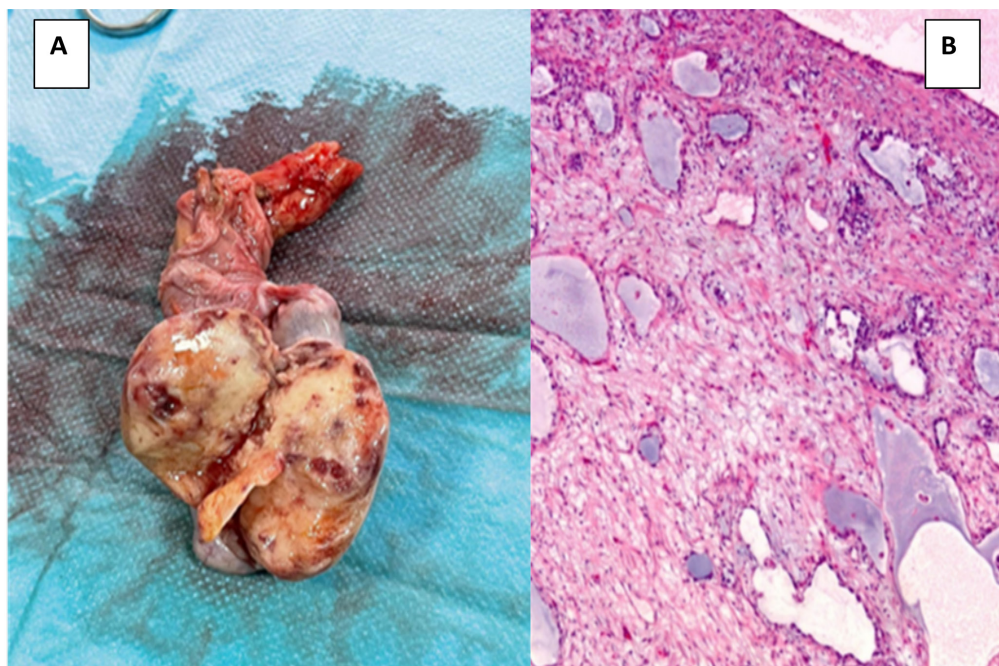


Figure 2. The patient underwent bilateral orchiectomy (bilateral orchiectomy surgical specimen; A), and the morphological and immunohistochemical profile was consistent with a testicular primary cancer (pathological section of the poorly differentiated carcinomatous testicular process; B), in particular a yolk tumor. ^{18}F -choline PET/CT allowed us to discover, in addition to lymph node recurrence, a rare and asymptomatic testicular primary cancer, which was accessible and resectable. Orchiectomy seemed essential in the absence of histological evidence that could confirm the diagnosis. The yolk tumor discovered fortuitously is an uncommon histological variant of non-seminomatous germ cell tumors in adults (2), and its binding to ^{18}F -choline remains non-specific and poorly defined. Calabrò et al. (3) reported also a case of incidental finding of testicular seminoma by ^{18}F -choline PET/CT in a prostate cancer patient. Also, Cegla et al. (4) reported that incidental detection of a second primary cancer in prostate cancer patients using ^{18}F -choline PET/CT is not very common and that lung cancer and hematologic malignancies are most frequently detected at 50% and 19% of cases, respectively, and less often a testicular cancer.

Moreover, the presence of this unusual testicular hypermetabolism poses challenges in terms of differential diagnosis, especially testicular secondary involvement, which is uncommon (2-3% prevalence) and is typically discovered during autopsy or orchidectomy. Prostate cancer nearly constitutes half of all testicular metastases, with suggested dissemination through different ducts or vascular networks, emphasizing an unconventional metastatic pathway. Foret et al. (5) reported a rare instance of isolated testicular recurrence of prostatic adenocarcinoma identified via ^{18}F -fluorocholine PET/CT. Furthermore, there are no studies in the literature addressing the various diagnoses to consider in the presence of this testicular hypermetabolism, particularly benign testicular pathologies unrelated to neoplastic contexts.

This case underscores the pivotal role of ^{18}F -choline PET/CT in the management of prostatic neoplasia, revealing a rare primary testicular cancer. It highlights the need for additional scientific studies and emphasizes the importance of systematic pathological examination post-surgical castration for improved differential diagnosis and enhanced control of prostatic neoplasia, especially after addressing lymph node recurrence. In addition, the discovery of a testicular vitelline tumor during ^{18}F -choline investigation for prostate cancer emphasizes the significance of thorough imaging and testing. It stresses the requirement for comprehensive, multidisciplinary care in addressing complex cases, urging further research to understand the implications and potential treatment strategies for these uncommon concurrent cancers.

Ethics

Informed Consent: Informed consents of the patient was obtained.

Authorship Contributions

Concept: C.B., S.O.N., M.A., O.A.S., Y.B., A.D., Design: C.B., S.O.N., O.A.S., Y.B., A.D., Data Collection or Processing: C.B., Analysis or Interpretation: C.B., S.O.N., A.D., Literature Search: C.B., M.A., Writing: C.B.

Conflict of Interest: No conflicts of interest were declared by the authors.

Financial Disclosure: The authors declare that this study has received no financial support.

References

1. Bauduceau O, Vedrine L, Chargari C, Ceccaldi B, Le Moulec S, Houlgatte A. Métastase testiculaire d'un adénocarcinome prostatique: à propos d'un cas [Testicular metastasis of prostatic adenocarcinoma: a case report]. *Prog Urol.* 2007;17:251-252. French.
2. Zizi M, Ziouziou I, El Yacoubi S, Khmou M, Jahid A, Mahassini N, Karmouni T, El Khader K, Koutani A, Andaloussi AI. Tumeur du sac vitellin du testicule au stade IIIc métastatique : à propos d'un cas. *Can Urol Assoc J.* 2014;8:E663-E665. French.
3. Calabrò A, Bosio G, Drera E, Giubbini R, Bertagna F. Incidental Finding of Testicular Seminoma by 18F-Choline PET/CT in a Prostate Cancer Patient. *Clin Nucl Med.* 2022;47:e249-e251.
4. Cegla P, Scibisz-Dziedzic K, Witkowska K, Kubiak A, Wierzoslawska E, Kycler W, Chrapko B, Czepczyński R. Detection of a second primary cancer in a 18F-fluorocholine PET/CT - multicentre retrospective analysis on a group of 1345 prostate cancer patients. *Nucl Med Rev Cent East Eur.* 2022;25:25-30.
5. Foret T, Dimier JP, Skanjeti A, Dhomps A, Tordo J. Récidive testiculaire isolée d'un adénocarcinome prostatique révélée par TEP/TDM 18F-fluorocholine [Solitary testicular metastasis from prostate adenocarcinoma revealed by ¹⁸F-fluorocholine PET/CT]. *Médecine Nucléaire.* 2020;44:76-78.



¹⁸F-FDG PET/CT Correctly Differentiates Idiopathic Pericarditis from Recurrent Lymphoma in a Patient with Primary Mediastinal Lymphoma

¹⁸F-FDG PET/CT, Primer Mediastinal Lenfomalı Bir Hastada İdiyopatik Perikarditi Tekrarlayan Lenfomadan Doğru Şekilde Ayırt Eder

© Sira Vachatimanont^{1,2}, © Chanittha Buakhao^{3,4}, © Napisa Bunnag⁵

¹King Chulalongkorn Memorial Hospital, Nuclear Medicine Unit, Bangkok, Thailand

²Chulalongkorn University Faculty of Medicine, Chulalongkorn University International Doctor of Medicine program (CU-MEDi), Bangkok, Thailand

³Phramongkutklao College of Medicine, Bangkok, Thailand

⁴Chulalongkorn University Faculty of Medicine, Department of Radiology, Nuclear Medicine Unit, Bangkok, Thailand

⁵Chulalongkorn University Faculty of Medicine, King Chulalongkorn Memorial Hospital, Department of Radiology, Diagnostic Radiology Unit, Bangkok, Thailand

Abstract

A man in his 30s awaiting end-of-treatment ¹⁸F-fluorodeoxyglucose positron emission tomography/CT (¹⁸F-FDG PET/CT) for primary mediastinal B-cell lymphoma developed chest pain and pericardial effusion. His interim ¹⁸F-FDG PET/CT showed complete metabolic responses. His blood test revealed elevated levels of inflammatory markers, including C-reactive protein of 204.1 mg/L and erythrocyte sedimentation rate of 106 mm/h. His pericardial biopsy revealed organizing fibrinous pericarditis with hemosiderin pigment deposition and no evidence of malignancy or granuloma. The ¹⁸F-FDG PET/CT performed during this episode of illness revealed a mild degree of ¹⁸F-FDG uptake along the pericardial lining [maximum standardized uptake value (SUV_{max}) =6.76] compared with the blood pool activity (SUV_{max} =3.17), which favors pericarditis over relapsed lymphoma. His symptoms subsided 2 weeks after treatment with a non-steroidal anti-inflammatory drug, and he had no sign of relapsed lymphoma on subsequent follow-ups.

Keywords: Nuclear medicine, pericarditis, non-Hodgkins lymphoma, cardiology

Öz

Primer mediastinal B hücreli lenfoma için tedavi sonu ¹⁸F-florodeoksiglukoz pozitron emisyon tomografisi/bilgisayarlı tomografi (¹⁸F-FDG PET/CT) bekleyen 30'lu yaşlarındaki bir erkek hastada göğüs ağrısı ve perikardiyal efüzyon gelişti. Ara değerlendirmedeki ¹⁸F-FDG PET/CT'si tam metabolik yanıt göstermekteydi. Kan testinde enflamatuvar belirteçlerde artışı gösterecek şekilde C-reaktif protein düzeyi 204,1 mg/L ve eritrosit sedimentasyon hızı 106 mm/saat idi. Perikard biyopsisinde hemosiderin pigment birikimi ile birlikte organize fibrinöz perikardit saptandı ve malignite veya granülom kanıtı yoktu. Hastalığın bu epizodu sırasında yapılan ¹⁸F-FDG PET/CT, lenfoma nüksüne göre perikarditi destekleyen kan havuzu aktivitesiyle [maksimum standardize tutulum değeri (SUV_{max}) =3,17] karşılaştırıldığında perikardiyal hat boyunca hafif derecede ¹⁸F-FDG tutulumunu (SUV_{max} =6,76) ortaya çıkardı; bu da nükseden lenfomaya kıyasla perikarditi düşündürür. Hastanın semptomları steroid olmayan anti-enflamatuvar ilaç tedavisinden 2 hafta sonra azaldı ve sonraki takiplerde nükseden lenfoma belirtisi görülmedi.

Anahtar kelimeler: Nükleer tıp, perikardit, non-Hodgkin lenfoma, kardiyoloji

Address for Correspondence: Sira Vachatimanont, MD, King Chulalongkorn Memorial Hospital, Nuclear Medicine Unit, Chulalongkorn University Faculty of Medicine, Chulalongkorn University International Doctor of Medicine program (CU-MEDi), Bangkok, Thailand

Phone: +022564000 **E-mail:** siravac@gmail.com **ORCID ID:** orcid.org/0000-0002-7393-2250

Received: 27.11.2023 **Accepted:** 29.02.2024 **Epub:** 15.03.2024



Copyright© 2024 The Author. Published by Galenos Publishing House on behalf of the Turkish Society of Nuclear Medicine. This is an open access article under the Creative Commons Attribution-NonCommercial-NoDerivatives 4.0 (CC BY-NC-ND) International License.

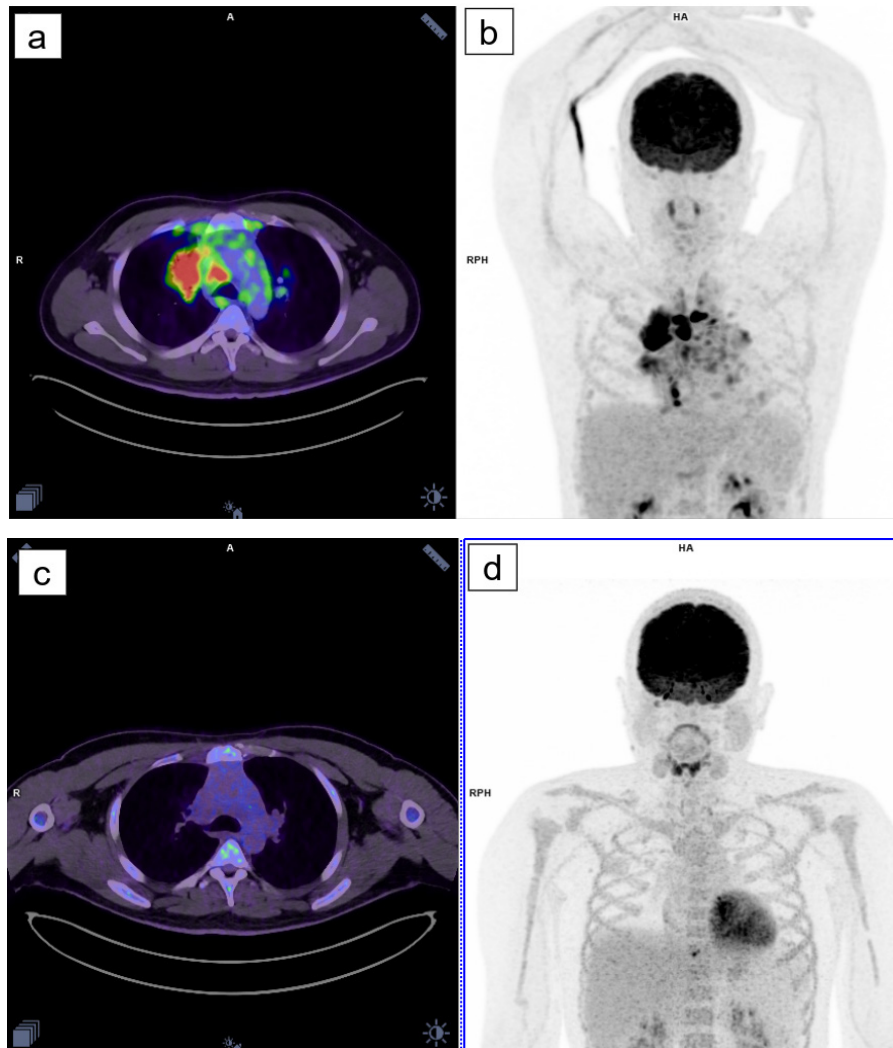


Figure 1. A man in his 30s had an underlying primary mediastinal B-cell lymphoma. The initial staging fluorine-18 fluorodeoxyglucose (¹⁸F-FDG) positron emission tomography/computed tomography (PET/CT) for his lymphoma demonstrated multiple abnormal ¹⁸F-FDG-avid lymph nodes in the mediastinum, which was consistent with lymphomatous involvement (a, b). He received chemotherapy sessions. His interim ¹⁸F-FDG PET/CT showed complete metabolic responses of the mediastinal lesions (c, d).

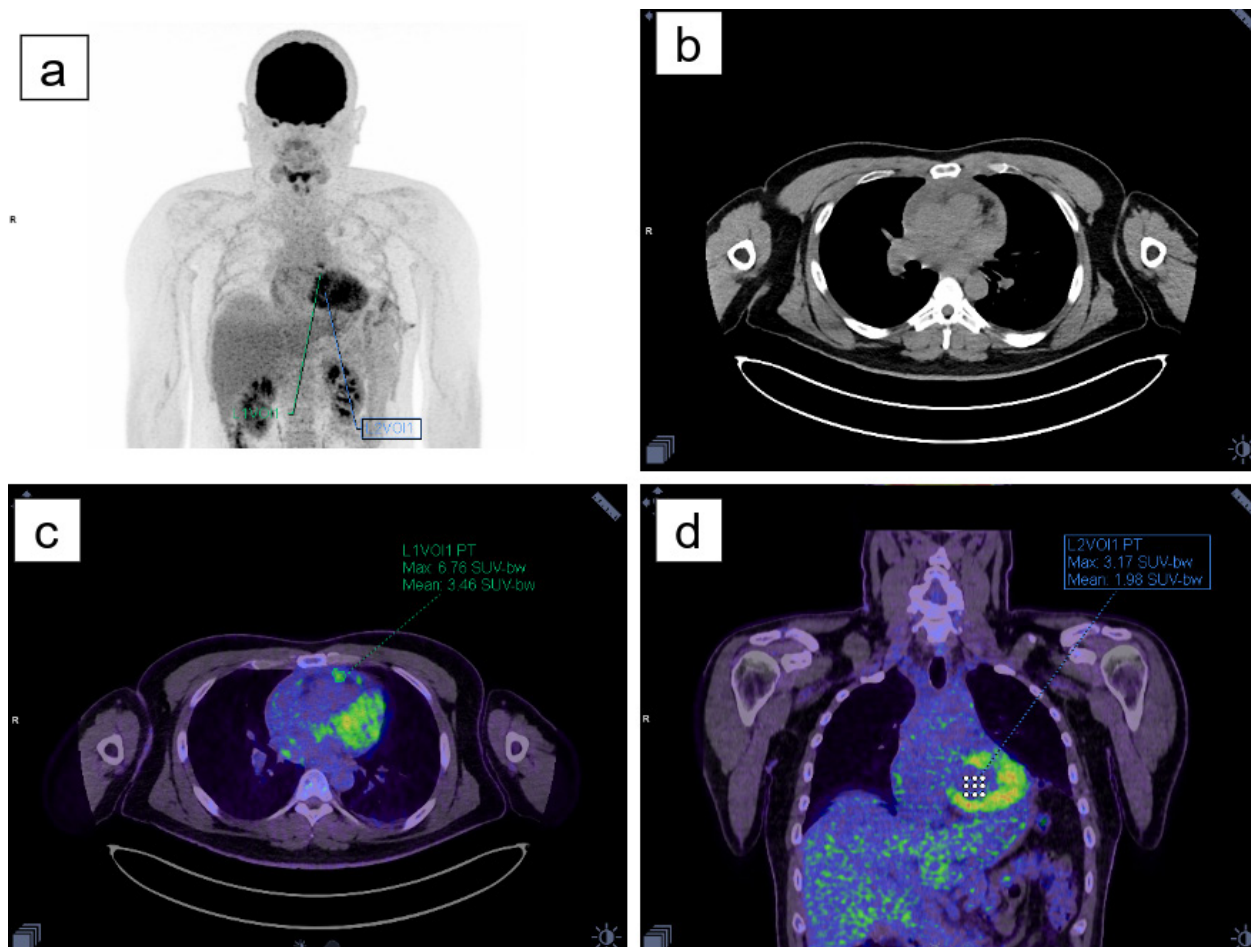


Figure 2. Approximately 1 month after the conclusion of his chemotherapy session, the patient experienced pruritic chest pain with fever and presented at the emergency department. Bedside echocardiography revealed recently developed 3 cm thick loculated pericardial effusion. A pericardial biopsy was performed, which yielded organizing fibrinous pericarditis with hemosiderin pigment deposition on pathological examination, without evidence of malignancy or granuloma. His erythrocyte sedimentation rate (ESR) was 106 mm/h and serum C-reactive protein (CRP) level was 204.1 mg/L. Follow-up ^{18}F -FDG PET/CT was performed to assess the end-of-treatment response to chemotherapy and rule out the possibility of relapsed lymphoma (a). ^{18}F -FDG PET/CT revealed the recent development of nodular ^{18}F -FDG uptake foci along the pericardial lining with a maximum standardized uptake value (SUV_{max}) of 6.76 (b, c). No other evidence of recurrent lymphoma was detected. As an internal reference, the measured SUV_{max} of the ventricular blood pool was 3.17 (d). The patient was diagnosed with acute idiopathic pericarditis and was treated with the non-steroidal anti-inflammatory drug ibuprofen. His chest pain and fever subsided approximately 2 weeks after the initiation of ibuprofen. His ESR was 15 mm/h, and his CRP was 4.35 mg/L 4 weeks after ibuprofen treatment. No ^{18}F -FDG PET/CT was performed afterward to follow up on his pericarditis.

Although ^{18}F -FDG PET/CT has not yet been established as a standard investigation for pericarditis, potential uses of ^{18}F -FDG PET/CT have been proposed for multiple pericardial diseases (1). One potential use of ^{18}F -FDG PET/CT is to differentiate between malignant and benign pericardial diseases. A study by Shao et al. (2) proposed a cut-off of $\text{SUV}_{\text{max}} \text{ lesion} / \text{SUV}_{\text{max}} \text{ blood pool}$ ratio of >2.4 to indicate malignant pericardial disease with a sensitivity of 92.3% and specificity of 90.0%. In this study, the SUV_{max} ratio was 2.13, which correctly classified the uptake as benign. Other potential uses of ^{18}F -FDG PET/CT in acute idiopathic pericarditis include predicting the risk of pericarditis relapse (3) and differentiating tuberculous from idiopathic pericarditis (4,5). Our case report supports the idea that ^{18}F -FDG PET/CT can be a reliable diagnostic tool for differentiating malignant from non-malignant pericardial diseases.

Ethics

Informed Consent: The Institutional Review Board of the Faculty of Medicine at Chulalongkorn University approved this case and waived the requirement for written informed consent based on its retrospective nature (COE No. 020/2023).

Authorship Contributions

Surgical and Medical Practices: C.B., Concept: N.B., Design: N.B., Data Collection or Processing: C.B., Analysis or Interpretation: S.V., N.B., Literature Search: S.V., N.B., Writing: S.V., N.B.

Conflict of Interest: No conflicts of interest were declared by the authors.

Financial Disclosure: The authors declare that this study has received no financial support.

References

1. Kim MS, Kim EK, Choi JY, Oh JK, Chang SA. Clinical utility of [¹⁸F]FDG-PET /CT in pericardial disease. *Curr Cardiol Rep.* 2019;21:107.
2. Shao D, Wang SX, Liang CH, Gao Q. Differentiation of malignant from benign heart and pericardial lesions using positron emission tomography and computed tomography. *J Nud Cardiol.* 2011;18:668-677.
3. Gerardin C, Mageau A, Benali K, Jouan F, Ducrocq G, Alexandra JF, van Gysel D, Papo T, Sacre K. Increased FDG-PET/CT pericardial uptake identifies acute pericarditis patients at high risk for relapse. *Int J Cardiol.* 2018;271:192-194.
4. Gouriet F, Levy PY, Casalta JP, Zandotti C, Collart F, Lepidi H, Cautela J, Bonnet JL, Thuny F, Habib G, Raoult D. Etiology of pericarditis in a prospective cohort of 1162 cases. *Am J Med.* 2015;128:784.e1-8.
5. Dong A, Dong H, Wang Y, Cheng C, Zuo C, Lu J. (¹⁸F)FDG PET/CT in differentiating acute tuberculous from idiopathic pericarditis: preliminary study. *Clin Nucl Med.* 2013;38:e160-165.



A Case of Diffuse Infiltrative Hepatocellular Carcinoma with Marked Response to Sorafenib Treatment Evidenced by ¹⁸F-FDG PET/MRI

¹⁸F-FDG PET/MRG ile Sorafenib Tedavisine Belirgin Yanıt Verdiği Gösterilen Diffüz İnfiltratif Hepatosellüler Karsinom Olgusu

Elgin Özkan¹, Burak Demir¹, Diğdem Kuru Öz², Yüksel Ürün³, Nuriye Özlem Küçük¹

¹Ankara University Faculty of Medicine, Department of Nuclear Medicine, Ankara, Türkiye

²Ankara University Faculty of Medicine, Department of Radiology, Ankara, Türkiye

³Ankara University Faculty of Medicine, Department of Internal Medicine, Division of Medical Oncology, Ankara, Türkiye

Abstract

A 73-year-old woman with known diagnosis of chronic hepatitis B infection referred for ¹⁸F-fluorodeoxyglucose positron emission tomography/computed tomography (¹⁸F-FDG PET/CT) and magnetic resonance imaging (MRI) after detection of a liver mass with 9 cm diameter in contrast enhanced CT. However, ¹⁸F-FDG PET/CT and MRI revealed diffuse infiltrating hepatocellular carcinoma lesions other than previously defined mass. After 9 months of Sorafenib treatment serum alpha fetoprotein levels dropped from 60,500 ng/mL to 801 ng/mL. Later ¹⁸F-FDG PET/MRI was performed for evaluation of response to treatment and revealed marked response to treatment.

Keywords: Hepatocellular carcinoma, positron emission tomography, fluorodeoxyglucose, magnetic resonance imaging, sorafenib

Öz

Bilinen kronik hepatit B enfeksiyonu tanılı hasta kontrastlı bilgisayarlı tomografide (BT) karaciğerde 9 cm boyutlu kitle saptanması üzerine ¹⁸F-florodeoksiglukoz pozitron emisyon tomografisi/BT (¹⁸F-FDG PET/BT) ve manyetik rezonans görüntüleme (MRG) için yönlendirildi. Ancak, ¹⁸F-FDG PET/BT ve MRG'de önceki tanımlanan kitle dışında parankimde diffüz infiltratif hepatosellüler karsinom lezyonları saptandı. Dokuz aylık sorafenib tedavisini takiben serum alfa fetoprotein değerleri 60.500 ng/mL'den 801 ng/mL'ye kadar geriledi. Tedavi yanıtı için çekilen ¹⁸F-FDG PET/MRG'de de belirgin tedavi yanıtı gösterildi.

Anahtar kelimeler: Hepatosellüler karsinom, pozitron emisyon tomografisi, florodeoksiglukoz, manyetik rezonans görüntüleme, sorafenib

Address for Correspondence: Burak Demir, MD, Ankara University Faculty of Medicine, Department of Nuclear Medicine, Ankara, Türkiye

Phone: +90 312 595 64 45 **E-mail:** 4burakfe@gmail.com **ORCID ID:** orcid.org/0000-0002-0966-9988

Received: 26.01.2024 **Accepted:** 03.03.2024 **Epub:** 16.04.2024



Copyright© 2024 The Author. Published by Galenos Publishing House on behalf of the Turkish Society of Nuclear Medicine. This is an open access article under the Creative Commons Attribution-NonCommercial-NoDerivatives 4.0 (CC BY-NC-ND) International License.

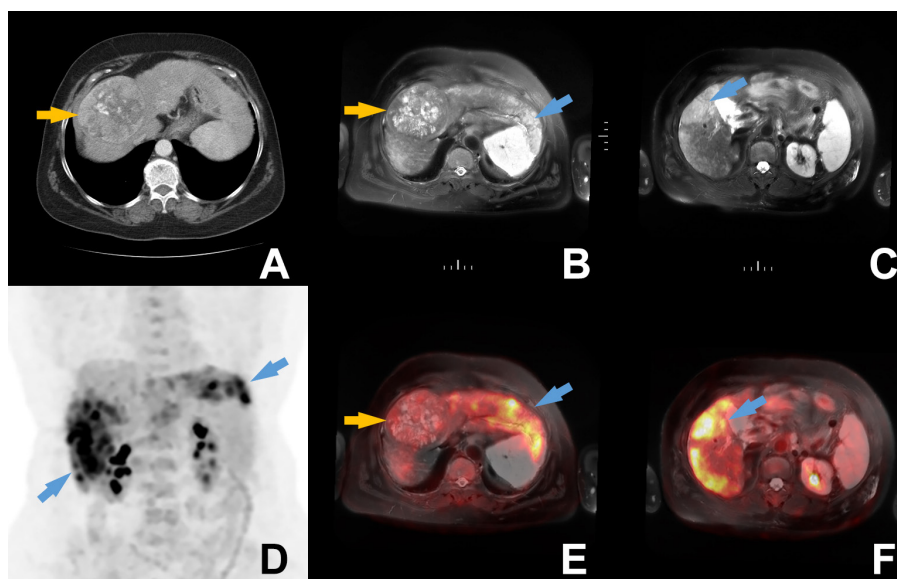


Figure 1. A 73-year-old woman with hepatitis B infection presented with abdominal pain and dynamic liver computed tomography (CT) revealed a 9 cm lesion in the liver (A, orange arrow). The patient's serum alpha feto protein (AFP) levels were measured as high as 60,500 ng/mL. The patient was referred for ^{18}F -fluorodeoxyglucose positron emission tomography/CT (^{18}F -FDG PET/CT) and magnetic resonance imaging (MRI) for staging of probable hepatocellular carcinoma (HCC) diagnosis. However, ^{18}F -FDG PET/CT and MRI revealed diffuse infiltrating HCC lesions in both lobes of liver in addition to the previously defined 9 cm mass. The diffuse infiltrating lesions (blue arrows) were hyperintense in axial T2-weighted MRI (B, C) images and showed intense ^{18}F -FDG uptake with maximum standardized uptake value (SUV_{max}): 12.5 as visualized in the maximum intensity projection (MIP) (D), axial PET/CT MRI fusion images (E, F). Additionally, the previously defined 9 cm lesion (orange arrows) had very mild ^{18}F -FDG uptake. Sorafenib treatment was initiated after the detection of advanced disease.

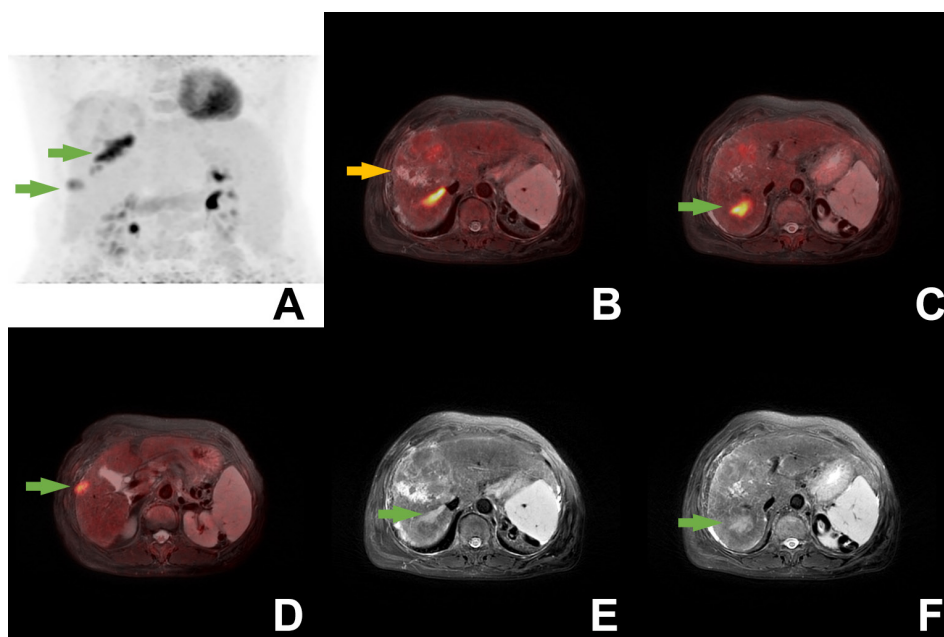


Figure 2. After 9 months of sorafenib treatment AFP levels were measured as low as 801 ng/mL. Post-treatment integrated ^{18}F -FDG PET/MRI revealed that diffuse infiltrating lesions had largely regressed. A few ^{18}F -FDG-avid lesions (green arrows) with maximum SUV_{max} : 10.9 including tumor thrombosis in right hepatic vein, could be visualized in MIP (A), axial T2-weighted MRI (E, F), axial PET/MRI fusion (B, C, D) images. There was no significant difference in MRI findings of large mass as it had a minimal decrease in diameter to 8 cm and is still mildly ^{18}F -FDG-avid (B-orange arrow).

HCC is one of the most prevalent cancers in the world (1,2). In advanced HCC cases treatment choices can be limited to systemic treatments such as tyrosine-kinase receptor inhibitors, vascular endothelial growth factor inhibitors and immunotherapy agents (3,4,5). As one of the most commonly used tyrosine-kinase inhibitors, sorafenib can increase overall survival in HCC patients (6). It has been shown that pretreatment ^{18}F -FDG PET/CT parameters have a prognostic value in HCC patients treated with sorafenib but intensity of ^{18}F -FDG uptake may not predict response to sorafenib treatment (7,8). In this case the lesions previously undetected in CT were demonstrated with both components of PET/MRI. Additionally, ^{18}F -FDG PET revealed different characteristics of these two pathologies, one being solitary non-FDG avid mass, other being intensely FDG-avid infiltrating lesions. Furthermore, more ^{18}F -FDG avid infiltrating lesions had a marked response to sorafenib while the other large solid mass was merely exhibiting stable disease. An effective response to sorafenib is rare, and in this case both PET and MRI revealed dramatic response of infiltrating lesions to treatment, consistent with clinical findings. In conclusion, PET can reveal metabolic characteristics of HCC lesions and usage of high soft tissue contrast of MRI can help identify corresponding lesions in liver. This could make the usage of PET/MRI valuable for diagnosis, staging and as demonstrated above evaluation of response to treatment.

Ethics

Informed Consent: Written informed consent was obtained from the patient.

Authorship Contributions

Surgical and Medical Practices: E.Ö., B.D., D.K.Ö., Y.Ü., N.Ö.K., Concept: E.Ö., B.D., Data Collection or Processing:

E.Ö., B.D., D.K.Ö., Y.Ü., N.Ö.K., Analysis or Interpretation: E.Ö., B.D., D.K.Ö., N.Ö.K., Literature Search: E.Ö., B.D., Writing: E.Ö., B.D.

Conflict of Interest: No conflicts of interest were declared by the authors.

Financial Disclosure: The authors declare that this study has received no financial support.

References

1. Sung H, Ferlay J, Siegel RL, Laversanne M, Soerjomataram I, Jemal A, Bray F. Global Cancer Statistics 2020: GLOBOCAN Estimates of Incidence and Mortality Worldwide for 36 Cancers in 185 Countries. *CA Cancer J Clin* 2021;71:209-249.
2. El-Serag HB, Mason AC. Rising incidence of hepatocellular carcinoma in the United States. *N Engl J Med*. 1999;340:745-750.
3. Reig M, Forner A, Rimola J, Ferrer-Fàbrega J, Burrel M, Garcia-Criado Á, Kelley RK, Galle PR, Mazzaferro V, Salem R, Sangro B, Singal AG, Vogel A, Fuster J, Ayuso C, Bruix J. BCLC strategy for prognosis prediction and treatment recommendation: The 2022 update. *J Hepatol*. 2022;76:681-693.
4. European Association For The Study Of The Liver; European Organisation For Research And Treatment Of Cancer. EASL-EORTC clinical practice guidelines: management of hepatocellular carcinoma. *J Hepatol*. 2012;56:908-943.
5. Forner A, Reig M, Bruix J. Hepatocellular carcinoma. *Lancet*. 2018;391:1301-1314.
6. Fan G, Wei X, Xu X. Is the era of sorafenib over? A review of the literature. *Ther Adv Med Oncol*. 2020;12:1758835920927602.
7. Sung PS, Park HL, Yang K, Hwang S, Song MJ, Jang JW, Choi JY, Yoon SK, Yoo IR, Bae SH. ^{18}F -fluorodeoxyglucose uptake of hepatocellular carcinoma as a prognostic predictor in patients with sorafenib treatment. *Eur J Nucl Med Mol Imaging*. 2018;45:384-391.
8. Lee JH, Park JY, Kim DY, Ahn SH, Han KH, Seo HJ, Lee JD, Choi HJ. Prognostic value of ^{18}F -FDG PET for hepatocellular carcinoma patients treated with sorafenib. *Liver Int*. 2011;31:1144-1149.



Distinguishing Bronchial Carcinoid from Benign Bronchocele using ^{68}Ga -DOTATOC PET/CT Imaging

^{68}Ga -DOTATOC PET/BT Görüntüleme Kullanılarak Bronşiyal Karsinoidin Benign Bronkoselden Ayırılması

✉ Akram Al-Ibraheem¹, ✉ Raghad Alhouwari¹, ✉ Baraa Alsyouf², ✉ Ahmed Saad Abdlkadir¹, ✉ Hussam Haddad³

¹King Hussein Cancer Center (KHCC), Department of Nuclear Medicine and PET/CT, Amman, Jordan

²University of Jordan, Department of Radiology and Nuclear Medicine, Division of Nuclear Medicine, Amman, Jordan

³King Hussein Cancer Center (KHCC), Department of Pathology, Amman, Jordan

Abstract

Bronchial carcinoids are low-grade neuroendocrine tumors with slow growth rates and the potential to spread to nearby lymph nodes. Here we present a challenging case of bronchial carcinoid visualized alongside an adjacent benign bronchocele. Chest computed tomography (CT) identified the endobronchial mass with unclear morphological and diagnostic insights. A differential diagnosis of several benign and malignant etiologies was made. Subsequently, an endobronchial biopsy confirmed lung carcinoid. For better evaluation, a ^{68}Ga -labeled 1,4,7,10-tetraazacyclododecane-N,N',N'',N'''-tetraacetic acid-d-Phe1-Tyr3-octreotide (^{68}Ga -DOTATOC) positron emission tomography/CT scan was performed. The scan revealed a locally confined endobronchial mass with intense ^{68}Ga -DOTATOC expression. Adjacent benign bronchocele was visualized with insignificant ^{68}Ga -DOTATOC expression. Histopathological examination of the resected upper lobe confirmed these findings. This case highlights the importance of somatostatin receptor imaging in accurately identifying the extent of carcinoid tumors in the primary, nodal, and metastatic domains.

Keywords: Bronchocele, bronchial carcinoid, diagnostic challenge, ^{68}Ga -DOTATOC, somatostatin receptor imaging, PET/CT

Öz

Bronşiyal karsinoidler, yavaş büyüme oranlarına sahip ve yakındaki lenf düğümlerine yayılma potansiyeli olan düşük dereceli nöroendokrin tümörlerdir. Burada komşu benign bronkoselin yanında görüntülenen zorlu bir bronşiyal karsinoid olgusu sunulmaktadır. Bilgisayarlı toraks tomografisi (BT), belirsiz morfolojik ve tanısal bilgilerle endobronşiyal kitleyi tanımladı. Çeşitli benign ve malign etiyolojilerin ayırıcı tanısı yapıldı. Daha sonra endobronşiyal biyopsi akciğer karsinoidini doğruladı. Daha iyi değerlendirme için, ^{68}Ga etiketli 1,4,7,10-tetraazasiklododekan-N,N',N'',N'''-tetraasetik asit-d-Phe1-Tyr3-oktreotid (^{68}Ga -DOTATOC) pozitron emisyon tomografisi/BT taraması yapıldı. Tarama, yoğun ^{68}Ga -DOTATOC ekspresyonuna sahip lokal olarak sınırlı bir endobronşiyal kitleyi ortaya çıkardı. Komşu benign bronkosel, önemsiz ^{68}Ga -DOTATOC ekspresyonuyla görüntüldü. Rezeke edilen üst lobun histopatolojik incelemesi bu bulguları doğruladı. Bu olgu, primer, nodal ve metastatik alanlardaki karsinoid tümörlerin boyutunun doğru bir şekilde belirlenmesinde somatostatin reseptörü görüntülemesinin önemini vurgulamaktadır.

Anahtar kelimeler: Bronkosel, bronşiyal karsinoid, tanısal zorluk, ^{68}Ga -DOTATOC, somatostatin reseptörü görüntülemesi, PET/BT

Address for Correspondence: Akram Al-Ibraheem MD, King Hussein Cancer Center (KHCC), Department of Nuclear Medicine and PET/CT, Amman, Jordan

Phone: +96265300460 **E-mail:** akramalibrahim@gmail.com ORCID ID: orcid.org/0000-0002-0978-4716

Received: 17.02.2024 **Accepted:** 10.03.2024 **Epub:** 06.06.2024



Copyright© 2024 The Author. Published by Galenos Publishing House on behalf of the Turkish Society of Nuclear Medicine. This is an open access article under the Creative Commons Attribution-NonCommercial-NoDerivatives 4.0 (CC BY-NC-ND) International License.

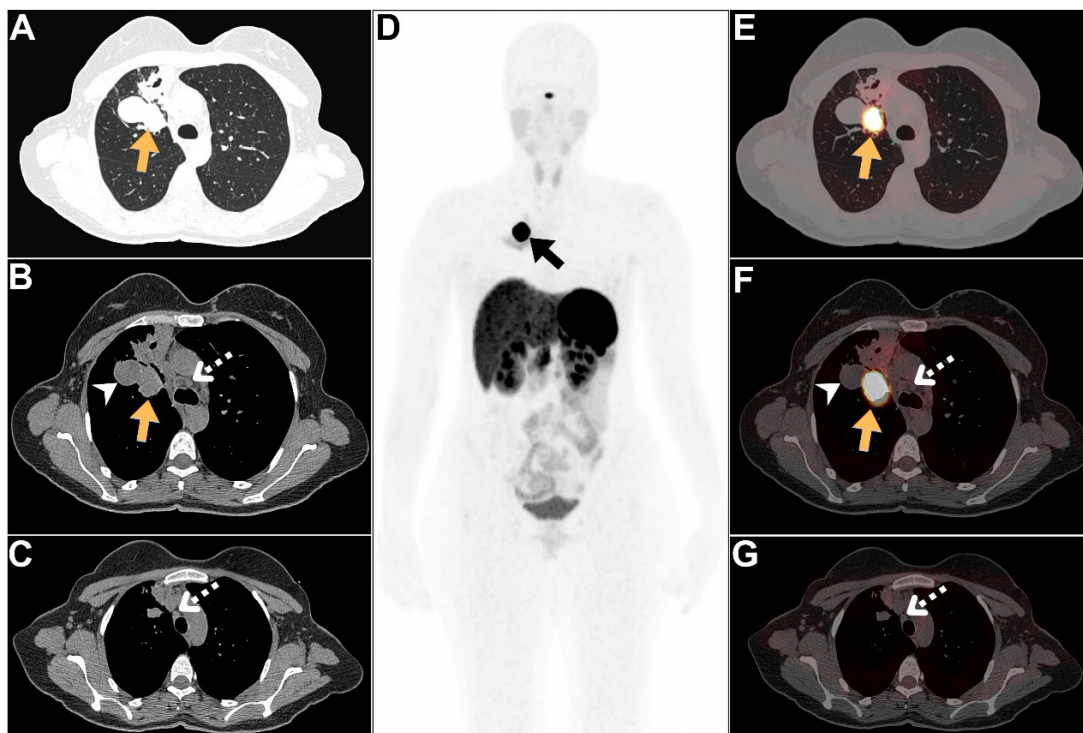


Figure 1. A 36-year-old female presented with progressive, productive cough over the last 2 months. Upon consultation, the patient denies any previous history of medical diseases or surgical operations but reports a positive family history of cancer. Chest computed tomography (CT) revealed a large right peribronchial mass lesion (A, B; arrows), an adjacent cystic density (B, arrowhead), and few prominent mediastinal lymph nodes (B, C, dotted arrows). The differential diagnosis includes endobronchial obstructing tumor, atypical pneumonia, or granulomatous disease. Therefore, an endobronchial biopsy was performed for a definitive diagnosis and revealed evidence of lung carcinoid. Shortly thereafter, the patient was transferred to our cancer center for further examination. For optimal staging prior to surgical intervention, a whole-body ^{68}Ga -labeled 1,4,7,10-tetraazacyclododecane-N,N',N'',N'''-tetraacetic acid-d-Phe1-Tyr3-octreotide (^{68}Ga -DOTATOC) tumor, nodal, metastatic domains (TNM) scan was ordered. The scan identified the right endobronchial mass with intense somatostatin receptor (SSTR) expression (D, E, F, arrows). The maximum standardized uptake value was 89.2 (D, E, F, arrows). In addition, the adjacent cystic density demonstrated insignificant SSTR expression, indicating a benign etiology and confirming post-obstructive bronchocele (F, arrowhead). Moreover, few mediastinal lymph nodes with insignificant ^{68}Ga -DOTATOC avidity were concluded to be mostly benign in nature (F, G; dotted arrows). Following a multidisciplinary clinic meeting, the patient underwent a right upper lobectomy with mediastinal lymphadenectomy, which revealed a locally confined 2.5 cm typical carcinoid tumor. The tumor, nodal, and metastatic domains (TNM) staging was found to be T1cN0 and was labeled as stage IA disease. The patient is doing well after surgery and will undergo the necessary follow-up after that.

Bronchial carcinoids constitute 2% of all pulmonary malignancies (1). These tumors display various clinical, morphological, and biological patterns (1). Bronchial carcinoids may exhibit concurrent bronchocele in proximity (2). Bronchoceles, also termed bronchial mucocele, are typically benign but may masquerade as part of the primary tumor, leading to disease upstaging (2). CT evaluation alone may complicate precise tumor size determination due to density similarities and proximity (3). Occasionally, cystic malignancies were incorrectly identified by CT as mucocele or bronchocele (4,5). In such scenarios, SSTR imaging aids in accurate disease diagnosis. This unique case highlights the first instance in which ^{68}Ga -DOTATOC PET/CT discriminated a bronchial carcinoid tumor from a subsequent bronchocele. These findings underscore the important role of SSTR imaging in distinguishing benign bronchocele from endobronchial carcinoid, ensuring precise staging across TNM.

Ethics

Informed Consent: Informed consent was obtained from the patient.

Authorship Contributions

Surgical and Medical Practices: A.A.-I., R.A., B.A., A.S.A., H.H., Concept: A.A.-I., R.A., B.A., A.S.A., Design: A.A.-I., R.A., B.A., Data Collection or Processing: A.A.-I., R.A., B.A., H.H., Analysis or Interpretation: A.A.-I., A.S.A., H.H., Literature Search: R.A., A.S.A., Writing: A.A.-I., A.S.A.

Conflict of Interest: No conflicts of interest were declared by the authors.

Financial Disclosure: The authors declare that this study has received no financial support.

References

1. Araujo-Castro M, Pascual-Corrales E, Molina-Cerrillo J, Moreno Mata N, Alonso-Gordoa T. Bronchial Carcinoids: From Molecular Background to Treatment Approach. *Cancers (Basel)*. 2022;14:520.
2. Kakarla B. Bronchocele, a common but underrecognized condition: a systematic review. *Monaldi Arch Chest Dis*. 2022;93.
3. Yadav V, Rathi V. Bronchial carcinoid with bronchocele masquerading as Scimitar syndrome on chest radiograph. *Radiol Case Rep*. 2021;16:710-713.
4. Sandhu FA, Martuza RL. Craniofacial hemangiopericytoma associated with oncogenic osteomalacia: case report. *J Neurooncol*. 2000;46:241-247.
5. Shikhare SN. Imaging of Thoracic Malignancies. *Thoracic Imaging*. 2019:101-146.



Paget's Disease Mimicking Prostate Cancer Metastasis with ⁶⁸Ga-PSMA PET/CT

⁶⁸Ga-PSMA PET/BT'de Prostat Kanseri Metastazını Taklit Eden Paget Hastalığı

✉ Melis Oflas, ✉ Emine Gökür Işık, ✉ Zeynep Gözde Özkan, ✉ Duygu Has Şimşek, ✉ Yasemin Şanlı

Istanbul University, Istanbul Faculty of Medicine, Department of Nuclear Medicine, İstanbul, Türkiye

Abstract

⁶⁸Ga-prostate-specific membrane antigen (PSMA) positron emission tomography/computed tomography imaging successfully detects bone metastases in prostate cancer (PCa). However, assuming that all detected PSMA-avid bone lesions are metastases should be avoided. It is essential to evaluate PCa patients with clinical findings and to consider possible differential diagnoses, especially in low-risk patients. Herein, we present the case of a 62-year-old male patient recently diagnosed with low-risk prostate adenocarcinoma with a PSMA-avid bone lesion corresponding to Paget's disease.

Keywords: PET/CT, Paget's disease of bone, prostate cancer

Öz

⁶⁸Ga-prostat-spesifik membran antijeni (PSMA) pozitron emisyon tomografisi/bilgisayarlı tomografi görüntüleme; prostat kanserinde (PCa) kemik metastazlarını başarılı bir şekilde tespit eder. Ancak, PSMA tutulumu gösteren kemik lezyonlarının tamamının metastaz olarak değerlendirilmesinden kaçınılmalıdır. Özellikle düşük riskli PCa hastalarının klinik bulguları ile birlikte değerlendirilmesi ve muhtemel ayırıcı tanılar göz önünde bulundurulması gerekmektedir. Bu yazıda, yakın zamanda düşük riskli prostat adenokarsinomu tanısı alan ve Paget hastalığı ile uyumlu olarak değerlendirilen PSMA tutulumu gösteren kemik lezyonu bulunan 62 yaşında bir erkek hasta sunulmuştur.

Anahtar kelimeler: PET/BT, kemiğin Paget hastalığı, prostat kanseri

Address for Correspondence: Melis Oflas MD, İstanbul University, İstanbul Faculty of Medicine, Department of Nuclear Medicine, İstanbul, Türkiye

Phone: +90 212 414 20 00 - 31392 **E-mail:** melisoflas240@gmail.com ORCID ID: orcid.org/0000-0001-9796-3302

Received: 07.09.2023 **Accepted:** 25.03.2024 **Epub:** 06.06.2024



Copyright© 2024 The Author. Published by Galenos Publishing House on behalf of the Turkish Society of Nuclear Medicine. This is an open access article under the Creative Commons Attribution-NonCommercial-NoDerivatives 4.0 (CC BY-NC-ND) International License.

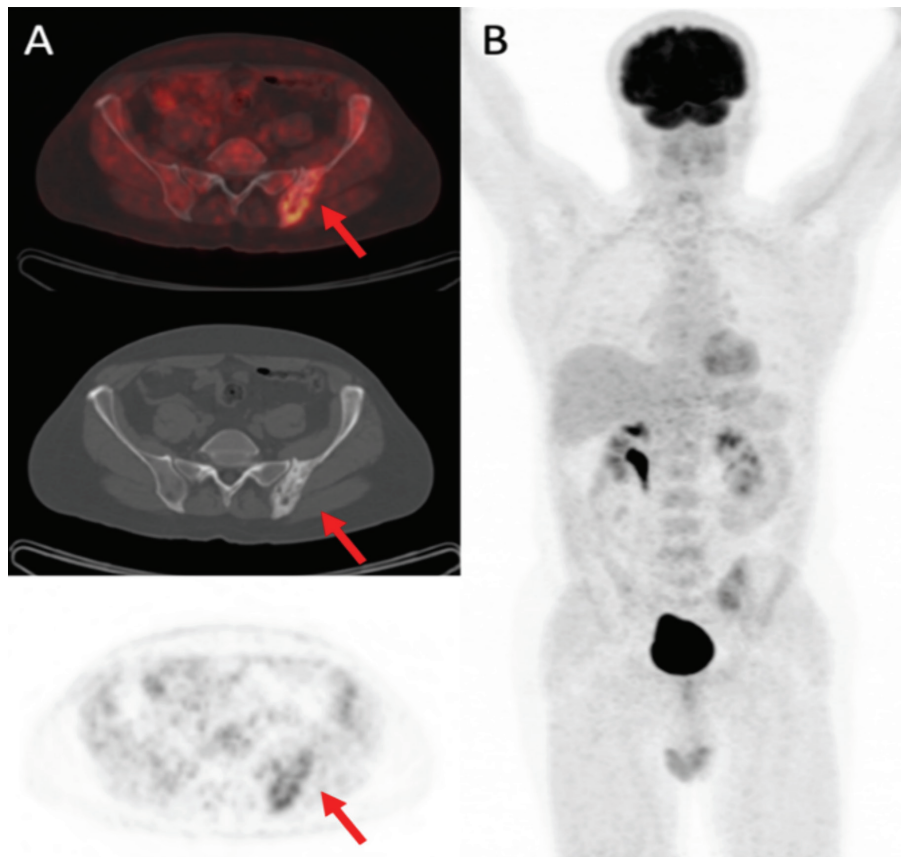


Figure 1. A 62-year-old male patient with bone pain in the left pelvic region underwent ^{18}F -fluorodeoxyglucose (^{18}F -FDG) positron emission tomography/computed tomography (PET/CT) for malignancy screening after detecting a lesion in the left iliac bone with CT. On axial ^{18}F -FDG PET/CT images (A), an FDG-avid lesion with sclerotic areas was detected [maximum standardized uptake value (SUV_{max}): 6.3]. No other findings were suspicious for FDG-avid primary tumor or metastases (B).

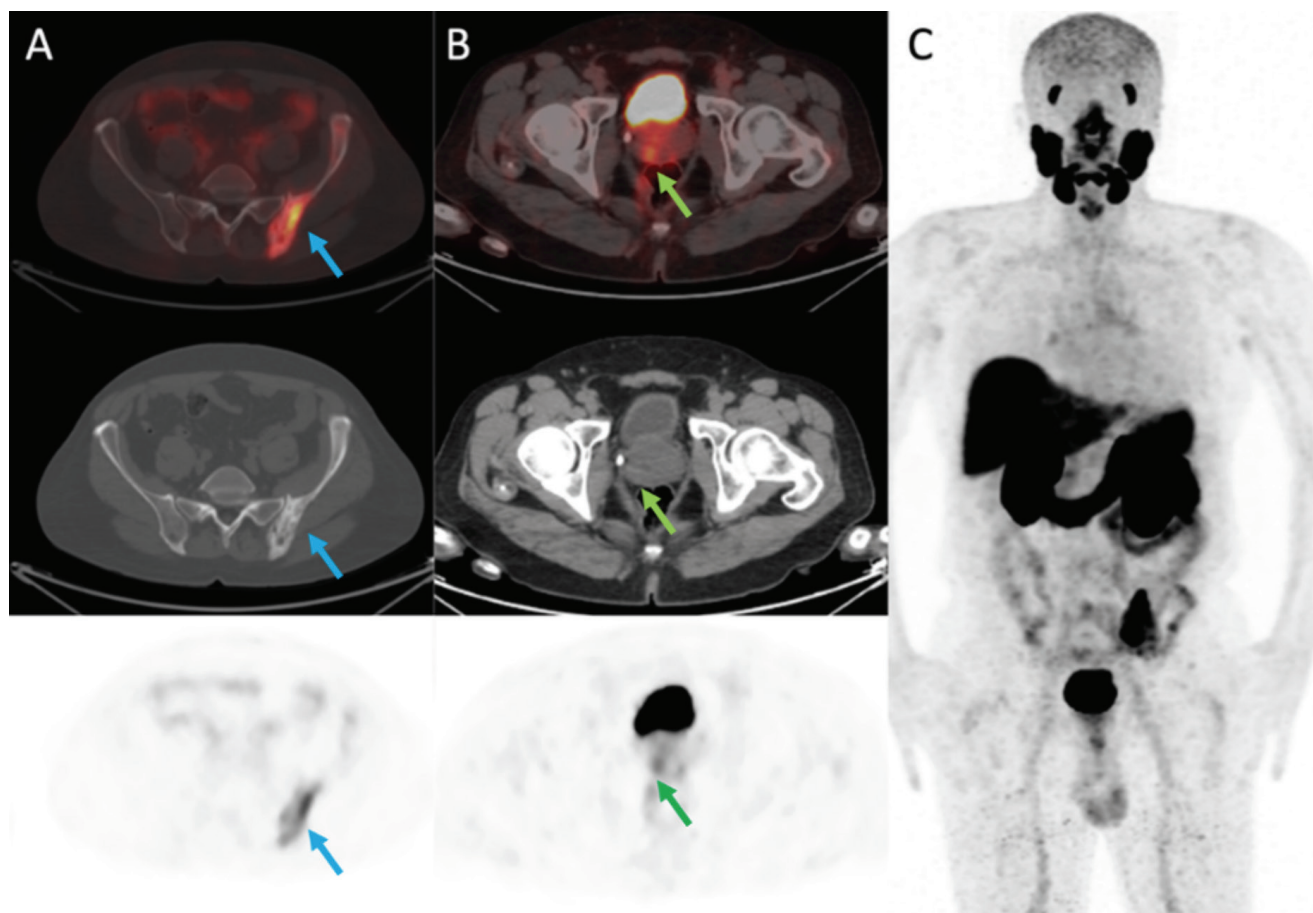


Figure 2. Subsequently, the patient was diagnosed with prostate cancer (PCa) [Gleason score: 3+3=6, ISUP grade 1; initial prostate-specific antigen (PSA) 2.54 ng/mL] after nodule detection at the urology consultation. Thus, 2 months after ^{18}F -FDG PET/CT, he underwent ^{68}Ga -PSMA PET/CT for disease staging considering the previous ^{18}F -FDG PET/CT and a slightly elevated bone alkaline phosphatase level of 23.6 mg/L (1,2). In ^{68}Ga -PSMA PET/CT images, intense PSMA expression was observed in the left iliac bone lesion (SUV_{max} : 17.85). However, CT images appeared Paget-like, such as cortical thickening and sclerosis (A, arrows). Meanwhile, no other finding could be detected in ^{68}Ga -PSMA PET/CT images, rather than a faint heterogeneous PSMA expression in the prostate gland (B, arrows; C).

In PCa staging, bone metastases are uncommon at low total PSA levels. The lesion in the left iliac bone was interpreted as Paget's disease, and he was referred to an internal medicine specialist (3,4,5,6). Paget's disease is a benign bone pathology demonstrated by abnormal bone remodeling; the pelvis, spine, femur, tibia, and skull are the main affected body parts. The main symptom of Paget's disease is bone pain due to high bone turnover, which can be relieved by bisphosphonate (7). The patient belonged to a lower-risk PCa group; therefore, the clinician opted for active surveillance (AS). Six months later, the patient had a total PSA level of 1.87 ng/mL without any treatment. Major urology guidelines suggest that patients with PCa with ISUP grade 1 having a low clinical stage and low total PSA values should be considered for AS (8). Consequently, it is essential to evaluate the data obtained from ^{68}Ga -PSMA PET/CT images with the patient's clinical presentation and consider the possible benign pathologies that can be mistaken for malignancy.

Ethics

Informed Consent: Patient consent was obtained.

Authorship Contributions

Surgical and Medical Practices: M.O., E.G.I., Z.G.Ö., D.H.Ş., Y.Ş., Concept: M.O., E.G.I., Y.Ş., Design: M.O., E.G.I., D.H.Ş., Y.Ş., Data Collection or Processing: M.O., Analysis or Interpretation: M.O., Z.G.Ö., D.H.Ş., Literature Search: M.O., Writing: M.O., Z.G.Ö.

Conflict of Interest: No conflicts of interest were declared by the authors.

Financial Disclosure: The authors declare that this study has received no financial support.

References

1. Simsek DH, Sanli Y, Civan C, Engin MN, Isik EG, Ozkan ZG, Kuyumcu S. Does bone scintigraphy still have a role in the era of 68 Ga-PSMA PET/CT in prostate cancer? *Ann Nucl Med.* 2020;34:476-485.
2. Pomykala KL, Czernin J, Grogan TR, Armstrong WR, Williams J, Calais J. Total-Body 68Ga-PSMA-11 PET/CT for Bone Metastasis Detection in Prostate Cancer Patients: Potential Impact on Bone Scan Guidelines. *J Nucl Med.* 2020;61:405-411.
3. Bourgeois S, Gykiere P, Goethals L, Everaert H, De Geeter FW. Aspecific Uptake of 68Ga-PSMA in Paget Disease of the Bone. *Clin Nucl Med.* 2016;41:877-878.
4. Sasikumar A, Joy A, Nanabala R, Pillai MR, T A H. 68Ga-PSMA PET/CT False-Positive Tracer Uptake in Paget Disease. *Clin Nucl Med.* 2016;41:e454-e455.
5. de Galiza Barbosa F, Queiroz MA, Nunes RF, Costa LB, Zaniboni EC, Marin JFG, Cerri GG, Buchpiguel CA. Nonprostatic diseases on PSMA PET imaging: a spectrum of benign and malignant findings. *Cancer Imaging.* 2020;20:23.
6. Malik D, Kumar R, Mittal BR, Singh H, Bhattacharya A, Singh SK. 68Ga-Labeled PSMA Uptake in Nonprostatic Malignancies: Has the Time Come to Remove "PS" From PSMA? *Clin Nucl Med.* 2018;43:529-532.
7. Ralston SH, Corral-Gudino L, Cooper C, Francis RM, Fraser WD, Gennari L, Guañabens N, Javaid MK, Layfield R, O'Neill TW, Russell RGG, Stone MD, Simpson K, Wilkinson D, Wills R, Zillikens MC, Tuck SP. Diagnosis and Management of Paget's Disease of Bone in Adults: A Clinical Guideline. *J Bone Miner Res.* 2019;34:579-604.
8. Willemse PM, Davis NF, Grivas N, Zattoni F, Lardas M, Briers E, Cumberbatch MG, De Santis M, Dell'Oglio P, Donaldson JF, Fossati N, Gandaglia G, Gillessen S, Grummet JP, Henry AM, Liew M, MacLennan S, Mason MD, Moris L, Plass K, O'Hanlon S, Omar MI, Oprea-Lager DE, Pang KH, Paterson CC, Ploussard G, Rouvière O, Schoots IG, Tilki D, van den Bergh RCN, Van den Broeck T, van der Kwast TH, van der Poel HG, Wiegel T, Yuan CY, Cornford P, Mottet N, Lam TBL. Systematic Review of Active Surveillance for Clinically Localised Prostate Cancer to Develop Recommendations Regarding Inclusion of Intermediate-risk Disease, Biopsy Characteristics at Inclusion and Monitoring, and Surveillance Repeat Biopsy Strategy. *Eur Urol.* 2022;81:337-346.



Bone Marrow Necrosis with Underlying Skeletal Lymphoma Evaluated by ¹⁸F-FDG PET/CT and MRI

¹⁸F-FDG PET/BT ve MRG ile Saptanan Altta Yatan İskelet Lenfomasına Bağlı Kemik İliği Nekrozu

Le Song*, Hui Li*, Weifang Zhang

Peking University Third Hospital, Departments of Nuclear Medicine, Beijing, China

*Contributed equally to this work as co-first authors.

Abstract

Bone marrow necrosis (BMN) is usually associated with malignancies and is characterized by multiple geographic signal abnormalities on magnetic resonance imaging (MRI). We report a 28-year-old female with BMN and underlying diffuse large B-cell lymphoma. Diffuse abnormal signal intensities through the vertebral column were demonstrated on her pretreatment MRI, and the diagnosis of BMN was challenging. Positron emission tomography/computed tomography (PET/CT) for lymphoma staging showed multiple decreased or absent ¹⁸F-fluorodeoxyglucose (¹⁸F-FDG) uptake within the vertebrae and pelvis. Marrow biopsy pathological examination showed lymphoma infiltration and massive necrosis. On the follow-up MRI obtained approximately 21 months after the PET/CT scan, multiple geographic abnormal signal intensities were detected within the vertebral column and were consistent with the areas of decreased ¹⁸F-FDG uptake on PET/CT. This case indicates that ¹⁸F-FDG PET/CT is helpful in the diagnosis of BMN with atypical MRI appearances.

Keywords: Bone marrow necrosis, lymphoma, ¹⁸F-FDG PET/CT, MRI

Öz

Kemik iliği nekrozu (KİN) genellikle malignitelerle ilişkilidir ve manyetik rezonans görüntüleme (MRG) çoklu bölgelerde sinyal anormallikleri ile karakterizedir. KİN'li ve altta yatan yaygın büyük B-hücreli lenfomalı 28 yaşında bir kadın hasta sunulmaktadır. Tedavi öncesi MRG'de vertebral kolon boyunca yaygın anormal sinyal yoğunlukları gösterildi ve KİN tanısını koymak güçleşti. Lenfoma evrelemesi için yapılan pozitron emisyon tomografisi/bilgisayarlı tomografi (PET/BT), omurlarda ve pelviste birden fazla ¹⁸F-florodeoksiglikoz (¹⁸F-FDG) alımının azaldığı veya olmadığı bölgeleri gösterdi. Kemik iliği biyopsisinin patolojik incelemesinde lenfoma infiltrasyonu ve masif nekroz görüldü. PET/BT taramasından yaklaşık 21 ay sonra elde edilen takip MRG'de vertebral kolonda çok sayıda bölgede anormal sinyal yoğunluğu tespit edildi ve PET/BT'de ¹⁸F-FDG alımının azaldığı alanlarla uyumluydu. Bu olgu, ¹⁸F-FDG PET/BT'nin atipik MRG görünümü olan KİN'nin tanısında yardımcı olduğunu göstermektedir.

Anahtar kelimeler: Kemik iliği nekrozu, lenfoma, ¹⁸F-FDG PET/BT, MRG

Address for Correspondence: Prof. Weifang Zhang, MD, Peking University Third Hospital, Departments of Nuclear Medicine, Beijing, China

Phone: +15611963920 **E-mail:** tsy1997@126.com **ORCID ID:** orcid.org/0000-0003-3879-1285

Received: 29.02.2024 **Accepted:** 25.03.2024 **Epub:** 06.06.2024



Copyright© 2024 The Author. Published by Galenos Publishing House on behalf of the Turkish Society of Nuclear Medicine. This is an open access article under the Creative Commons Attribution-NonCommercial-NoDerivatives 4.0 (CC BY-NC-ND) International License.

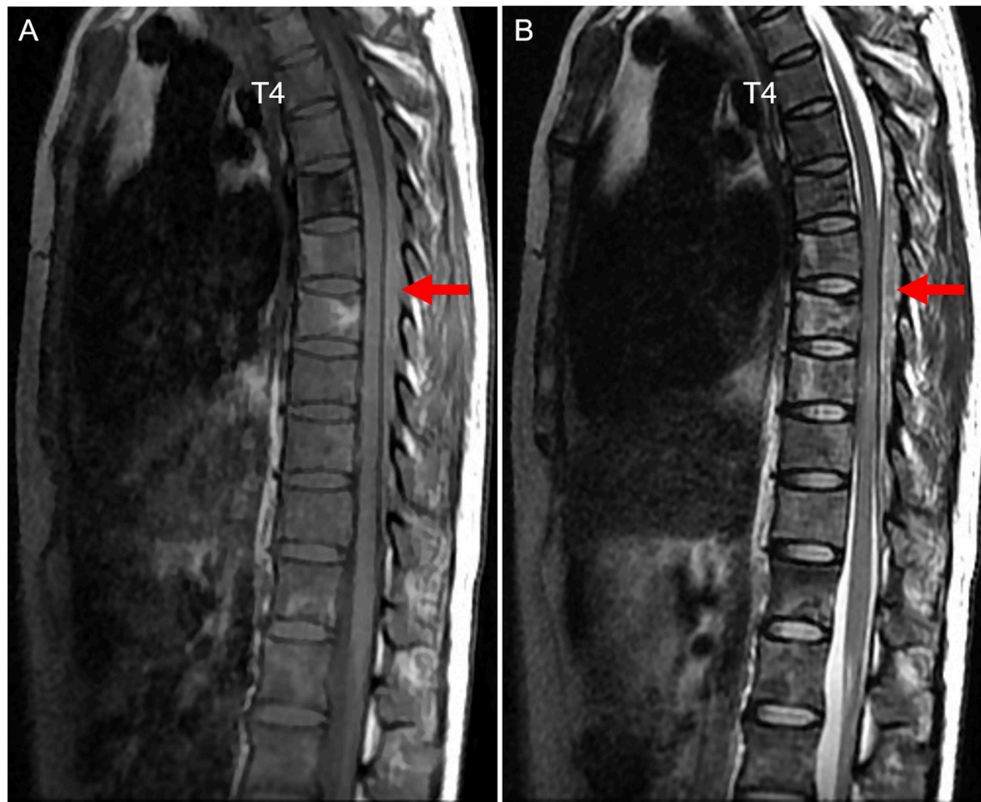


Figure 1. A 28-year-old woman with a history of back pain for 5 months complained of pain aggravation, weakness in her legs, and dysuria for 2 weeks. She underwent a thoracic spine magnetic resonance imaging (MRI) scan. T1-weighted (A) and T2-weighted (B) images showing an epidural mass compressing the spinal cord (red arrows) and diffuse abnormal signal intensity through the vertebral column. The patient underwent surgical resection of the epidural lesion 5 days after the MRI scan, and diffuse large B-cell lymphoma was confirmed by postoperative histological examination. Nine days after the operation, she underwent an ^{18}F -fluorodeoxyglucose (^{18}F -FDG) positron emission tomography/computed tomography (PET/CT) scan for further evaluation.

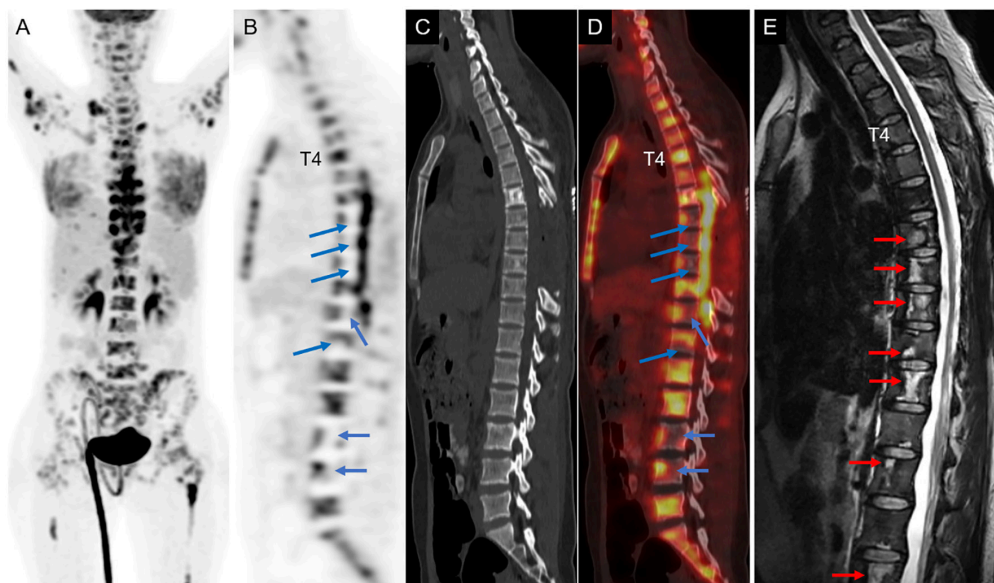


Figure 2. PET/CT images (A, maximum intensity projection; B, PET; C, CT; D, PET/CT) demonstrated diffuse lesions with increased ^{18}F -FDG uptake involving the skeleton, lymph nodes, bilateral breasts, liver, vertebral canal, etc. Multiple radioactive defects were also detected within the spine (blue arrows in B, D) and pelvis, whereas the corresponding CT scan did not show any obvious abnormality. The day after the PET/CT scan, bone marrow aspiration on the bilateral posterior iliac crest was performed, and dry taps were obtained. Marrow biopsy pathological examination showed lymphoma infiltration and massive necrosis. She underwent chemotherapy and autologous stem cell transplantation, achieved a complete response, and has remained relapse-free. On the T2-weighted MRIs (E) obtained approximately 21 months after the PET/CT scan, multiple geographic abnormal (central high with peripheral low) signal intensities were detected within the vertebral column (red arrows) and were consistent with the areas of decreased ^{18}F -FDG uptake on PET/CT. Bone marrow necrosis (BMN) was considered according to marrow pathology and MRI findings and was assumed to be secondary to the marrow involvement of lymphoma.

BMN is caused by microcirculation failure (1) and is characterized as necrosis of myeloid tissue and medullary stroma. BMN is usually associated with malignancies and mainly involves the spine and pelvis (1). It can lead to bone pain, fever, and fatigue (2). Sulfur colloid marrow scan was once thought to be useful in the diagnosis and assessment of the extent of BMN (3,4,5). Later, BMN was more commonly evaluated by MRI with its characteristic geographic signal abnormalities: central hyperintensity without enhancement surrounded by a peripheral band of hypointense signal (6,7). However, the diagnosis of BMN may be challenging based on MRI because MRI appearances may vary at different stages of BMN and may be influenced by the underlying marrow composition. As shown in this study, typical geographic signal abnormalities were not obvious on preoperative MRI. However, BMN should be suspected based on PET/CT findings of decreased or absent ^{18}F -FDG uptake in multiple vertebrae (8). The case indicates that PET/CT is complementary to MRI in the early diagnosis of BMN.

Ethics

Informed Consent: The written informed consent has been obtained from the patient.

Authorship Contributions

Surgical and Medical Practices: L.S., Concept: W.Z., Design: W.Z., Data Collection or Processing: L.S., H.L., Analysis or Interpretation: L.S., W.Z., Literature Search: L.S., H.L., Writing: L.S.

Conflict of Interest: No conflicts of interest were declared by the authors.

Financial Disclosure: The authors declare that this study has received no financial support.

References

1. Janssens AM, Offner FC, Van Hove WZ. Bone marrow necrosis. *Cancer*. 2000;88:1769-1780.

- Murphy PT, Sivakumaran M, Casey MC, Liddicoat A, Wood JK. Lymphoma associated bone marrow necrosis with raised anticardiolipin antibody. *J Clin Pathol*. 1998;51:407-409.
- Carlsson H, Winslow D, Kastan L, Yam LT. Bone marrow necrosis. Diagnosis and assessment of extent of involvement by radioisotope studies. *Arch Intern Med*. 1977;137:863-866.
- Navari RM, Carter J, Hillman RS. Bone marrow necrosis in acute leukemia. *Acta Haematol*. 1983;69:158-163.
- Cowan JD, Rubin RN, Kies MS, Cerezo L. Bone marrow necrosis. *Cancer*. 1980;46:2168-2171.
- Weissman DE, Negendank WG, al-Katib AM, Smith MR. Bone marrow necrosis in lymphoma studied by magnetic resonance imaging. *Am J Hematol*. 1992;40:42-46.
- Tang YM, Jeavons S, Stuckey S, Middleton H, Gill D. MRI features of bone marrow necrosis. *AJR Am J Roentgenol*. 2007;188:509-514.
- Dong P, Tian R, Li L, Su M. Bone marrow necrosis secondary to metastatic adenocarcinoma revealed by ^{18}F -FDG PET/CT: A clinical case report. *Medicine (Baltimore)*. 2017;96:e9067.



Multiple Bone Involvement in Low-grade Myofibroblastic Sarcoma Demonstrated on ¹⁸F-FDG PET/CT

Düşük Dereceli Miyofibroblastik Sarkomda ¹⁸F-FDG PET/CT'de Gösterilen Çoklu Kemik Tutulumu

© Hui Li*, © Xiaoyan Hou*, © Na Guo, © Le Song, © Weifang Zhang

Peking University Third Hospital, Department of Nuclear Medicine, Beijing, China

*Contributed equally to this work as first authors.

Abstract

A 68-year-old woman with low back pain for 2 months was admitted. T2-weighted fat-saturated imaging revealed hyperintense lesions in multiple lumbar regions, suggesting the possibility of bone metastases. Multiple osteolytic and mixed osteolytic-osteoblastic lesions with significant ¹⁸F-fluorodeoxyglucose (¹⁸F-FDG) uptake, as well as multiple osteoblastic lesions with mild ¹⁸F-FDG uptake, were observed on subsequent ¹⁸F-FDG positron emission tomography/computed tomography without an identifiable primary lesion. This patient was pathologically diagnosed with low-grade myofibroblastic sarcoma (LGMS) after biopsy and surgery. Although multiple bone involvement in LGMS is extremely rare, this case suggests that it should be considered in the differential diagnosis of multiple bone metastases.

Keywords: Low-grade myofibroblastic sarcoma, bone destruction, ¹⁸F-FDG PET/CT

Öz

Altmış sekiz yaşında kadın hasta 2 aydır bel ağrısı şikayetiyle başvurdu. T2 ağırlıklı yağa doymuş görüntülemeye birden fazla lomber bölgede hiperintens lezyonlar saptandı ve bu da kemik metastazı olasılığını düşündürdü. ¹⁸F-florodeoksiglukoz (¹⁸F-FDG) pozitron emisyon tomografisi/bilgisayarlı tomografisinde tanımlanabilir bir primer olmaksızın, belirgin ¹⁸F-FDG alımına sahip çoklu osteolitik ve mikst osteolitik-osteoblastik lezyonların yanı sıra hafif ¹⁸F-FDG alımına sahip çoklu osteoblastik lezyonlar gözlemlendi. Bu hastaya biyopsi ve cerrahi sonrasında patolojik olarak düşük dereceli miyofibroblastik sarkom (LGMS) tanısı konuldu. LGMS'de çoklu kemik tutulumu son derece nadir olmakla birlikte, bu olgu LGMS'nin çoklu kemik metastazlarının ayrıncı tanısında dikkate alınması gerektiğini düşündürmektedir.

Anahtar kelimeler: Düşük dereceli miyofibroblastik sarkom, kemik yıkımı, ¹⁸F-FDG PET/CT

Addresses for Correspondence: Prof. Weifang Zhang, Le Song, MD, Peking University Third Hospital, Department of Nuclear Medicine, Beijing, China
Phone: +15611963920 **E-mail:** tsy1997@126.com ORCID ID: orcid.org/0000-0003-3879-1285

Prof. Le Song, MD, Peking University Third Hospital, Department of Nuclear Medicine, Beijing, China
Phone: +86-010-82264935, **E-mail:** songle@bjmu.edu.cn ORCID ID: orcid.org/0000-0002-7532-7150

Received: 26.09.2023 **Accepted:** 25.03.2024 **Epub:** 06.06.2024



Copyright© 2024 The Author. Published by Galenos Publishing House on behalf of the Turkish Society of Nuclear Medicine.
This is an open access article under the Creative Commons Attribution-NonCommercial-NoDerivatives 4.0 (CC BY-NC-ND) International License.

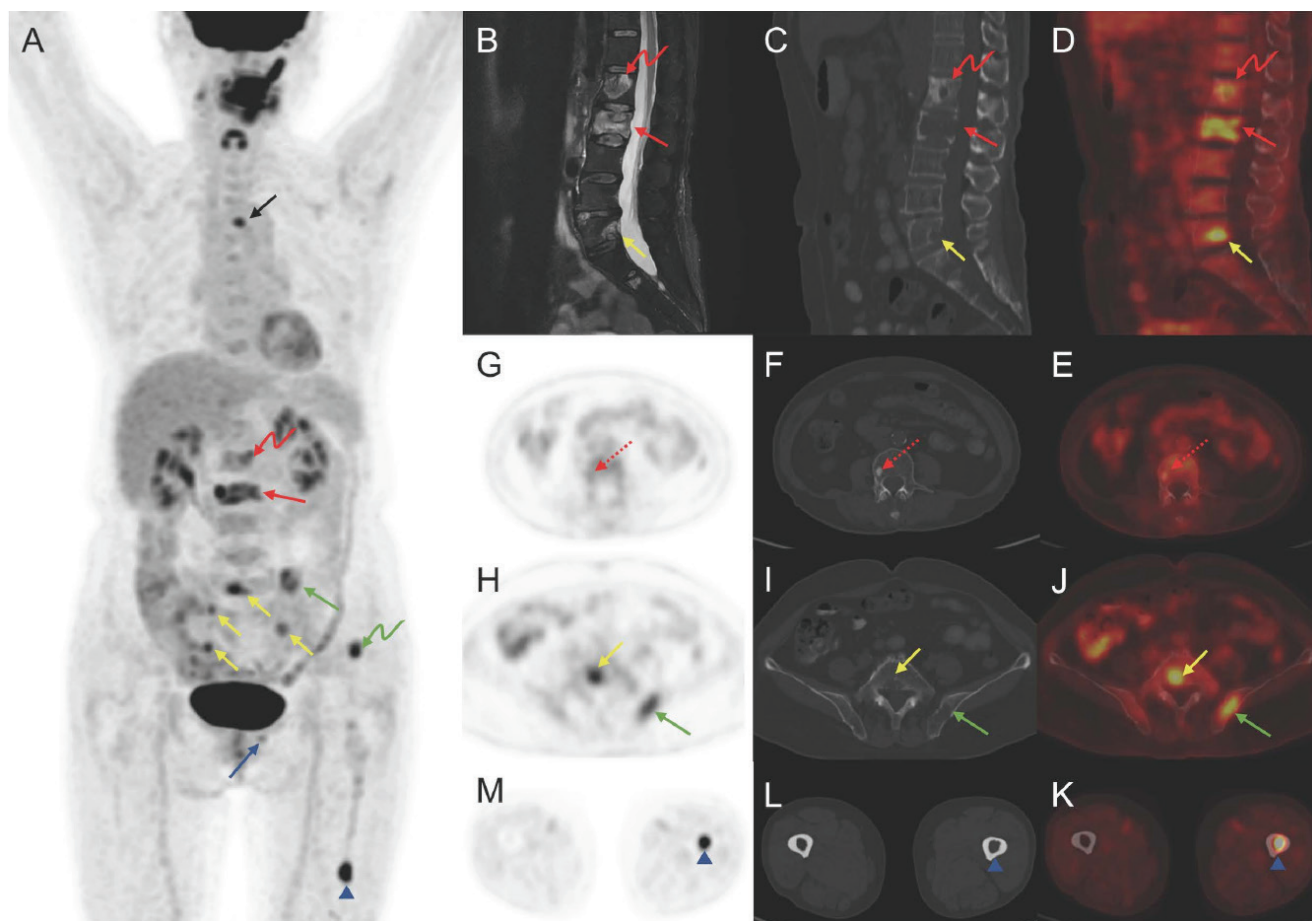


Figure 1. A 68-years-old woman with low back pain for 2 months was admitted. T2-weighted fat-saturated imaging revealed heterogeneous hyperintense lesions in multiple lumbar regions, indicating the likelihood of bone metastases. To identify the primary lesion and determine the tumor stage, the ^{18}F -fluorodeoxyglucose (^{18}F -FDG) positron emission tomography/computed tomography (PET/CT) was performed (A, MIP; B, sagittal T2-weighted fat-saturated magnetic resonance imaging; C, sagittal CT; D, sagittal PET/CT; E, J, K, axial PET/CT; F, I, L, axial CT; G, H, M, axial PET). Multiple osteolytic (solid arrow) and mixed osteolytic-osteoblastic (bend arrow) lesions with significant ^{18}F -FDG uptake, as well as multiple osteoblastic lesions (dotted arrow) with mild ^{18}F -FDG uptake, were observed in the thoracic vertebra (black arrow), lumbar vertebra (red arrow), sacrum (yellow arrow), right 12th rib, left ilium (green arrow), left pubis (blue arrow), and femur (arrowhead), without an identifiable primary lesion. In addition, intense activity was found in the oral cavity and left cheek area, with no abnormalities detected on the corresponding CT scans, indicating unspecific uptake. This patient underwent biopsy of the left iliac region and surgery of L3 and was pathologically diagnosed with low-grade myofibroblastic sarcoma (LGMS). LGMS is a rare mesenchymal tumor that was previously thought to mainly originate from the head and neck region, but a recent study suggested it may be more common in the extremities (1,2). The majority of LGMS occurs in the soft tissue and is infrequent in the bone (2,3). The distal femur is the most prevalent site for bone LGMS, followed by the ilium, and the vertebrae are rare (3,4,5). LGMS has been described as having a low-grade malignant potential that may locally recur and less frequently metastases (2). Multifocal involvement is extremely rare, with only one case of multicentric soft tissue involvement described by Wechalekar et al. (6). We report an extremely rare LGMS case of multiple bone involvement (multiple vertebrae, rib, ilium, pubis, and femur) without any soft tissue lesions. Furthermore, in this case, different types of bone destruction (osteolytic, mixed osteolytic-osteoblastic, and osteoblastic) were observed, which is quite different from the primary and metastatic bone lesions in the previous studies, which typically manifest as osteolytic bone destruction (1,4,5,7,8). ^{18}F -FDG PET/CT scan is an important approach in differentiating malignant sarcomatous lesions from benign lesions, especially for the equivocal lesions on conventional imaging, as well as a primary diagnostic tool for metastatic lesion detection (9,10). The presence of primary bone LGMS on the ^{18}F -FDG PET/CT scan has been reported by Hou et al. (8). To the best of our knowledge, this is the first case of LGMS involving numerous bones and causing different types of bone destruction with heterogeneous ^{18}F -FDG uptake on the ^{18}F -FDG PET/CT. Despite its rarity, this case suggests that LGMS with multiple bone involvement should be considered when multiple bone metastases are suspected.

Ethics

Informed Consent: The written informed consent has been obtained from the patient.

Authorship Contributions

Concept: L.S., W.Z., Design: L.S., W.Z., Data Collection or Processing: X.H., Analysis or Interpretation: X.H., Literature Search: H.L., N.G., Writing: H.L.

Conflict of Interest: No conflicts of interest were declared by the authors.

Financial Disclosure: This work was supported by the Key Clinical Projects of Peking University Third Hospital (no.: BYSY2022060).

References

1. San Miguel P, Fernández G, Ortiz-Rey JA, Larrauri P. Low-grade myofibroblastic sarcoma of the distal phalanx. *J Hand Surg Am.* 2004;29:1160-1163.
2. Chan JY, Gooi Z, Wong EW, Ng SK, Tong MC, Vlantis AC. Low-grade myofibroblastic sarcoma: A population-based study. *Laryngoscope.* 2017;127:116-121.
3. Hadjigeorgiou GF, Samaras V, Varsos V. Low-grade myofibroblastic sarcoma of the thoracic spine: report of an extreme rare case. *Br J Neurosurg.* 2017;31:731-733.
4. Watanabe K, Ogura G, Tajino T, Hoshi N, Suzuki T. Myofibrosarcoma of the bone: a clinicopathologic study. *Am J Surg Pathol.* 2001;25:1501-1507.
5. Saito T, Mitomi H, Kurisaki A, Torigoe T, Takagi T, Suehara Y, Okubo T, Kaneko K, Yao T. Low-grade myofibroblastic sarcoma of the distal femur. *Int J Surg Case Rep.* 2013;4:195-199.
6. Wechalekar MD, Ayres O, Farshid G, Clayer M, Cleland LG. Multicentric myofibroblastic sarcoma. *BMJ Case Rep.* 2014;2014:bcr2013201666.
7. Wang L, Li LX, Chen DQ, Yang L, Li SK, Cheng C. Low-grade Myofibroblastic sarcoma: clinical and imaging findings. *BMC Med Imaging.* 2019;19:36.
8. Hou W, Su M, Li Q, Tian R. Low-Grade Myofibroblastic Sarcoma Demonstrated on 99mTc-MDP Bone Scan and 18F-FDG PET/CT. *Clin Nucl. Med.* 2020;45:549-551.
9. Mendoza H, Nosov A, Pandit-Taskar N. Molecular imaging of sarcomas with FDG PET. *Skeletal Radiol.* 2023;52:461-475.
10. Roberts CC, Kransdorf MJ, Beaman FD, Adler RS, Amini B, Appel M, Bernard SA, Fries IB, Germano IM, Greenspan BS, Holly LT, Kubicky CD, Lo SS, Mosher TJ, Sloan AE, Tuite MJ, Walker EA, Ward RJ, Wessell DE, Weissman BN. ACR Appropriateness Criteria Follow-Up of Malignant or Aggressive Musculoskeletal Tumors. *J Am Coll Radiol.* 2016;13:389-400.



Intrathyroidal Parathyroid Adenoma

İntratiroidal Paratiroid Adenomü

© Sara Zougari¹, © Mohamed Aziz Bsiss¹, © Aboubaker Matrane¹, © Abdelouahed Marrat², © Ibtissam Zrara Touiti²

¹Mohammed VI University Hospital, Department of Nuclear Medicine, Marrakesh, Morocco

²Al Fadl Pathological Anatomy and Cytology Laboratory, Department of Pathology, Marrakesh, Morocco

Abstract

Intrathyroidal parathyroid adenoma is a rare anomaly with an incidence of 1.4-6%. A cause of failure in the therapeutic management of hyperparathyroidism is the ectopic localization of the adenoma, particularly intrathyroidal. This is the case of a 51-year-old patient with no particular pathological history who presented with neck pain and whose clinical examination revealed a goiter. Parathyroid myocardial perfusion imaging (MIBI) scintigraphy revealed an elective MIBI-fixing focus with an upper left polar projection compatible with a parathyroid origin. A left lobectomy was performed. Anatomopathological study showed a parathyroid adenoma associated with dystrophic thyroid parenchyma, with no obvious histological signs of malignancy. Post-therapeutic laboratory work-up was normalized. Parathyroid adenoma, intrathyroidal, is an uncommon lesion but may be responsible for therapeutic failure in hyperparathyroidism. MIBI parathyroid gland scintigraphy is the gold standard for the diagnosis of parathyroid ectopy.

Keywords: Intrathyroidal parathyroid adenoma, parathyroid ectopy, MIBI scintigraphy

Öz

İntratiroidal paratiroid adenomu nadir görülen bir anomali olup görülme sıklığı %1,4-6'dır. Hiperparatiroidizmin terapötik tedavisindeki başarısızlığın bir nedeni, adenomun ektopik lokalizasyonu, özellikle intratiroidal olmasıdır. Burada, özel bir patolojik geçmişi olmayan, boyun ağrısı şikayetiyle başvuran ve klinik muayenesinde guatr tespit edilen 51 yaşında bir hasta sunulmaktadır. Paratiroid miyokardiyal perfüzyon görüntüleme (MIBI) sintigrafisi, paratiroid kökeniyle uyumlu projeksiyonlu MIBI tutulum odağını ortaya çıkardı. Sol lobektomi yapıldı. Anatomopatolojik çalışma, belirgin bir histolojik malignite belirtisi olmayan, distrofik tiroid parankimi ile ilişkili bir paratiroid adenomunu gösterdi. Tedavi sonrası laboratuvar çalışmaları tamamlandı. İntratiroidal paratiroid adenomu nadir görülen bir lezyondur ancak hiperparatiroidizmde tedavi başarısızlığından sorumlu olabilir. MIBI paratiroid bezi sintigrafisi paratiroid ektopisinin tanısında altın standarttır.

Anahtar kelimeler: İntratiroidal paratiroid adenomu, paratiroid ektopisi, MIBI sintigrafisi

Address for Correspondence: Sara Zougari MD, Mohammed VI University Hospital, Department of Nuclear Medicine, Marrakesh, Morocco

Phone: +212610996182 **E-mail:** sarazougari@gmail.com **ORCID ID:** orcid.org/0009-0004-3066-6548

Received: 12.12.2023 **Accepted:** 28.03.2024 **Epub:** 06.06.2024



Copyright© 2024 The Author. Published by Galenos Publishing House on behalf of the Turkish Society of Nuclear Medicine. This is an open access article under the Creative Commons Attribution-NonCommercial-NoDerivatives 4.0 (CC BY-NC-ND) International License.

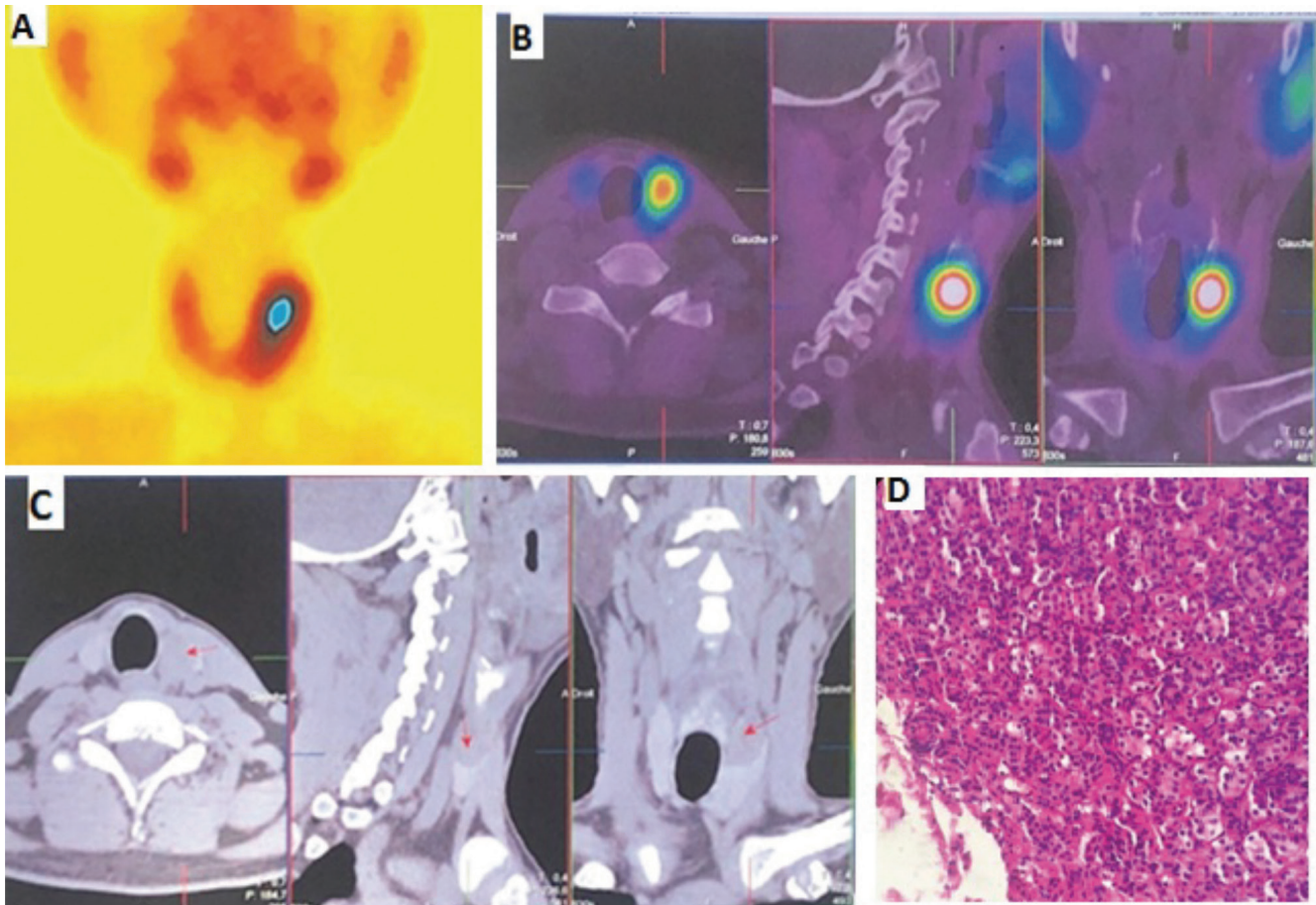


Figure 1. This is the case of a 51-year-old patient, with no particular pathological history, who was consulted for cervical pain and swelling. Clinical examination revealed cervical goiter. Biological workup showed a profile characteristic of hyperparathyroidism, with parathyroid hormone (PTH) elevated to 922.3 pg/mL, hypercalcemia to 152 mg/L, and hypophosphatemia to 10 mg/L. Cervical ultrasound revealed a normal-sized thyroid gland with a left upper lobar thyroid nodule classified as EU-TIRADS 5 and measuring 1.4x2 cm. Myocardial perfusion imaging (MIBI) scintigraphy revealed an elective MIBI-fixing focus with an upper left polar projection (A) compatible with parathyroid origin. In addition, single-photon emission computed tomography/computed tomography (SPECT/CT) images (B) and CT images (C) confirmed the intra-thyroidal location of the parathyroid nodule. A left lobectomy was performed, and the anatomopathological study showed a parathyroid adenoma associated with dystrophic thyroid parenchyma, with no obvious histological signs of malignancy. (D) Biological tests performed 1 week after surgery showed normal levels, with calcemia =83 mg/L and PTH =61.2 pg/mL.

Hyperparathyroidism is the third most common endocrinopathy, with parathyroid adenoma being the most common etiology. The latter may be located ectopically in 11-25% of cases, secondary to embryonic migration anomalies (1). Intrathyroidal parathyroid adenoma is a rare anomaly with an incidence of 1.4-6%. One of the causes of failure in the therapeutic management of hyperparathyroidism is the ectopic localization of the adenoma, particularly intrathyroidal (2). The diagnosis of the location of the ectopic gland depends mainly on imaging studies, such as ultrasound, CT, magnetic resonance imaging (MRI), Tc-99m-MIBI SPECT/CT, or ^{18}F -fluorocholine positron emission tomography (PET)/CT (3). Tc-99m-MIBI SPECT/CT represents additional advantages in the evaluation of parathyroid adenoma. It can be used to estimate the function of the parathyroid gland and the extent of its hyperplasia is the simplest and most widely used noninvasive method for preoperative determination of the location and position of the gland (4). Numerous studies have confirmed the usefulness of MIBI scintigraphy in the exploration of the parathyroid gland in the management of hyperparathyroidism. In a group of over 1,500 cases, Roy et al. (5) observed a parathyroidectomy success rate of over 95% and the presence of an ectopic parathyroid gland in 6-16% of cases (38% located in the thymus, 31% in the retropharynx and 18% intra-thyroid). In such cases, these authors found MIBI scintigraphy was diagnostically superior, with a sensitivity of 89% compared with ultrasound (sensitivity 59%) (5). Ishibashi et al. (6) recommended that MIBI scintigraphy be performed before any other diagnostic means of localization, such as CT or MRI. This author observed a sensitivity of 70% and a specificity of 88% for scintigraphy, which is superior to CT (40% and 88% respectively) and MRI (60% and 88%) (6). Other studies also point to MIBI scintigraphy as the best performing diagnostic technique, with sensitivity approaching 90% (7). However, MIBI scintigraphy has certain limitations. For example, when parathyroid hyperplasia is not evident, or the focus is too small to be covered by thyroid tissue, or when associated with a multinodular goiter, false-negative results can occur; hence, it is also of interest in the differential diagnosis of benign thyroid disease. Furthermore, when ultrasound and Tc-99m-MIBI SPECT/CT cannot determine intrathyroid nodules, PET/CT may be a better alternative (8).

Ethics

Informed Consent: The patient consent was obtained.

Authorship Contributions

Surgical and Medical Practices: S.Z., M.A.B., A.M., A.Mar., I.Z.T., Concept: S.Z., Design: S.Z., Data Collection or Processing: S.Z., Analysis or Interpretation: S.Z., M.A.B., A.M., A.Mar., I.Z.T., Literature Search: S.Z., Writing: S.Z.

Conflict of Interest: No conflicts of interest were declared by the authors.

Financial Disclosure: The authors declare that this study has received no financial support.

References

1. Kaplan EL, Yashiro T, Salti G. Primary hyperparathyroidism in the 1990s. Choice of surgical procedures for this disease. *Ann Surg.* 1992;215:300-317.
2. Mazeh H, Kouniavsky G, Schneider DF, Makris KI, Sippel RS, Dackiw AP, Chen H, Zeiger MA. Intrathyroidal parathyroid glands: small, but mighty (a Napoleon phenomenon). *Surgery.* 2012;152:1193-1200.
3. Hai R, Xie LJ, You Q, Wu F, Qiu GC, Zhou XY. Diagnosis of Ectopic Intrathyroidal Parathyroid Adenoma with Nodular Goiter by 18F Fluorocholine: A Case Report. *Ear Nose Throat J.* 2022;1455613221103082.
4. Özdemir E, Genç M, Aydos U, Polat ŞB, Kandemir Z, Tam AA, Yildirim N, Türkölmez Ş. Comparison of 99mTc-MIBI planar scintigraphy, SPET/CT and ultrasonography in detection of parathyroid adenoma in patients with primary hyperparathyroidism. *Hell J Nucl Med.* 2020;23:21-26.
5. Roy M, Mazeh H, Chen H, Sippel RS. Incidence and localization of ectopic parathyroid adenomas in previously unexplored patients. *World J Surg.* 2013;37:102-106.
6. Ishibashi M, Nishida H, Hiromatsu Y, Kojima K, Uchida M, Hayabuchi N. Localization of ectopic parathyroid glands using technetium-99m sestamibi imaging: comparison with magnetic resonance and computed tomographic imaging. *Eur J Nucl Med.* 1997;24:197-201.
7. Castellani M, Reschini E, Longari V, Paracchi A, Corbetta S, Marotta G, Gerundini P. Role of Tc-99m sestamibi scintigraphy in the diagnosis and surgical decision-making process in primary hyperparathyroid disease. *Clin Nucl Med.* 2001;26:139-144.
8. Piccardo A, Trimboli P, Puntoni M, Foppiani L, Treglia G, Naseri M, Bottoni GL, Massollo M, Sola S, Ferrarazzo G, Bruzzone M, Catrambone U, Arlandini A, Paone G, Ceriani L, Cabria M, Giovanella L. Role of 18F-Choline Positron Emission Tomography/Computed Tomography to Detect Structural Relapse in High-Risk Differentiated Thyroid Cancer Patients Thyroid. 2019;29:549-556.



Tc-99m-MDP Uptake in Extraosseous Metastases from Ovarian Papillary Serous Adenocarcinoma

Over Papiller Seröz Adenokarsinomuna Bağlı Ekstraosseöz Metastazlarda Tc-99m-MDP Tutulumu

✉ Komal Bishnoi, ✉ Kanhaiyalal Agrawal, ✉ P. Sai Sradha Patro, ✉ Girish Kumar Parida

All India Institute of Medical Sciences, Department of Nuclear Medicine, Bhubaneswar, India

Abstract

The uptake of Tc-99m-uptake of Tc-99m-methylene diphosphonate (MDP) on bone scintigraphy can be seen at sites other than bone in a varying number of benign and malignant conditions. Extraosseous metastatic calcifications can occur in ovarian papillary serous adenocarcinoma (PSAC). These extraosseous calcifications show Tc-99m-MDP uptake. We report a case of a female in her sixties who had a previous history of PSAC of the ovary. The patient had undergone neoadjuvant chemotherapy (NACT) followed by total abdominal hysterectomy and bilateral salpingo-oophorectomy. She also received adjuvant chemotherapy. Tc-99m-MDP bone scan was performed post chemotherapy because the patient complained of lower backache. The scan showed increased uptake in the lower thoracic and lumbar vertebral regions. However, single-photon emission computed tomography/computed tomography (CT) localizes the uptake to metastatic calcified peritoneal deposits. Further ¹⁸F-fluorodeoxyglucose positron emission tomography/CT confirmed widespread peritoneal and omental metastatic disease with increased uptake.

Keywords: Tc-99m-MDP, metastases, ovarian papillary serous adenocarcinoma

Öz

Kemik sintigrafisinde Tc-99m-metilen difosfonatın (MDP) Tc-99m alımı, çeşitli iyi huylu ve kötü huylu durumlarda kemik dışındaki bölgelerde de görülebilir. Yumurtalık papiller seröz adenokarsinomunda (PSAC) ekstraosseöz metastatik kalsifikasyonlar meydana gelebilir. Bu ekstraosseöz kalsifikasyonlar Tc-99m-MDP alımını göstermektedir. Daha önce overde PSAC öyküsü olan altmışlı yaşlarındaki bir kadın hasta bildirilmektedir. Hastaya neoadjuvan kemoterapi (NACT), ardından total abdominal histerektomi ve iki taraflı salpingo-ooferektomi uygulandı. Ayrıca hasta adjuvan kemoterapi de aldı. Hastanın bel ağrısı şikayeti nedeniyle kemoterapi sonrası Tc-99m-MDP kemik taraması yapıldı. Tarama, alt torasik ve lomber vertebral bölgelerde artan alım gösterdi. Bununla birlikte, tek foton emisyonlu bilgisayarlı tomografi/bilgisayarlı tomografi (BT), metastatik kalsifiye peritoneal birikimlerin alımını lokalize etmektedir. İlave ¹⁸F-florodeoksiglukoz pozitron emisyon tomografisi/BT, artan alımla birlikte yaygın peritoneal ve omental metastatik hastalığı doğruladı.

Anahtar kelimeler: Tc-99m-MDP, metastaz, over papiller seröz adenokarsinomu

Address for Correspondence: Prof. Kanhaiyalal Agrawal, MD, All India Institute of Medical Sciences, Department of Nuclear Medicine, Bhubaneswar, India

Phone: +8195930013 **E-mail:** nucmed_kanhaiyalal@aiimsbhubaneswar.edu.in ORCID ID: orcid.org/0000-0003-4855-8938

Received: 11.01.2024 **Accepted:** 06.04.2024 **Epub:** 06.06.2024



Copyright© 2024 The Author. Published by Galenos Publishing House on behalf of the Turkish Society of Nuclear Medicine.
This is an open access article under the Creative Commons Attribution-NonCommercial-NoDerivatives 4.0 (CC BY-NC-ND) International License.

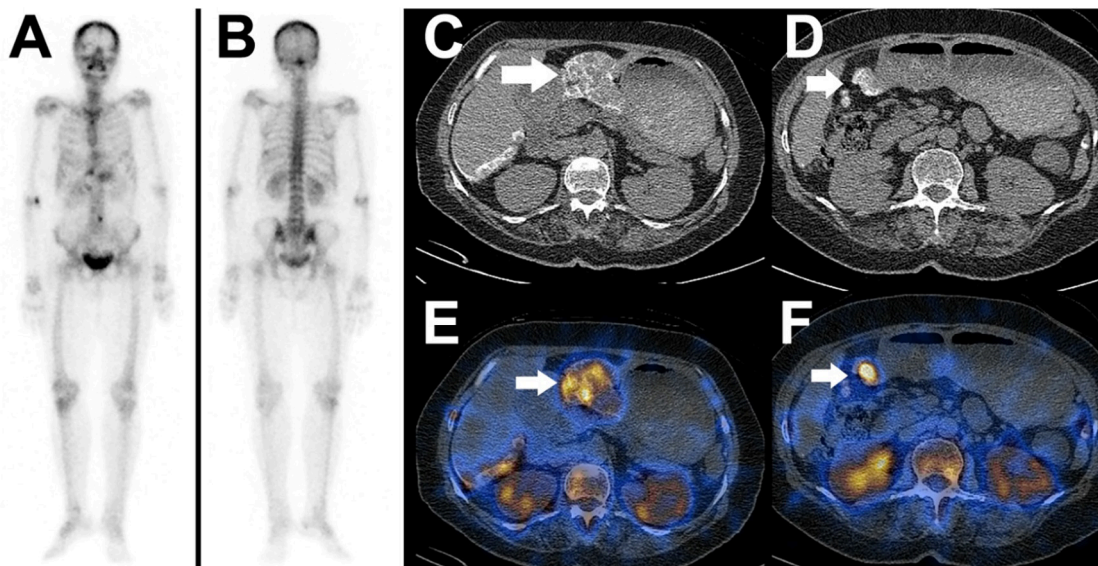


Figure 1. Ovarian cancer is the seventh most common cancer worldwide in women (1). The mortality rate is high, attributable to diagnosis at an advanced stage, which is often known to be a “silent killer” (2,3). Tc-99m-methylene diphosphonate (MDP) is a bone-seeking radiopharmaceutical used to rule out bone metastases. On bone scintigraphy, the uptake can be seen at sites other than the bone in a varying number of benign and malignant conditions. In this case, a woman in her sixties had stage III papillary serous adenocarcinoma (PSAC) ovary diagnosed almost 3 years ago (in 2020). She received three cycles of neoadjuvant chemotherapy and underwent total abdominal hysterectomy and bilateral salpingo-oophorectomy, infracolic omentectomy, left paracolic peritoneum, and pelvic peritoneum removal. Thereafter, the patient was asymptomatic and was followed up. A follow-up contrast-enhanced computed tomography (CT) scan of the abdomen showed few hypodense lesions in the liver and multiple soft tissue lesions indenting the liver surface in the peritoneum and abdominal wall with few small bilateral lung nodules, which were suspicious for widespread metastases. Therefore, the patient received 9 cycles of adjuvant chemotherapy with paclitaxel and bevacizumab for 6 months. The patient presented with lower backache during the course of chemotherapy. Tc-99m-MDP bone scan was performed to rule out any bone metastases. (A, B): anterior and posterior planar bone scan images show increased tracer uptake in the lower thoracic and lumbar vertebrae region, although the uptake in the lower thoracic vertebrae region is not limited to the bones. To rule out this dilemma, single-photon emission computed tomography/CT (SPECT/CT) of the abdomen and pelvis was performed. (C, D, E, F): axial CT and fused SPECT/CT images of the abdomen show tracer uptake in the calcified deposits along the surface of the liver (peritoneal) and other peritoneal deposits (arrows), suggestive of peritoneal metastatic disease ruling out bone

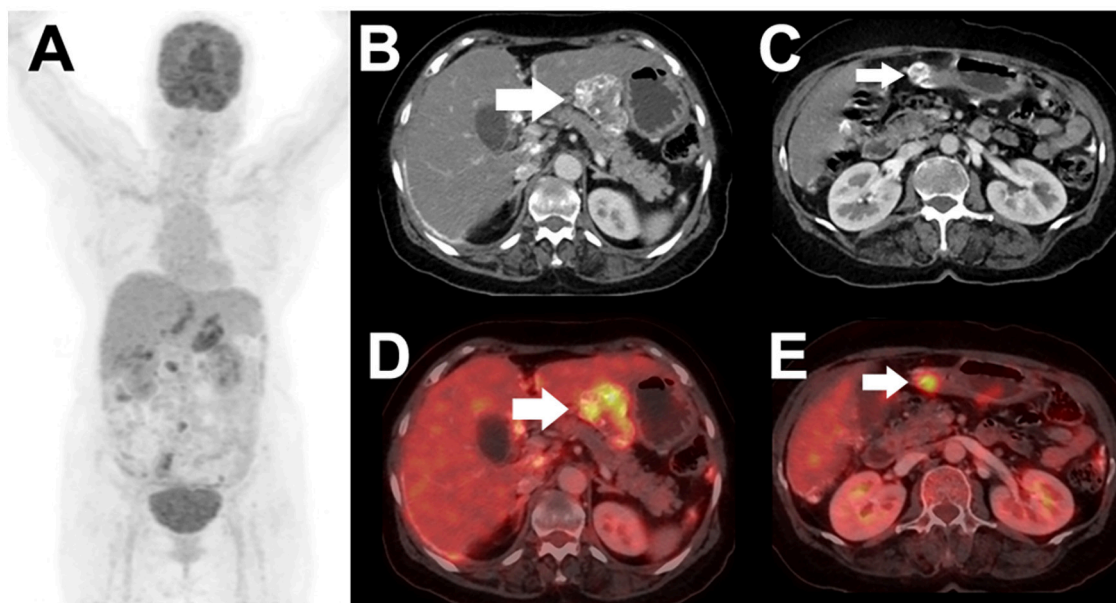


Figure 2. A further whole body (vertex to mid-thigh) ^{18}F -fluorodeoxyglucose positron emission tomography (PET)/CT was performed to assess the extent of metastatic disease. (A): maximum intensity projection image shows multifocal increased tracer uptake in the abdomen and pelvis in a pattern similar to Tc-99m-MDP uptake suggesting metastatic lesions. (B, C, D, E): axial CT and fused PET/CT images of the abdomen show hypermetabolic calcified deposits along the surface of the liver (peritoneal) and peritoneal deposits (arrows) suggestive of metastatic peritoneal disease. This finding of metastatic disease was supported by the serum CA 125 level, which was 1183.1 U/mL (normal <30.2 U/mL). The patient is further started on a chemotherapy regimen including bevacizumab and carboplatin.

Many previously published studies have shown the uptake of Tc-99m-MDP in calcified metastases from Krukenberg tumor (4), endometrium, and ovary (5,6). This uncommon extrasosseous accumulation can be explained by the affinity of Tc-99m-MDP for hydroxyapatite crystals and calcium precipitates (7) in soft tissue metastases from ovarian PSAC. Another explanation could be altered extracellular fluid and tracer handling dynamics and tumor neovascularization with altered capillary permeability (4,8). This extrasosseous uptake on bone scans leads to misdiagnosis of bone metastases. Hybrid imaging like SPECT/CT, provides additional anatomic information and leads to localization of tracer uptake for further clarification, as in this case.

Ethics

Informed Consent: Written informed consent has been obtained from the patient for the publication of the case.

Authorship Contributions

Concept: K.A., P.S.S.P., G.K.P., Data Collection or Processing: K.B., Analysis or Interpretation: K.B., K.A., P.S.S.P., G.K.P., Literature Search: K.B., Writing: K.B., K.A.

Conflict of Interest: No conflicts of interest were declared by the authors.

Financial Disclosure: The authors declare that this study has received no financial support.

References

- Momenimovahed Z, Tiznobaik A, Taheri S, Salehiniya H. Ovarian cancer in the world: epidemiology and risk factors. *Int J Womens Health*. 2019;11:287-299.
- Bharwani N, Reznick RH, Rockall AG. Ovarian Cancer Management: the role of imaging and diagnostic challenges. *Eur J Radiol*. 2011;78:41-51.
- Sharma SK, Nemieboka B, Sala E, Lewis JS, Zeglis BM. Molecular Imaging of Ovarian Cancer. *J Nucl Med*. 2016;57:827-833.
- Oppenheimer AG, Onyedika C, Freeman LM. MDP uptake in peritoneal carcinomatosis and Krukenberg tumors from mucinous adenocarcinoma. *Clin Nucl Med*. 2011;36:235-236.
- Radin AI, Youssef IM, Quimbo RD, Perone RW, Guerrieri C, Abdel-Dayem HM. Technetium-99m diphosphonate imaging of psammocarcinoma of probable ovarian origin: case report and literature review. *Clin Nucl Med*. 2005;30:395-399.
- Ozulker T, Ozulker F, Ozpacaci T. 99mTc-MDP and 18F-FDG uptake in calcified metastatic lesions from ovarian papillary serous adenocarcinoma. *Hell J Nucl Med*. 2009;12:287-288.
- Kaye J, Hayward M. Soft tissue uptake on 99mTc methylene diphosphonate bone scan imaging: pictorial review. *Australas Radiol*. 2002;46:13-21.
- Agrawal K, Bhattacharya A, Harisankar CN, Abrar ML, Dhaliwal LK, Mittal BR. F-18 fluoride uptake in calcified extrasosseous metastases from ovarian papillary serous adenocarcinoma. *Clin Nucl Med*. 2012;37:e22-e23.

2024 Referee Index - 2024 Hakem Dizini

Ali Fuat Yapar
Ali Sarıkaya
Ayşe Mavi
Ayşegül Akgün
Berna Okudan Tekin
Bilal Kovan
Bilge Volkan Salancı
Bircan Sönmez
Burcu Esen Akkaş
Bülent Turgut
Cengiz Taşçı
Corinna Altini
Dragana Sobic Saranovic
Elgin Özkan
Emre Entok
Esra Arslan
Fatma Suna Kıraç
Fikriye Gül Gümüşer
Funda Üstün
Gamze Çapa Kaya
Gonca G. Bural
Gözde Dağlıöz Görür
Hakan Demir
Hülya Peker
İrfan Peksoy

Mahmut Yüksel
Majid Assadi
Maria Lyra Georgosopoulou
Mehmet Reyhan
Meliha Korkmaz
Meryem Kaya
Metin Kır
Mine Araz
Mustafa Demir
Mustafa Yıldız
Nedim C.M. Gülaldı
Nilüfer Yıldırım
Nosheen Fatima
Özgül Ekmekçioğlu
Pelin Arıcan
Serdar Savaş Gül
Serkan İşgören
Sevin Coşar Ayaz
Suna Erdoğan
Tamer Özülker
Tunç Öneş
Yakup Yürekli
Zehra Özcan
Zeynep Burak

2024 Author Index - 2024 Yazar Dizini

Abdelouahed Marrat	209	Doğangün Yüksel	90
Abderrahim Doudouh	185	Doğu Vurallı Bakkaloğlu	125
Aboubaker Matrane.....	209	Domenico Michele Modica	121
Ahmed Saad Abdlkadir	179, 196	Duygu Has Şimşek	109, 125, 199
Ahmet Eren Şen.....	40	Ebru Tatcı.....	147
Ahu Senem Demiröz.....	43	Ecenur Dursun	167
Akram Al-Ibraheem.....	179, 196	Ediz Beyhan	43
Alaa' Abufara	179	Elgin Özkan	193
Alessandra Castelluccia.....	1	Elvan Sayit	68
Alessandro Pitruzzella	121	Emine Göknur Işık.....	109, 199
Ali Kibar.....	54	Erkan Vardareli	174
Angela Sardaro.....	1	Esra Arslan.....	43, 47, 182
Anjali Jain	106	Fariba Amini	63
Antonino Maria Moreci.....	121	Fırat Ortaç	167
Antonio Rosario Pisani	1	Francesco Tramacere.....	1
Artor Niccoli Asabella.....	1	Funda Demirağ	147
Ashique Rahman	77	Gabriela Mateva	112
Assen Dudov	112	Gamze Beydağı.....	134
Ayça Taş	19	Gerrit Engelbrecht.....	57
Aziz Gültekin	90	Girish Kumar Parida	77, 212
Bala Başak Öven	134	Giuseppe Mario Galfano	121
Baraa Alsyouf	196	Gözde Mutevelizade	68
Barış Sarıkçalı	19	Gül Gümüşer	68
Batool Albalooshi.....	179	Gülhan Duman	19
Bedriye Büşra Demirel.....	11	Gülin Uçmak.....	11
Bing-Qi Li	115	Haiyan Li.....	129
Burak Demir.....	167, 193	Halil Başar.....	11
Caner Civan	109,125	Hui Li.....	115, 203, 206
Cansu Güneren.....	54	Humberto Varela	28
Carlos Avila.....	28	Hussam Haddad	196
Cengiz Taşçı	66	Ibtissam Zrara Touiti.....	209
Ceren Sezgin Arıkbası	68	İbrahim Taşkın Rakıcı.....	43
Ceyda Turan Bektaş	47	Jalil Pirayesh Islamian	138
Chanittha Buakhao	189	Jocelyn Chu	118
Chaymae Bensaid	185	Kaan Akçay.....	134
Chien-an Liu.....	156	Kamal Al-Rabi	179
Corinna Altini.....	1	Kanhaiyalal Agrawal.....	77, 212
Cristina Ferrari	1	Kemal Ünal.....	174
Çağlagül Erol	40	Kerim Sönmezoğlu	54
Çiğdem Soydal.....	167	Khulood Al Riyami	106
Derya Kızılgöz	147	Ko-Han Lin.....	156
Diğdem Kuru Öz.....	193	Komal Bishnoi.....	212
Dino Rubini.....	1	Kübra Şahin.....	54

2024 Author Index - 2024 Yazar Dizini

Lavish Kakkar.....	38	Saeed Farzanehfar	138
Le Song	115, 203, 206	Salah Oueriagli Nabih.....	185
Levent Güner.....	174	Salih Taşkın.....	167
Levent Kabasakal.....	134	Salvatore Ialuna.....	121
Mahsa Shahrabakki.....	138	Salvatore Poma.....	121
Mahsa Sobhi Lord.....	138	Samiye Demirezen.....	90
Man Mohan Singh.....	38	Sara Zougari.....	209
Maria Cristina Martínez.....	28	Satyawati Deswal.....	38
Marina Garcheva-Tsacheva.....	112	Seçkin Bilgiç.....	147
Mehmet Emin Mavi.....	50, 63	Seda Gülbahar Ateş.....	11
Melis Ofilas.....	199	Selim Doğan.....	47
Mennaallah Mahmoud.....	156	Serkan Çelik.....	134
Meryem Aboussabr.....	185	Serkan Kuyumcu.....	109, 125
Mine Araz.....	167	Sevim Baykal Koca.....	182
Mohamed Aziz Bsiss.....	209	Seyfettin Ilgan.....	63
Mohsen Qutbi.....	94	Seyit Ahmet Ertürk.....	19
Muhammet Halil Baltacıoğlu.....	167	Sharjeel Usmani.....	106
Muhammet Sait Sağır.....	54	Shashwat Verma.....	38
Murat Fani Bozkurt.....	50	Sira Vachatimanont.....	189
Mustafa Altınkaynak.....	109	Subhash Kheruka.....	106
Na Guo.....	115, 206	Tarık Şengöz.....	90
Nalan Alan Selçuk.....	134	Tatiana Cadavid.....	28
Napisa Bunnag.....	189	Tebatso Tebeila.....	57
Natale Quartuccio.....	121	Tejasvini Singhal.....	77
Nathalie Hernández-Hidalgo.....	28	Tevfik Fikret Çermik.....	43, 47, 182
Negisa Seyyedi.....	138	Tsz-Kit Chow.....	118, 132
Nikolina Novoselska.....	112	Vincenzo Luca Lentini.....	121
Nurhan Ergül.....	182	Vipin V Jayakrishnan.....	106
Nuriye Özlem Küçük.....	167, 193	Walter Endres.....	57
Omar Ait Sahel.....	185	Weifang Zhang.....	115, 203, 206
Osayande Evbuomwan.....	57	Xia Lu.....	129
Ömer Sönmez.....	134	Xiaoyan Hou.....	206
Özge Ulaş Babacan.....	19	Yasemin Parlak.....	68
Özlem Özmen.....	147	Yasemin Şanlı.....	199
Özlem Şahin.....	40	Yassir Benameur.....	185
P. Sai Sradha Patro.....	212	Yavuz Siliğ.....	19
Parneet Singh.....	77	Yüksel Ürün.....	193
Pavel Bochev.....	112	Zahida Niaz.....	106
Peyman Sheikhzadeh.....	138	Zehranur Tosunoğlu.....	47, 182
Priyamedha Bose Thakur.....	38	Zekiye Hasbek.....	19
Raghad Alhouwari.....	196	Zeynep Aydın.....	40
Rezvan Samimi.....	138	Zeynep Gözde Özkan.....	199
Rheun-Chuan Lee.....	156		

2024 Subject Index / 2024 Konu Dizini

¹⁸ F prostate-specific membrane antigen/ ¹⁸ F prostat-spesifik membran antijeni	38	Extraosseous uptake/Kemik dışı tutulum	106
¹⁸ F PSMA PET/CT/ ¹⁸ F PSMA PET/BT	38	Fallopian tube fimbria/Fallop tüpü fimbriyası	115
¹⁸ F-choline positron emission tomography/computed tomography/ ¹⁸ F-kolin pozitron emisyon tomografisi/bilgisayarlı tomografi	185	FDG/FDG	112
¹⁸ F-FCH PET/CT/ ¹⁸ F-FCH PET/BT	1	Fibroblast activation protein/Fibroblast aktivasyon proteini	134
¹⁸ F-FDG PET/CT/ ¹⁸ F-FDG PET/BT	11, 43, 47, 115, 129, 132, 147, 167, 179, 182, 203, 206	Fibroblast-activation-protein inhibitors/Fibroblast aktivasyon protein inhibitörleri	77
¹⁸ F-FDG/ ¹⁸ F-FDG	54, 109, 125, 179	Fluorodeoxyglucose/Florodeoksiglukoz	193
¹⁸ F-fluorodeoxyglucose/ ¹⁸ F-florodeoksiglukoz ..	50, 63, 77, 121	Gallbladder micro-perforation/Safra kesesi mikroperforasyonu	47
¹⁸ F-PSMA/ ¹⁸ F-PSMA	57	Gated myocardial perfusion imaging/Kapılı miyokard perfüzyon sintigrafisi	66
⁶⁸ Ga-DOTA/ ⁶⁸ Ga-DOTA	54	Hepatocellular cancer/Hepatoselüler kanser	77
⁶⁸ Ga-DOTATATE PET/CT/ ⁶⁸ Ga-DOTATATE PET/BT	182	Hepatocellular carcinoma/Hepatosellüler karsinom	193
⁶⁸ Ga-DOTATATE/ ⁶⁸ Ga-DOTATATE	138	Image display/Görüntü ekranı	94
⁶⁸ Ga-DOTATOC/ ⁶⁸ Ga-DOTATOC	196	Implants/İmplantlar	174
⁶⁸ Ga-FAPI/ ⁶⁸ Ga-FAPI	125	Incidental/İnsidental	63
⁶⁸ Ga-PSMA PET/CT/ ⁶⁸ Ga-PSMA PET/BT	68	Integrated/Entegre	28
⁶⁸ Ga-PSMA/ ⁶⁸ Ga-PSMA	54	Intestinal obstruction/Bağırsak tıkanıklığı	129
⁶⁸ Gallium DOTATATE/ ⁶⁸ Galyum DOTATATE	134	Intrathyroidal parathyroid adenoma/İntratiroidal paratiroid adenomu	209
Abscess/Abse	47	Intussusception/İntususepsiyon	129
Attenuation correction/Atenüasyon düzeltilmesi	138	Jejunum/Jejunum	129
Atypical metastases/Atipik metastazlar	57	Lepidic predominant adenocarcinoma of the lung/Lepidik predominant akciğer adenokarsinomu	147
Biochemical recurrences/Biyokimyasal nüksler	1	Lincoln sign/Lincoln işareti	118
Bladder cancer/Mesane kanseri	11	Liver cancers/Karaciğer kanserleri	77
Bone destruction/Kemik yıkımı	206	Liver lesions/Karaciğer lezyonları	43
Bone marrow metastasis/Kemik iliği metastazı	132	Liver metastasis/Karaciğer metastazı	174
Bone marrow necrosis/Kemik iliği nekrozu	203	Look-up table/Arama tablosu	94
Breast cancer/Meme kanseri	106	Low-grade myofibroblastic sarcoma/Düşük dereceli miyofibroblastik sarkom	206
Bronchial carcinoid/Bronşiyal karsinoid	196	Lung/Akciğer	63
Bronchocele/Bronkosel	196	Lutetium/Lutesyum	28
Cardiac/Kardiyak	50	Lymphoma/Lenfoma	203
Cardiology/Kardiyoloji	189	Magnetic resonance imaging/Manyetik rezonans görüntüleme	193
Cartilage metastasis/Kıkırdak metastazı	179	Meckel scintigraphy/Meckel sintigrafisi	90
Cholangiocarcinoma/Kolanjiokarsinom	77	Meckel's diverticulum/Meckel divertikülü	90
Colormap/Renk haritası	94	Medical imaging/Tıbbi görüntüleme	138
Computed tomography/Bilgisayarlı tomografi	77	Medication-related osteonecrosis of the jaw/İlaca bağlı çene osteonekrozu	118
Curative radiotherapy/Küratif radyoterapi	1	Medullary thyroid carcinoma/Medüller tiroid kanseri	54
Decay constant/Bozunma sabiti	66	Metastases/Metastaz	212
Deep-learning/Derin öğrenme	138	Metastatic castrate-resistant prostate cancer/Metastatik kastrasyon dirençli prostat kanseri	57
Diagnostic challenge/Tanısal zorluk	196		
Drain-site hernia/Drenaj yeri fıtığı	115		
Emission/Emisyon	50		
Epithelial myoepithelial carcinoma/Epitelyal miyoepitelyal karsinom	125		

2024 Subject Index / 2024 Konu Dizini

MIBI scintigraphy/MIBI sintigrafisi.....	209	Quantitative analysis/Niceliksel analiz.....	94
miRNA-30C-5p/miRNA-30C-5p	19	Radiation-induced sarcoma/Radyasyona bađlı sarkom .	106
miRNA-574-5p/miRNA-574-5p	19	Radical prostatectomy/Radikal prostatektomi.....	1
MRI/MRG	156, 203	Radioactive decay formula/Radyoaktif bozunma formülü	66
Nasopharyngeal carcinoma/Nazofaringeal karsinom ...	121	Radioiodine/Radyoiyot	19
Neuroectodermal/Nöroektodermal	50	Radiomics/Radiomics	156
Neuroendocrine tumor/Nöroendokrin tümör	134	RCC/RHK	112
Non-Hodgkins lymphoma/Non-Hodgkin lenfoma	189	Relapsing polychondritis/Tekrarlayan polikondrit	109
Nuclear medicine radiopharmaceutical delivery of health care/Nükleer tıp radyofarmasötik sađlık hizmeti sunumu.....	28	Renal cancer/Böbrek kanseri.....	179
Nuclear medicine/Nükleer tıp.....	189	Renal cell carcinoma/Renal hücreli karsinom	179
Ovarian cancer/Over kanseri.....	174	Renal osteodistrophy/Renal osteodistrofi	40
Ovarian papillary serous adenocarcinoma/Over papiller seröz adenokarsinomu	212	Renal paraganglioma/Renal paraganglioma	182
Overall survival/Genel sađkalım.....	11	Response/Yanıtı	50
Paget's disease of bone/Kemiđin Paget hastalıđı	199	Saglıker syndrome/Sađlıker sendromu.....	40
Pancreatic metastasis/Pankreas metastazı.....	112	SANT/SANT	43
Pantoprazole/Pantoprazol.....	90	Secondary hyperparathyroidism/Sekonder hiperparatiroidizm.....	40
Parathyroid ectopy/Paratiroid ektopisi	209	Signet-ring cell gastric carcinoma/Taşlı yüzük hücreli mide karsinomu.....	132
Pediatrics/Pediatri	121	Somatostatin receptor imaging/Somatostatin reseptörü görüntülemesi.....	196
Peliosis hepatis/Peliosis hepatis	43	Sorafenib/Sorafenib.....	193
Perceptual metric/Algısal metrik	94	Splenic lesions/Splenik lezyonlar	43
Performance/Performans	94	Subcutaneous mass/Deri altı kitle	115
Pericarditis/Perikardit	189	Superscan/Superscan.....	38
PET/CT/PET/BT	199	Systolic volume change/Sistolik hacim deđiřimi	66
PET/CT/PET/BT ...63, 109, 112, 125, 134, 138, 174, 196, 199		Tc-99m MDP bone scan/Tc-99m MDP kemik taraması. 106	
Positron emission tomography/Pozitron emisyon tomografisi	77, 121, 193	Tc-99m-MDP/Tc-99m-MDP	212
Positron/Pozitron	50	Tc-99m-methylene diphosphonate bone scintigraphy/ Tc-99m-metilen difosfonat kemik sintigrafisi	118
Preclinical imaging/Klinik öncesi görüntüleme	90	Thyroid cancer/Tiroid kanser	19
Premedication for Meckel scan/Meckel sintigrafisinde premedikasyon	90	Thyroid cartilage/Tiroid kıkırdak	179
Primary invasive mucinous adenocarcinoma of the lung/ Akciđerin primer invaziv müsinöz adenokarsinomu.....	147	Thyroid/Tiroid	63
Primitive/Primitif	50	Tomography/Tomografi.....	50
Prognosis/Prognoz.....	167	Treatment/Tedavi	50
Prostate cancer/Prostat kanseri.....	1, 68, 112, 199	Ultrasonography/Ultrasonografi	63
Prostate carcinoma/Prostat karsinomu	38	Undifferentiated spindle cell sarcoma/Farklılaşmamıř iđ hücreli sarkom	129
Prostate-specific antigen/Prostat spesifik antijen.....	28	Uterine cervix cancer/Uterin serviks kanseri	167
Prostate-specific membrane antigen/Prostat spesifik membran antijeni	54	Volumetric parameters/Volümetrik parametreler.....	68
Prostatic adenocarcinoma/Prostat adenokarsinomu	185	Y-90 radioembolization/Y-90 radyoembolizasyonu	156
Prostatic neoplasms/Prostat neoplazmaları	28	Yolk tumor/Yolk tümörü	185
PSMA/PSMA	54, 112		